Title

Millimeter Scale Magnetic Field Manipulation in Magnetic Resonance Imaging Radio Frequency Coil and Magnetic Shielding Applications

Permalink

Author

Liu, Siyuan

Publication Date

2023

Peer reviewed|Thesis/dissertation

UNIVERSITY OF CALIFORNIA

Los Angeles

Millimeter Scale Magnetic Field Manipulation in

Magnetic Resonance Imaging Radio Frequency Coil

and Magnetic Shielding Applications

A dissertation submitted in partial satisfaction of the

requirements for the degree Doctor of Philosophy

in Electrical and Computer Engineering

by

Siyuan Liu

2023

ABSTRACT OF THE DISSERTATION

Millimeter Scale Magnetic Field Manipulation in

Magnetic Resonance Imaging Radio Frequency Coil

and Magnetic Shielding Applications

by

Siyuan Liu

Doctor of Philosophy in Electrical and Computer Engineering

University of California, Los Angeles, 2023

Professor Robert N. Candler, Chair

Magnetic devices - components that generate, manipulate, or detect magnetic fields - are used in a variety of applications ranging from medical imaging to information transfer and sensing. The persisting motivation to miniaturize electronic devices drives a need to more effectively manipulate magnetic fields in the millimeter scale. In this dissertation, two areas are presented where miniaturization technology has been applied to create new or improved capability in the area of milliscale magnetics. For the first application, a radio frequency (RF) surface coil with a dimension that is comparable to the area of interest can maximize the signal-to-noise ratio (SNR) in Magnetic Resonance Imaging (MRI) application, allowing for higher quality images than available existing tools. This work demonstrates a miniature flexible coil that can be inserted into the body for high SNR pituitary gland MR imaging. It presents the spatial

distributions of the image SNR of the 26-mm coil in both numerical simulation and agar gel phantom experiments. Compared to the commercial head coil, the miniature coil achieved up to a 19-fold SNR improvement within the region of interest, and the simulation matched the phantom experiment within an error of $1.1\% \pm 0.8\%$. Additionally, the coil performance was characterized with cadaver heads MRI scan using a 20-mm coil. A maximum of 16-fold and an average of 5-fold SNR improvement within the pituitary gland compared to the commercial head coil was obtained. The feasibility of using the miniature flexible coil for high-SNR pituitary MR imaging has been demonstrated, showing the potential for improved detection and characterization of pituitary gland microadenoma.

In the second application, a novel way to shield the magnetic field of a single chip on a multi-chip-module is presented. This approach uses individual millimeter-size magnetic shield on each chip to reduce the chip-to-chip coupling effect of the circuits or influence on signal currents from local magnetic fields. Magnetic through silicon vias (mTSVs) were developed to help achieve the desired level of magnetic shielding. The microscale multilayer shields provided high efficiency shielding around arbitrary shapes and enabled fabrication of chip-scale shielding. This work focuses on the design and fabrication of the proposed magnetic shielding.

The dissertation of Siyuan Liu is approved.

Kyunghyun Sung

Yahya Rahmat-Samii

Yuanxun Wang

Robert N. Candler, Committee Chair

University of California, Los Angeles

2023

TABLE OF CONTENTS

Miniature Flexible Coil for High-SNR MRI of the Pituitary Gland

Compact Magnetic Shielding for a Single Chip on Multi-chip-module

List of Figures

Figure 2.8: Signals induced in coils as illustrated in [94]. When the spin is rotating in the x-y plane, the coil along the y-axis shows oscillating signals while no current is induced in the coil along the z-axis.

Figure 2.9: Coil rotation illustration. B_0 is in the +z axis. a: The coil resides in the x-z plane at θ = 0°. b: The coil is rotated around the x-axis at an angle, θ, where: 0° ≤ θ ≤ 90°. c: The coil is rotated at θ = 90°.

Figure 3.1: Phantom system setup, including the igloo cavity, resolution plate, and agar phantom. a: CAD model of the igloo cavity. The coil was placed inside the cavity. b: The 3D-printed igloo cavity. The cavity was waterproofed with the Plasti Dip (Plasti Dip Int., Minneapolis, MN, USA). A U.S. quarter is shown for reference. c: The resolution plate with hole diameters 1 mm, 1.6 mm, 2 mm, 2.4 mm, 2.8 mm, and 12.7 mm. The smaller holes were used for visual demonstration and the 12.7 mm hole was used for SNR calculation. d: CAD model of the phantom set up. The cavity was fixed inside a plastic jar and then placed on two 3D-printed supporters, allowing the jar to be set to the desired coil angle. e: Assembled phantom set up. The resolution plate was taped tightly under the cavity and then the cavity was fixed in a plastic jar. f: The plastic jar was filled with agar gel, and the coil was placed inside the cavity [1].

Figure 3.2: The tune and match process and the MRI scan experiment set up. a: A portable vector network analyzer (DG8SAQ VNWA 3, SDR-Kits, United Kingdom) was used for tune and match analysis after placing the coil inside the agar phantom. b: The tune and match box was connected to the pre-amplifier, and MRI scans were performed on the phantom [1].

Figure 3.3: The blue cylinders represent the region of interest (ROI) at various distances d from the coil. B_0 is in the +z axis. a: The coil resides in the x-z plane at θ = 0°. b: The coil is rotated around the x-axis at an angle, θ, where: 0° < θ ≤ 90° [1].

Figure 3.4: Comparison of S11 with and without the load measured with the VNA and simulated using COMSOL. The coil in both loaded and unloaded cases was tuned and matched to the resonance frequency [1].

Figure 3.5: The standard-resolution PD-TSE scan (Table 3.2 line 1) signal SNR maps and normalized amplitude of the simulated effective transverse B_1 field distributions at θ = 0°, 38°, 70° and, 90°, respectively. d indicates the distance between the coil and the imaging plane. The imaging planes were selected to be parallel to the coil plane. Columns 1&3: The SNR maps at the respective coil distances d and rotation angles θ. Column 2&4: The amplitudes of the simulated effective transverse B_1 field distributions at the central hole on the resolution. Linear color scale indicates the level of the SNR and the normalized $B_{1xy\ effective}$. The simulation fields were normalized based on the maximum $B_{1xy\ effective}$ field at d = 4.5 mm [1].

Figure 3.6: Dead spots location illustrations. The dead spots are located at where the B_1 field is mostly parallel to the B_0 field.

Figure 3.7: High-resolution PD-TSE image comparisons, using the commercial head coil (left), and the pituitary miniature flexible coil at θ = 0° (middle) and θ = 60° (right). The voxel size is $0.2 \times 0.2 \times 0.7$ mm^3. Imaging planes were selected 1 cm from the coil. Images from miniature

flexible coil are at the same window level, while the image from the commercial head coil is at its own window level for better visualization [1].

line of the box represents the 1st quartile, and the top line of the box represents the 3rd quartile. The center line inside of the box indicates the median. For 0° rotation angle (green box), the 1st quartile and the median lines overlay. The whiskers (vertical lines) extend from the ends of the box to 1.5 times the interquartile range below the 1st quartile and above the 3rd quartile. The cross (×) represents the mean value.

Figure 4.3: The distributions of the measured sellar distance in the sagittal plane. For 0° rotation angle (green box), the 3rd quartile and the median lines overlay.

Figure 4.4: The illustration of the maximum lateral intercarotid distance in the coronal plane and the distribution.

Figure 4.5: An illustration of the coil position (red line). Saline-soaked Helostat was used to secure the coil above and beneath the coil. The pituitary gland is circled in the yellow line.

Figure 4.6: A comparison of the measured S11 with various loading conditions.

Figure 4.7: (a) Picture of the Helostat placed below the coil. (b) The picture of the coil inside the sphenoid cavity (waterproofed with Plasti Dip). (c) Picture of the Helostat placed above the coil.

Figure 4.8: Comparative T1-MPRAGE images of the pituitary gland of a cadaver head obtained using the 20-channel coil (left columns a & b) and mini coil (right columns c & d) in the coronal plane. The resolution is 0.9 mm × 0.9 mm × 0.9 mm (top rows a & c) and 0.4 mm × 0.4 mm × 0.4 mm (bottom rows b & d).

Figure 4.9: Comparative T1-MPRAGE images of the pituitary gland of a cadaver head obtained using the 20-channel coil (left columns a & b) and mini coil (right columns c & d) in the sagittal plane. The resolution is 0.9 mm × 0.9 mm × 0.9 mm (top rows a & c) and 0.4 mm × 0.4 mm × 0.4 mm (bottom rows b & d).

Figure 4.10: Comparative PD-TSE images of the pituitary gland of a cadaver head obtained using the (a) 20-channel coil and (b) the mini coil in the coronal plane. The resolution is 0.7 mm × 0.7 mm × 3 mm.

Figure 4.11: MATLAB post-processing on the PD-TSE image. (a) The image filter imposed by the MRI scanner was removed from the image. (b)&(c) Pixel SNR were calculated. The size of the pixel is 0.7 mm × 0.7 mm. The color legend indicates the SNR value.

Figure 5.1: A new version of the coil with a UF.L connector. The coil is built on a FPCB. (a) The front of the coil. (b) The back of the coil. (c) The coil is connected to the coaxial cable and the tune and match circuit box.

Figure 5.2: Integration of a 2-cm diameter coil with tracking coils (top). The miniature coil is on the front side, while tracker coils are on the back side, with spacing between them determined by a PDMS spacer layer. Side view of the coil (bottom). Three tracker coils are shown for demonstration.

Figure 5.3: Possible coil positioning method. The sinus could be filled with layered materials to

support the coil. An inflated balloon could be used to secure the coil.

Compact Magnetic Shielding for a Single Chip on Multi-chip-module

Figure 6.1: Cutaway illustration of proposed magnetic shielding. The shield encapsulates the entire SCE chip and is integrated into the MCM.

Figure 7.1: 2D cap shield model. a: The top shield cap consisted of 3 layers: permalloy, Cu, and permalloy. The cap was placed on the MCM substrate (500 μm). b: Simulated magnetic flux density for the cap shield model. Magnetic flux density was attracted to the magnetic material. c: The magnetic flux density along the surface of the MCM (the red line).

Figure 7.2: 2D cap shield model with bottom permalloy layer. a: The top shield cap and the bottom permalloy layer (100 μm). b: Simulated magnetic flux density for the model. The magnetic flux density along the surface of the MCM (the red line) is 27.3 μT.

Figure 7.3: The magnetic flux density at the surface of the MCM at various Si substrates for the MCM.

Figure 7.4: Addition of magnetic vias to magnetic shield. a: Location of magnetic vias at corners of shield. b: The vias connect the shield cap to the bottom permalloy layer beneath the substrate.

Figure 7.5: Comparison of the magnetic flux density at surface of the MCM inside the shield (along the red lines). a: When there is no TSV in the shield design. b: TSVs are placed at each corner of the shield.

Figure 7.6: The magnetic flux density simulated inside the permalloy material.

Figure 7.7: (a) Isosurface plot of internal magnetic fields. (b) Contour plot of the internal magnetic field below 4 μT.

Figure 7.8: In-plane and out-of-plane shielding simulations. (a) 50 μT out of plane external field is applied to the magnetic shielding. (b) The magnetic field contours at the bottom of the shield under out of plane external field. (c) 50 μT in plane external field is applied to the magnetic shielding. (d) The magnetic field contours at the bottom of the shield under in plane external field.

Figure 7.9: Shields simulation with dimensions of 10 mm × 10 mm × 3mm, 7.5mm × 7.5 mm × 2.25 mm, 5 mm × 5 mm × 1.5 mm, and 2.5 mm × 2.5 mm × 0.75 mm. 4 vias, 8 vias, and via at every 300 μm cases were simulated for each dimension.

Figure 7.10: The simulation model to evaluate effects of multiple shields in proximity on a single MCM substrate.

Figure 7.11: Results from proximity shield simulations. Note that the single shield case is where only the center chip is shielded, and the remaining three cases are when all locations denoted are

shielded simultaneously.

List of Tables

Miniature Flexible Coil for High-SNR MRI of the Pituitary Gland

Compact Magnetic Shielding for a Single Chip on Multi-chip-module

ACKNOWLEDGEMENTS

First and foremost, I am extremely grateful to my supervisor Professor Robert N. Candler for his invaluable advice, continuous support, and patience during my PhD study. His immense knowledge and plentiful experience have encouraged me in all the time of my academic research and daily life.

I would like to thank my committee members, Professor Kyunghyun Sung, Professor Yahya Rahmat-Samii, and Professor Yuanxun Wang, for their feedback and comments to guide this dissertation to completion. I would like to thank our collaborators, Dr. Marvin Bergsneider, Dr. Sophie Peeters, Dr. Giyarpuram Prashant, Dr. Rock Hadley, Dr. Michael Hamilton, Dr. Mark Adams, Jiahao Lin, and Sherman Peek for their help and support to this dissertation.

I also would like to thank all the members in the Sensors and Technology Laboratory for their kind help and advice that have made my study and life at UCLA a wonderful time. Thank you to Dr. Yuan Dai, Dr. Max Ho, Dr. Sidhant Tiwari, Dr. Jimmy Wu, Dr. Ling Li, Dr. Zhuyun Xiao, and Dr. Ben Pound.

I also appreciate all the help from the staff members and facilities of the UCLA Nanoelectronics Research Facility, the Integrated Systems Nanofabrication Cleanroom, and the Center for High Frequency Electronics.

Finally, I would like to express my gratitude to my family and friends. Special thanks to my parents Yi and Tao for their unconditional support. Without their tremendous understanding and encouragement in the past few years, it would be impossible for me to complete my study. Thank you to Zixuan Rong, for all the love and support.

VITA

EDUCATION

UNIVERSITY OF CALIFORNIA, LOS ANGELES   **Los Angeles, CA**
   Master of Science, Electrical and Computer Engineering   *9/2017-3/2019*

UNIVERSITY OF CALIFORNIA, LOS ANGELES   **Los Angeles, CA**
   Bachelor of Science, Electrical Engineering   *9/2013-3/2017*
   CUM LAUDE

PUBLICATIONS

S. Liu, L. Jiahao, M. Bergsneider, J. R. Hadley, N. G. Prashant, S. Peeters, R. Candler, K. Sung, "Experimental and Numerical Simulation of the Miniature Flexible Coil for High-SNR Pituitary MRI", Joint Annual Meeting ISMRM-ESMRMB & ISMRT 31st Annual Meeting, May 07-12, 2022, London, England, UK.

S. Liu, L. Jiahao, M. Bergsneider, J. R. Hadley, N. G. Prashant, S. Peeters, R. Candler, K. Sung, "A Miniature Flexible Coil for High-SNR MRI of the Pituitary Gland". IEEE Access, 10, 12619–12628. 2022.

J. Lin, S. Liu, R, Hadley, M. Bergsneider, G. Prashant, S. Peeters, R. Candler, K. H. Sung, " Exploration of the Surgical Placement of the Local Pituitary Coil for Microadenomas", International Society for Magnetic Resonance in Medicine, May 15-20, 2021.

S. Peeters M., S. Liu, J. Lin, R. Candler, K. H. Sung, G. Prashant, M. Bergsneider, "Signal to Noise Ratio Increases with Miniature Surface Coil Position as Demonstrated by Both Numerical Simulation and Experimental Validation", J Neurol Surg B Skull Base 2021; 82(S 02): S65-S270

Y. Dai, A. Abiri, J. Pensa, S. Liu, O. Paydar, H. Sohn, S. Sun, P. A. Pellionisz, Cassidy Pensa, E. P. Dutson, W.S. Grundfest, R. Candler, "Biaxial Sensing Suture Breakage Warning System for Robotic Surgery", Biomed Microdevices 21, 10. 2019.

Y. Dai, A. Abiri, S. Liu, O. Paydar, H.n Sohn, E. P. Dutson, W. S. Grundfest, R. N. Candler, "Grasper Integrated Tri-Axial Force Sensor System for Robotic Minimally Invasive Surgery", 39th Annual International Conference of the IEEE Engineering in Medicine and Biology Society, July 11-15, 2017, Seogwipo, South Korea

Y. Dai, O. Paydar, A. Abiri, Z. Xiao, X. Guan, S. Liu, A. Tao, E. P. Dutson, W. S. Grundfest, R. N. Candler, "Miniature Multi-axis Force Sensor for Haptic Feedback System in Robotic Surgery", 38th Annual International Conference of the IEEE Engineering in Medicine and Biology Society, August 17-20, 2016, Florida, USA

Miniature Flexible Coil for High-SNR MRI of the Pituitary Gland

Chapter 1: Introduction and Motivation

Magnetic resonance imaging (MRI) is a non-invasive tomographic imaging technique that provides images of the internal characteristics of an object from the nuclear magnetic resonance (NMR) signals [2]. First observed in 1946, NMR signals are used to form images by spatial information encoding principles. The spatial information is then uniquely encoded into the activated MR signals that can be detected outside the object. As a powerful imaging tool, MRI operates in the radio-frequency (RF) and provides a multidimensional data array for the spatial distribution of measured quantity without ionizing radiation and associated potential harmful effects [3]. This versatile imaging technique is capable of imaging any arbitrary scan plane or 3D volume and is applicable to various anatomical structures throughout the body [4]. Most importantly, MRI is flexible in data acquisition, and MR images contain very rich information, such as tissue contrast, blood flow velocities, tissue temperature, and metabolite concentration [5][6][7].

The current imaging capability of MRI has been reached through decades of innovations and developments in several areas. Image acquisition and reconstruction algorithms provide better image quality and contrast [7]. Additionally, recent advances in the MRI hardware, including increased field strength and optimized gradient performance, have effectively improved MRI performance [8][9]. Meanwhile, the development of the RF system should not be underestimated. RF coils are the main components of the MRI hardware, responsible for transmitting and receiving the MR signals. Their advances have significant impact in improving the image resolution and shortening the examination times in today's MRI techniques.

RF coils can be distinguished into two categories: volume coils and surface coils. In volume coils, the sample is inserted into the coil volume, and the coils surround the anatomy of

interest. Volume coils are widely used in applications that require better RF homogeneity as the coils extend over a large area. An RF surface coil has a dimension comparable to the area of interest and can maximize the signal-to-noise ratio (SNR) close to the surface of the patient [8]. For example, multi-channel surface coil arrays are developed for brain imaging [8][9][10][11]. However, surface coil arrays are unsuitable for imaging structures in the center of the body or head. In the center of the head, the corresponding noise increase will undermine the signal and downgrade the overall performance [14]. This makes MRI imaging of the pituitary gland and the sella at the center of the cranium using conventional surface coils unsuitable.

The main objective of this work is the development of a miniature flexible coil for high-SNR MRI of the pituitary gland. With the local pituitary coil, we intend to increase the SNR to provide sufficient spatial resolution for pituitary microadenoma detection and characterization.

1.1. Basics of MRI

1.1.1. Signal generation and detection

MRI is based on the NMR phenomenon that was first observed in bulk matter. It is known that any material can be broken down into nuclei and orbiting electrons. The nuclei with odd atomic numbers possess a net angular momentum called spin, which can be visualized as a physical rotation about its axis, although the protons and neutrons are not physically spinning. The most common NMR-active nucleus used in MRI scanning is hydrogen-1 due to its abundance in the body [15]. It is also the most sensitive and by far the most studied nuclei in biomedical MRI [4]. Other nuclei, such as carbon-13, fluorine-19, and phosphorus-31, are used for imaging as well [16]–[18].

Spin is the physical basis of MRI, and a spin system is activated by external magnetic

3

fields and RF excitations to produce the signals. Normally, the hydrogen spins are orientated randomly in the body with no net magnetization. When the body is placed in an external magnetic field (B_0), such as an MRI scanner, the spins will align their orientations to the external magnetic field. This uniform alignment creates a net magnetization along the direction of the external field. To detect the magnetization, we need to add additional energy from a transverse RF magnetic pulse (B_1) to the B_0 magnetic field. The spins are activated from the RF pulse, and their orientations are flipped away from the external field axis. As the magnetization direction is deflected, the spins start to precess at a frequency called the resonance frequency or Larmor frequency (f_{Larmor}). Larmor frequency is proportional to the external magnetic field as shown in equation (1.1). For hydrogen-1, the gyromagnetic ratio (γ) is 42.58 MHz/Tesla [2].

$$f_{Larmor} = \frac{\gamma}{2\pi} B_0 \qquad (1.1)$$

After the RF excitation is switched off the spins return to the resting state, emitting an RF wave as the signal. This signal is captured by the receiving coils and induces a current in the loop according to Faraday's law of induction [5]. The intensity of the received signal is then plotted in a grey scale and decoded into the cross sectional images [15].
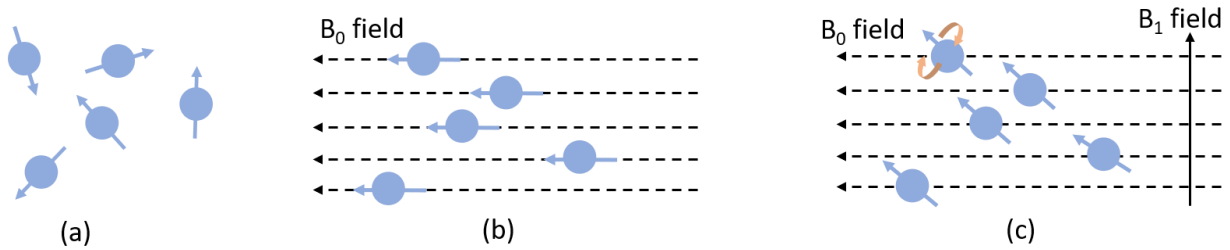
Figure 1.1: The spin system in MRI. (a) spins are orientated randomly, (b) spins align their orientations to B_0 field, (c) spins orientations are flipped away after B_1 field is applied and start to precess.

1.1.2. MRI hardware

The key components of a MR scanner are the main magnet, the magnetic field gradient system, and the RF system.

The main magnet

The main magnet can be a resistive, a permanent, or a superconducting magnet [2]. The main magnet is used to generate a strong and uniform static magnetic field (B_0) pointing in the longitudinal direction. The strength of this static field determines the magnetization of the nuclear spins and the Larmor frequency. In the early days of MRI, the magnetic field strengths ranged from 0.1 T to 0.3 T, achieved with resistive magnets (< 0.15 T) or permanent magnets (0.3 T). For current clinical systems, higher field strength frequently operating at 3T and more recently at 7 T is now used thanks to improvements in superconducting magnet technology [19].
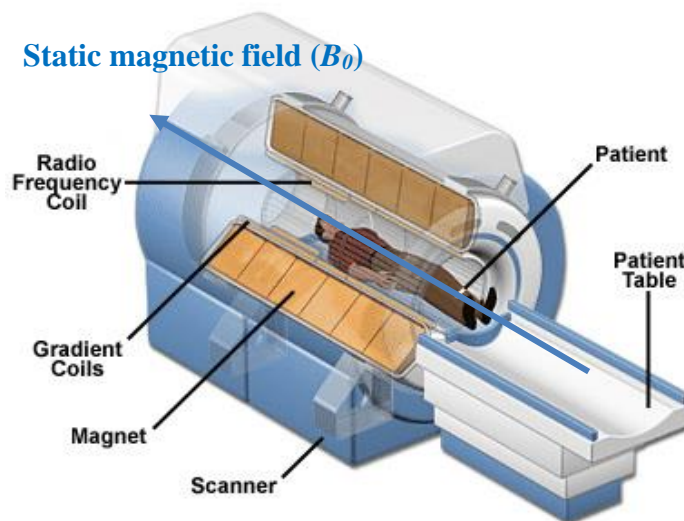
Figure 1.2: *MRI Scanner Cutaway. Static magnetic field (B_0) is pointing in the longitudinal direction as illustrated in* [20].

The required field strength depends on the specific application. While a higher field provides better SNR and spectral resolution, it also causes problems such as RF penetration,

higher cost, and uncertain clinical benefits [2][21]. The spatial homogeneity of the static magnetic field is an important feature. The homogeneity of the magnetic field is given as the maximum deviation of the field over the volume [2]:

$$\text{Homogeneity} = \frac{B_{0,max} - B_{0,min}}{B_{0,mean}} \qquad (1.2)$$

The gradient system

A magnetic field gradient is used to produce field variations in the main magnetic field. A linear magnetic field gradient is the most common method to determine the spatial distribution information. The system typically consists of three orthogonal gradient coils, producing a linearly varying gradient, G_x, G_y, G_z as shown in Figure 1.3. Therefore, the Larmor frequency of spins varies as a function of position in the *x, y*, and *z*-axes [22]. For example, the Larmor frequency of a spin at a specific point *x* when G_x is applied is given by equation 1.3. This variation can be used for spatial encoding with Fourier transform [23].

$$f_{Larmor} = \frac{\gamma}{2\pi}(B_0 + G_x x) \qquad (1.3)$$
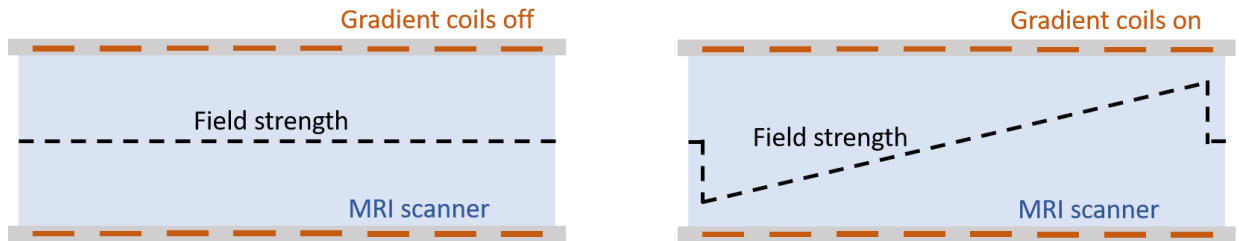
Figure 1.3: Field strength inside the MRI scanner: (a) when the gradient coils are off, the field strength is uniform, (b) when the gradient coils are on, the field strength shows a gradient.

The RF system

The RF system of the MR scanner is responsible for spin excitation and signal detection in MRI [2]. It includes a transmitter coil that generates the B_1^+ field for spin system excitation

and a receiver coil that transforms the precessing magnetization B_1^- field into the electrical signal. Both transmitter and receiver coils can be treated as resonant circuits with capacitors and inductors to store the electric and magnetic energy. The circuits need to be tuned and matched to reach the best performance. Tuning the coil circuit refers to adjusting the coil resonance frequency to Larmor frequency of the spins in the object. In this way, the coil will produce a large precessing magnetization from the excitation. On the other hand, matching the circuit impedance ensures that the power transfer from the amplifier to the coil is maximized and the greatest possible power is transmitted to the spin system [8]. Therefore, a better tuned and matched coil can provide higher SNR.
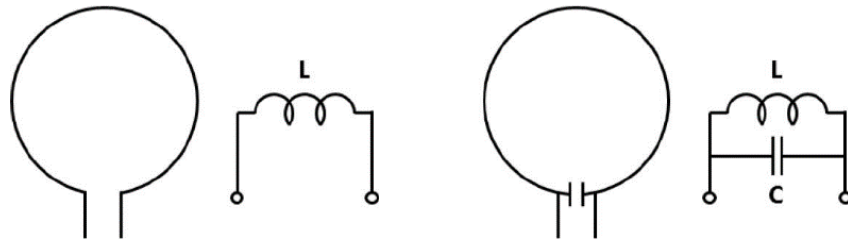
Figure 1.4: Equivalent circuit models for circular loop coils as illustrated in [24].

1.2. Coils in MRI

Various types of RF coils have been used in different fields of applications. Based on their usage, RF coils can be divided into volume coils and surface (array) coils. In volume coils, the sample is inserted into the coil volume, and the coil surrounds the anatomy of interest. Volume coils are widely used in applications that require a better RF homogeneity as they extend over a large area. An RF surface coil is made up of loops of wire that match the dimension of the area of interest. Due to its smaller size and proximity to the investigated structure, the signal received from the sample has a higher amplitude than that from a large volume coil, and less

noise is therefore coupled to the coil. Using small surface coils helps improve SNR in restricted regions [8].

Single loop coil

The single loop coil design is the simplest form of receiving surface coil. It can be designed with a very small diameter for insertion into small areas of interest and makes the "in vivo" experiment possible. However, there is a limit on the smallest size of the coil. The total resistance of the coil depends on both the coil itself and the sample since the coil couples to the sample. As coil radius decreases, coil resistance increases relative to sample resistance. A small coil is dominated by sample resistance and therefore sample noise. When the coil noise ultimately dominates the SNR, the sensitivity of an RF coil cannot be increased through coil miniaturization [25]. Therefore, coils are typically operated in a sample noise dominated regime [26].

Butterfly coil/ Figure-of-eight coil

For a single loop coil, the RF field is strong near the coil wire and the center has less coverage [27]. A coil with a butterfly or figure-8 geometry can be used to reduce signal intensity inhomogeneities of the center [28], [29]. The optimum geometry for the butterfly and figure-8 coils that deliver the best SNR will be examined. The butterfly coil will be oriented in a different way as the single loop coil since they have different associated magnetic flux vectors [30].

Combined coil

The butterfly coil has a magnetic flux vector that is transverse to the magnetic flux vector

of the loop coil. When combining a single loop coil and a butterfly coil, we can get a quadrature surface coil, which detects the MR signal in orthogonal directions [8]. If signals from the two coils are fed into a 90-degree combiner and added together in an analog way, a single-channel output is produced. The combined signals from the quadrature coils offer better SNR compared to single loop coils and a perfect quadrature coil can improve the SNR at the center of the coil by $\sqrt{2}$-fold gain over a single loop coil [30].

(a) (b) (c)
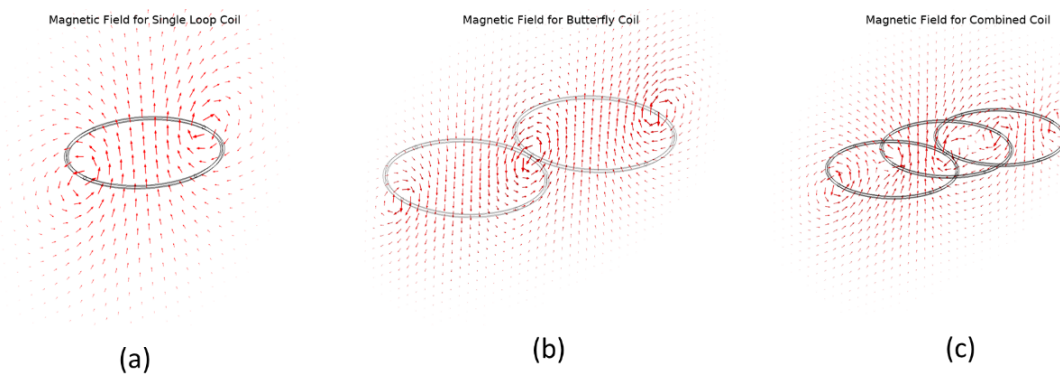
Figure 1.5: The magnetic field distribution for (a) single loop coil, (b) butterfly coil, and (c) combined coil.

1.3. MRI scan parameters

An MRI sequence consists of multiple RF pulses and gradients and results in images with a particular appearance [31]. The programmed set of changing magnetic gradients has various parameters, and the sequences are grouped into an MRI protocol [32]. Here are some of the parameters that define the pulse sequence:

- Time to echo (TE): the time between the RF excitation pulse and the peak of the signal induced in the coil. TE controls the amount of T2 relaxation, which is the progressive decay or dephasing of the transverse components of magnetization [33].

- Repetition time (TR): the time between the application of the excitation pulse and the next. TR determines the recovery of the longitudinal magnetization between each pulse [34].

- Flip angle: the amount of rotation the net magnetization experiences during a RF pulse [35].

- Field of view (FOV): the dimensions of the anatomic region to be imaged, specified in millimeters or centimeters.

- Matrix size: the number of frequency encoding steps and the number of phase encoding steps [36]. In other words, it is the number of pixels in the images.

- Bandwidth: the range of frequencies associated with RF excitation or signal reception [37].

- Number of excitations (NEX) or number of signal averages (NSA): the number of times each line of k space is sampled [38]. It describes the number of times a signal from a given slice is measured.

MRI spatial resolution determines the ability of human eyes to distinguish structures as separate and distinct from each other [39]. In MRI, the in-plane resolution is determined by the number of pixels in the FOV. A pixel represents the smallest 2D element in the image, and its size can be calculated by dividing the FOV by the matrix size [40]. Spatial resolution is also related to the acquired voxel volume. A voxel is the volume element in the 3D space. The dimensions of the voxel are given by the pixel and the thickness of the slice. Resolution is inversely proportional to the pixel size: the smaller the pixel size, the higher the resolution. Low-resolution images may look "blurry", and high-resolution images in general have better image quality. However, decreasing the pixel size also decreases the signal received by individual pixel. Therefore, small voxels provide MR images with high spatial resolution but a lower SNR, and the image may appear "grainy" [39].

Another consideration is the image acquisition time or scan time, which increases in

direct proportion to the matrix size [41]. To achieve a high-quality diagnostic image with a smaller pixel size, we also get a longer scan time. The scan time can be calculated as [42]:

$$Scan\ time = TR \times number\ of\ phase\text{-}encoding\ steps \times NEX \quad (1.4)$$

The effects of the sequence parameters on the SNR, spatial resolution, and scan time can be summarized in the following tables:

Table 1.1: *Effects of imaging and sequence parameters on SNR are seen in [11, Table 4].*

Change in parameter	Effect on SNR
TR ↑	↑
TE ↑	↓
Slice thickness ↑	↑
FOV ↑	↑
Matrix size ↑	↓
NEX ↑	↑
Magnetic field strength (B_0) ↑	↑
Receiver bandwidth ↑	↓

Table 1.2: *Effects of parameters on spatial resolution are seen in [11, Table 5].*

Change in parameter	Spatial resolution
Slice thickness ↑	↓
FOV ↑	↓
Matrix size ↑	↑

Table 1.3: *Effects of parameters on scan time are seen in [11, Table 6].*

Change in parameter	Scan time
TR ↑	↑
TE ↑	↑
Slice thickness ↑	↓
Matrix size ↑	↑
NEX ↑	↑

1.4. Motivation

There is a strong clinal need to achieve a better resolution the MRI for detection of small pathological lesions. One example is Cushing's syndrome, which is characterized by the hypersecretion of the adrenocorticotropic hormone (ACTH) due to a pituitary adenoma, whose features include abnormal fat distribution, proximal muscle weakness and hypertension [43][44]. If left untreated, Cushing's syndrome may lead to a significant morbidity and mortality [45]. However, the diagnosis of Cushing's disease (CD) remains a challenge and is often delayed due to the small size of the pituitary tumors and the poor SNR in MR imaging [46]. Current clinical imaging method, 3T MRI [47]–[50], fails to detect over 50% of microadenomas in Cushing's disease and nearly 80% of cases of dural microinvasion[51],[46]. This failure of diagnostic imaging hinders the primary and optimal treatment of CD: surgical excision of the offending tumor. In such cases without an imaging-identifiable tumor, neurosurgeons must consider surgically "exploring" the anterior pituitary gland by making multiple parallel incisions typically spaced 2-3 mm apart with the hope of encountering the tumor. This procedure has a significant failure rate of finding a tumor and introduces the risk of permanently damaging the normal pituitary gland.

The median size of the pituitary tumors causing CD is 5 mm and a large portion of tumors are less than 3 mm [32][33]. Standard 3T pituitary MRI protocols generate multi-slice 2-dimensional (2D) images with a typical in-plane resolution of 0.7×0.7 mm^2 and a through-plane slice thickness of 3 mm [51]. When considering various shapes of the pituitary gland, partial volume averaging, and motion-related degradation [54], it is not surprising that MR images with an in-plane pixel size of 0.7 mm commonly fail to detect lesions smaller than 3 mm.
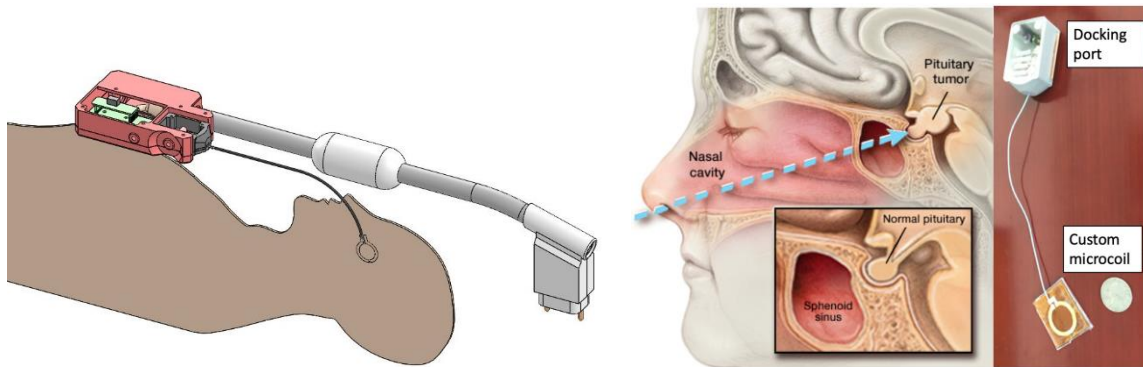
Figure 1.6: *Project concept with a prototype custom miniature coil that can be inserted to enable increased SNR in a transsphenoidal endoscopic surgery as illustrated in* [55]. *A US quarter is shown for the size comparison.*

To improve image resolution, we have focused on improving the SNR. The higher SNR can be used to improve spatial resolution with thinner imaging slices and higher in-plane resolution [56]. There are both physiologic and physical reasons that limit the SNR. For the physiologic reason, the detection of pituitary adenomas using MRI typically relies on a contrast of signal intensity between the tumor and the normal gland. The intravenous gadolinium contrast infusion shortens the spin-lattice relaxation time (T1) of voxels and thus the tumor appears relatively brighter on T1-weighted imaging [57]. However, the timing and intensity of the maximum contrast difference varies from patient-to-patient. Standard pituitary imaging, which takes image at arbitrary time points after contrast injection, may fail to detect tumors if the

maximum differential point is missed. On the other hand, dynamic imaging, in which the images are taken in a repeated fashion, decreases imaging acquisition times and therefore SNR is also decreased, further reducing the possibility of detecting a small tumor.

The physical reasons for reduced SNR include motion artifacts, low MRI field, and receiving coil distance:

1) Patient motion during the MRI scanning, such as periodic cardiac and respiratory motion, involuntary movements like yawning, swallowing, and blinking, or conscious motion due to discomfort, can cause motion artifacts and reduce image quality because of blurring or geometric distortion. A shorter acquisition time can mitigate these artifacts, but it also reduces SNR [58].

2) Low field can also limit the SNR. In theory, SNR increases linearly with field strength (B_0) [59], [60]. Higher field strength scanners, however, may lead to other problems from increased susceptibility to motion and other artifacts [47], [61], [62].

3) The distance of receiving coil from the target tissue also limits the SNR. Current pituitary MRI is usually performed with coils that are placed outside of the head, for example, the birdcage head coil [47], [48],[63],[64]. Three-dimensionally, signal strength from the source decreases as the cube of the distance [65].

Our approach to improve SNR utilizes a custom receiver coil designed to be placed in close proximity to the pituitary gland. RF surface coils usually have dimensions that are comparable to the area of interest and can maximize the SNR close to the surface of the patient [8]. For example, the prostate imaging using endorectal coils demonstrates SNR improvements of 5 to 9 times compared to phased-array coil [66] but is has seen limited clinical adoption due to discomfort during the coil placement [67]. Chittiboina, et al modified the prostate-endorectal surface coil and placed it within the sphenoid sinus for pituitary imaging [46]. A sublabial

approach to the sphenoid sinus was necessary to position this cylindrical coil close to the sella turcica. They demonstrated a ten-fold increase in SNR within the pituitary gland in cadaveric studies [46]. However, this semi-rigid, bulky prostate coil has major limitations for pituitary imaging, including the inability to use a transnasal approach due to the large coil size, potential safety concerns related to the semi-blind positioning, risk of sterility violations due to the need to "double-bag" the probe in plastic, and suboptimal angulation of the coil relative to the B_0 field.

In this work, novel customized in-body miniature flexible pituitary coils are proposed, which will be surgically positioned millimeters from the pituitary gland. The miniature flexible coil could easily be placed via one nostril and optimally situated inside the sphenoid sinus under direct endoscopic visualization [1]. Since the coil placement is a part of a surgical operation for the tumor removal, the surgical placement does not add additional surgical operation to the patients. Using a remote tune and match technique, only the coil loop and cable need be inserted endonasally. As no electrical component is placed on the coil trace, the coil can be easily folded and safely positioned inside the human body.

The coils are numerically optimized to fit inside the limited physical space of the sphenoid sinus, and the simulation models were validated through the agar gel phantom MRI experiment. The ideal orientation of the coil is parallel to the orientation of the main magnetic field, B_0. As the surgical positioning for endoscopic surgery is supine, our investigations of the sphenoid sinus anatomy indicate that this coil orientation may not be anatomically possible in some cases. Therefore, we studied the angular misalignment effect between the coils and the static magnetic field (B_0 field) with the agar gel phantom. We investigated the spatial distributions of the image SNR for various coil rotation angles (θ) using a numerical simulation model and phantom experiments. Compared to a 20-channel commercial head coil, our miniature

coil achieved up to a 19-fold SNR improvement within the region of interest. The simulation and phantom experiment reached a good agreement, with an error of 1.1% ± 0.8%. Additionally, to ensure coil safety for the clinical environment, we performed temperature measurements on the meat phantom and examined the temperature rise at various measuring sites. No detectable temperature increase was found for a continuous 15-minute scan measured by a benchtop fiber optic thermometer (FOTEMP1-4, Optocon®, resolution = 0.1°C). Finally, the coil performance was characterized by cadaver heads MRI scan. The waterproof of the coil and the tune and match condition were tested. A maximum of 16-fold SNR improvement and an average of 5-fold SNR improvement within the pituitary gland was obtained using the miniature coil compared to the commercial head coil. The feasibility of using the miniature flexible coil for high-SNR pituitary MR imaging in a pre-clinical environment has been demonstrated, leading to the improved detection and characterization of pituitary gland microadenoma.

Chapter 2: Finite Element Analysis of the miniature flexible coil

2.1. Introduction

We designed a single loop miniature flexible coil that could easily be placed via one nostril and situated within the sphenoid sinus at the optimal angle under direct endoscopic visualization. The coil design is used as part of a surgical operation with the aim of removal of the tumor. The ideal orientation of the coil is parallel to the orientation of the main magnetic field, B_0, with the coil axis perpendicular to the B_0 field. However, since the surgical positioning for endoscopic surgery is supine, our investigations of sphenoid sinus anatomy indicated that this parallel coil orientation may not be anatomically possible in some cases. An agar gel with the 3D printed igloo cavity and a resolution plate are designed to allow us to study the effect of coil angulation relative to the B_0 field. Real-time remote tuning and matching is performed after the coil placement.

2.2. Coil and Interface Design

2.2.1. Initial design

The prototype customized local coil was constructed for a 3T MRI scanner (Prisma, Siemens Healthcare) with a Larmor frequency = 123.2 MHz. We started our design from a single loop of coil with no electrical components (capacitors and inductors) on the trace. The coil radius was chosen based on the size of sella bone and the image depth. For a circular loop coil, optimal coil diameter is proportional to the imaging depth of interest: $R_{optimal}=d_{max}/\sqrt{5}$, where d_{max} is the maximum distance of interest from the coil [68]. The diameter of the coil should be large enough to cover the pituitary gland in the region of high sensitivity. In the meanwhile, the coil needs to fit the physical constraint of the sphenoid sinus and a larger radius may introduce excessive noise

17

from volume outside the region of interest [69][70]. On the other hand, a smaller radius results in lack of signal in the region of interest and the coil noise dominates in the system [26]. In 20 consecutive endoscopic pituitary surgeries, we used various sizes of sterile cotton patties ("cottonoids") to subjectively assess the suitable size of the coil [1]. The experience revealed that a coil diameter up to 2.5-cm could easily be inserted without hyperangulation (kinking). Once past the nostril, further advancement into the sphenoid sinus was easy and safe.

The coil with an interior diameter of 20 mm connected to two stubs of 10 mm in length was simulated in Agilent Advanced Design System (ADS). The width of the copper trace was 3 mm (Figure 2.1). With no electrical tuning elements, the coil had very limited flexibility in the tuning capability. We simulated the coil on a 25 μm polyimide substrate and plotted the scattering parameter S11, which represented how much power was reflected from the coil. The simulated S11 showed a resonance around 1 GHz, which was far away from the desired resonance frequency at 123.2 MHz. The S11 at the resonance frequency was only -6.510 dB with $10^{-6.510/10} \approx 22.5\%$ of the power being reflected.
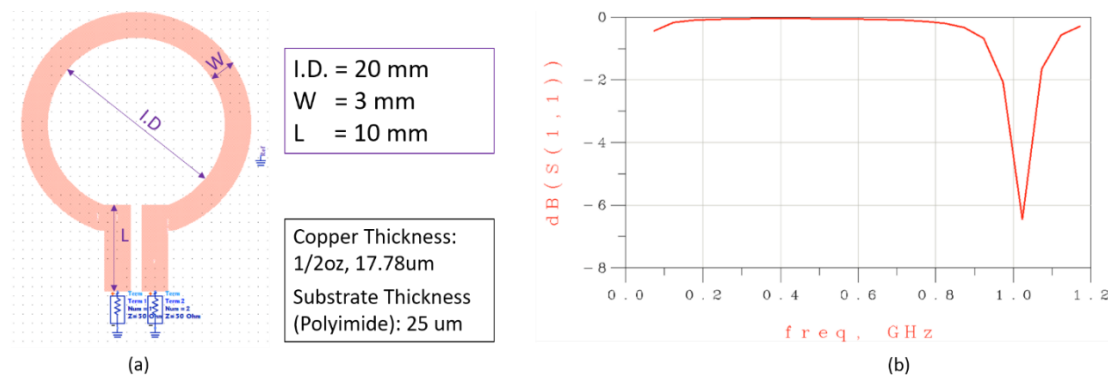
Figure 2.1: *Single loop coil with no electrical components design: (a) the coil dimension, (b) S11 plot of the coil.*
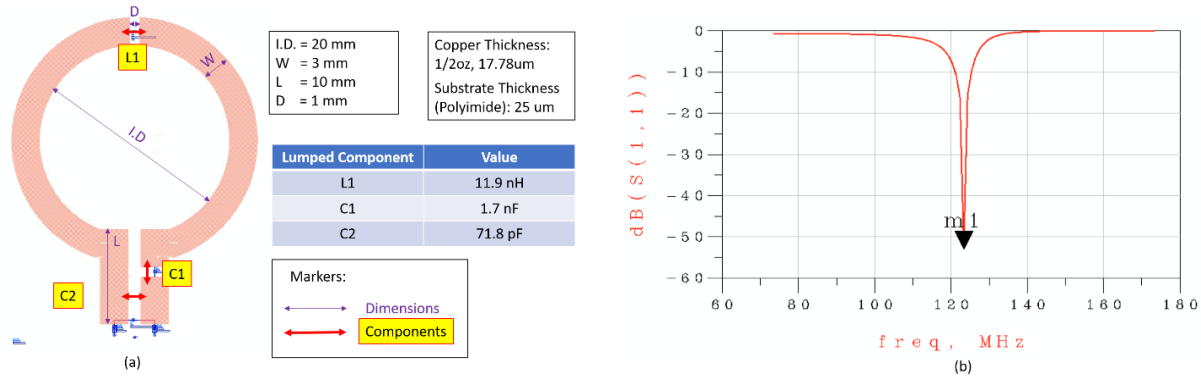
Figure 2.2: *Single loop coil with 2 gaps: (a) the coil dimension and lumped components values, (b) S11 plot of the coil.*
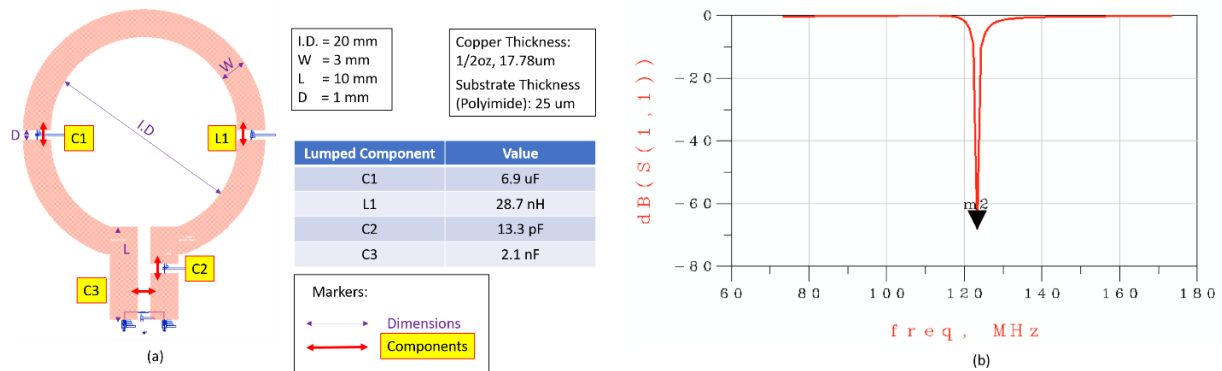
Figure 2.3: *Single loop coil with 3 gaps: (a) the coil dimension and lumped components values, (b) S11 plot of the coil.*

A traditional method used in tuning the circular loop coil is to place lumped capacitors and inductors on the loop to adjust the resonance frequency[69][5][6]. For the second design, we had a coil with 2 gaps. On the top of the coil loop, an inductor of 11.9 nH was placed, and two capacitors were added, one 1.7 nF capacitor on the stub and one 71.8 pF capacitor between the two stubs (Figure 2.2). For this design, the simulated S11 at the resonance frequency 123.2 MHz is -52.987 dB, showing a much better tuning condition for the coil. We also tried tuning the coil with even more lumped elements added (Figure 2.3), and a simulated S11 of -68.218 dB was reached.

The single loop coil designs with lumped elements demonstrated reasonably good

resonance at the desired frequency. However, the lumped elements would make the coil less flexible. Since the coil is intended to be placed in proximity to the pituitary gland that requires coil deformation during operation, flexibility of the coil is a major concern in the coil design. Furthermore, a good coil design should be able to fit various patients and maintain its performance when positioned near samples with different conductivities. Therefore, a real-time tuning and matching process –with the components located off the coil - is needed instead of using lumped elements with limited tuning capability.

2.2.2. Current design

The current single-loop coil design consists of a local coil with a 20 mm diameter loop made from a single contiguous copper trace (3 mm in width and 17.8um in thickness) on a plated flexible printed circuit board (PCB). The coil is attached to a coaxial cable (Siemens Healthineers, Forchheim, Germany: 50 Ohms, 1.13 mm diameter, 0.22 mm inner conductor diameter, 20 cm length). All lumped electrical components are placed in a 3D-printed box along the length of the cable [73]. The coil assembly is tuned to a resonance frequency of 123.2MHz (for 3 Tesla imaging), and impedance matched by adjusting the electrical components in the circuit box. Active decoupling is also included in the circuit, without lumped element capacitors, during the transmit phase of the pulse sequence. The active detuning is done by putting an inductor in parallel with the net capacitance of the coax cable and detuning the inductive coil loop at the Tx mode. A built-in docking port transmits the Rx signal from the coil remote tuning/matching box to the preamp via an MCX connector.
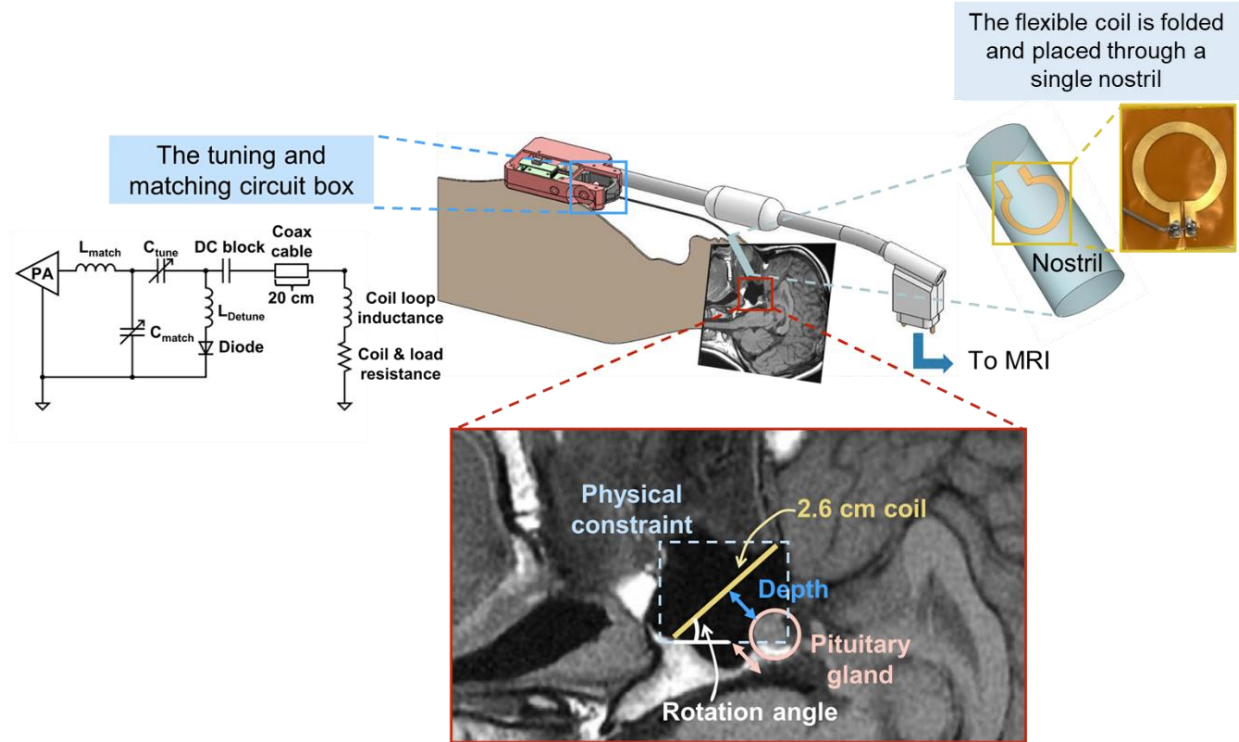
Figure 2.4: *Coil design and the surgical placement. The coil is built on a flexible and connected to the preamp box. The tune and match box allows fine-tuning the coil remotely. Local pituitary coil is placed against the pituitary gland, and the coil rotation angle is defined as the angle between the coil plane and the scanner bed* [1].

The coil is designed to tune and match remotely so that only the coil loop and cable need to be inserted endonasally. The adjustable electronics components are housed in a 3D-printed circuit box and are kept outside of the body. With a 20 cm length, the cable is short enough to not pick up any significant currents from the body coil during Tx. If the coax cable needs to be longer than 20 cm, common mode current chokes could be used on the cable to impede the shield currents. A balun will also be needed on the pre-amplifier circuit board for this technique.

2.3. Electromagnetic simulation

The modeling of RF coils in MRI is an important step in coil design and development as it sheds light on the interaction between RF energy and imaging targets. To study the

electromagnetic behavior of the coil, we developed a 3D coil simulation of Finite Element

Method (FEM) models in COMSOL 5.2 Multiphysics® [74].

2.3.1. Finite Element Method (FEM)

The laws of physics for space- and time-dependent problems are usually stated in terms

of partial differential equations (PDEs), which cannot be solved with analytical methods in

complicated geometries [75]. Instead, an approximation of the equations may be used based on

discretizations. It approximates the PDEs with numerical model equations by changing the PDEs

into equivalent ordinary differential equations and then solves the equations using numerical

methods. The solution to the numerical model equations can be used as an approximation of the

real solution to the PDEs. These approximations are computed by the finite element method

(FEM) by evaluating a differential equation curve with polynomial curves. The polynomials are

represented by the points on the curves, and FEM calculates the solution at the points only.

2.3.2. Maxwell's equations

In COMSOL Multiphysics, the problem of electromagnetic analysis is the problem of

solving Maxwell's equations under certain boundary conditions [76]. Maxwell's equations

provide the relationships between the fundamental electromagnetic quantities: the electric field

intensity $\mathbf{E}$, the electric flux density $\mathbf{D}$, the magnetic field intensity $\mathbf{H}$, the magnetic flux density

$\mathbf{B}$, the current density $\mathbf{J}$, and the electric charge density ρ (Equation 2.1 a-d).

$$\nabla \times \mathbf{H} = \mathbf{J} + \frac{\partial \mathbf{D}}{\partial t} \qquad (2.1a)$$

$$\nabla \times \mathbf{E} = -\frac{\partial \mathbf{B}}{\partial t} \qquad (2.1b)$$

$$\nabla \cdot \mathbf{D} = \rho \qquad (2.1c)$$

$$\nabla \cdot \mathbf{B} = 0 \qquad \text{(2.1d)}$$

2.3.3. Coil geometry and material setup

A circular loop coil is set up in COMSOL Multiphysics 3D simulation in the frequency domain based on the coil design mentioned in previous sections. The interior radius of the coil is 10 mm and the width of trace is 3 mm. The length of the bottom stubs is 10 mm, and two stubs are connected with a small block, where a copper segment is used in the actual coil. To tune and match the coil to resonance frequency and intended impedance, we place lumped elements (capacitors and inductors) on the coil trace. By sweeping the values of the lumped elements using parametric sweep in the frequency domain study, we found the capacitance and inductance that tuned the resonance frequency to 123.2 MHz with matched impedance. The coil surface is assigned to a perfect electric conductor (PEC). A uniform lumped port feeds a voltage excitation to the coil at the terminal of the coil. Scattering boundary conditions are assigned for the sphere's boundaries to prevent any reflections into the model from the outermost boundaries.

Phantoms are the non-biological material for RF coil performance characterization and validation. In recent years, agar gel has been widely used as the tissue-mimicking material for MRI brain phantoms since it is inexpensive and easy to work with [77]–[79]. In the simulation, the coil is placed inside a cylindrical agar gel phantom with a radius of 6 cm and a height of 13 cm, which is similar in size to a human head. The relative permittivity and electrical conductivity are set up according to the agar gel properties at 128 MHz [80], and the relative permeability is set to $\mu_r = 1$. An igloo cavity holds the coil and is filled with air, mimicking the sinus cavity (Figure 2.6).
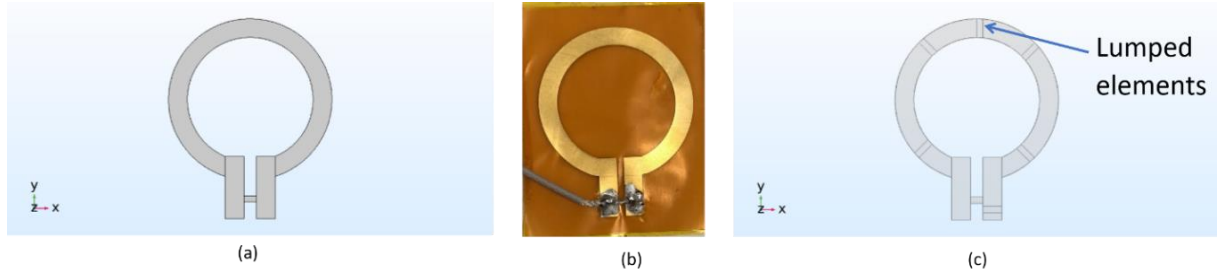
Figure 2.5: *Coil simulation model in COMSOL: (a) the coil model without lumped elements, (b) the actual coil connected to the cable, (c) the coil model with lumped elements (capacitors and inductors).*
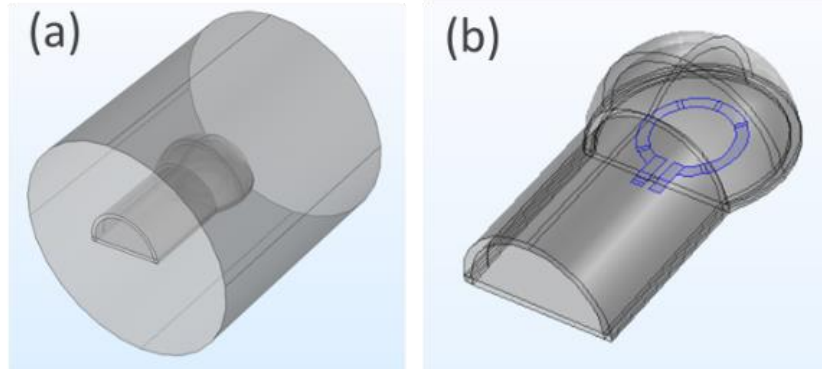
Figure 2.6: *Phantom CAD models in COMSOL Multiphysics® simulation. (a) agar phantom and igloo cavity model. (b) igloo cavity model. The coil is placed inside the cavity (highlighted).*

The quality factor Q is a dimensionless value measuring the coil efficiency to detect the MR signal and is defined as the ratio of the stored magnetic field energy and dissipated energy per oscillation [8][81]. A more practical way to calculate Q-factor is the ratio of the resonance frequency (f_0) to the 3dB bandwidth (Δf) [82]–[84]. In our coil model, the loaded Q-factor (with the phantom placed under the coil) is given as:

$$Q^{sim}_{unloaded} = \frac{f_0}{\Delta f} = \frac{123.2\ MHz}{126\ MHz - 120\ MHz} = 20.533 \quad (2.2)$$

And the Q-factor for an unloaded case (without sample/ phantom) is

$$Q^{sim}_{unloaded} = \frac{f_0}{\Delta f} = \frac{123.2\ MHz}{123.4\ MHz - 123\ MHz} = 308 \quad (2.3)$$

A common measure for sensitivity to loading is the ratio between the unloaded Q-factor and loaded Q-factor [85], [86]. In our case:

$$Q_{ratio}^{sim} = \frac{Q_{unloaded}}{Q_{loaded}} = \frac{R_{Coil} + R_{sample}}{R_{Coil}} = \frac{308}{20.533} = 15 \quad (2.4)$$

where R_{coil} represents the coil losses and R_{sample} represents the sample losses. When Q-ratio is much larger than 2, the sample noise is dominant, which is an important requirement for a good coil design [8]. Larger R_{sample} indicates the signal is more tightly coupled to the sample, leading to a higher sensitivity of the signal detection.
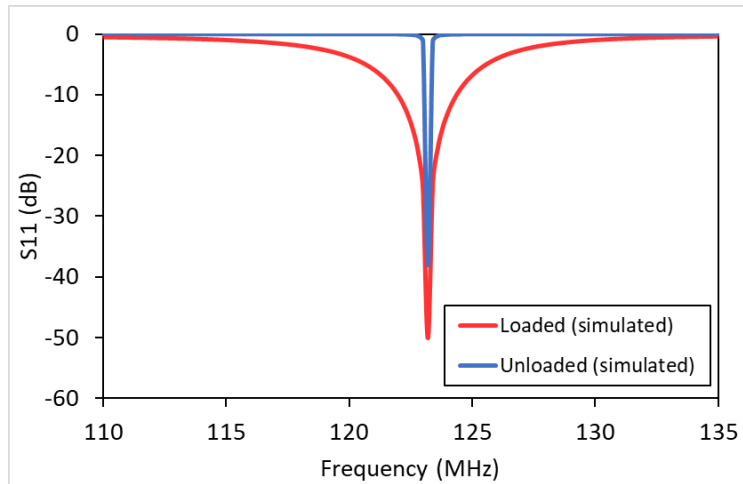
Figure 2.7: *Simulated S11 plot. Loaded S11 is simulated with the phantom placed under the coil. Unloaded S11 is simulated with no phantom presented. Both simulated S11 values are below -20 dB, which means less than 1% of power is reflected.*

2.3.4. Coil simulation SNR

The primary focus of RF receiver coil design is to improve the SNR. To assess the performance of the coil, we need to carefully evaluate the coil SNR. There are different theories on SNR calculations in RF coils [14], [87], [88]. A widely used relation for the coil SNR states that

$$\text{SNR} \propto \frac{B_1}{\sqrt{R_{coil} + R_{sample}}} \quad (2.5)$$

25

where B_1 is the magnetic field of the RF coil, R_{coil} represents the coil losses and R_{sample}

represents the sample losses [18][21][89].

If the static magnetic field B_0 is in the z-axis, the z component of the RF magnetic field

B_{1z} does not contribute to the spin excitation. The magnetic field we are interested in is the

transverse B_1 field, whose norm is given by [90]:

$$\|B_{1xy}\| = \sqrt{B_{1x}B_{1x}{}^* + B_{1y}B_{1y}{}^*} \qquad (2.6)$$

The transmit field generated by the RF coil responsible for exciting the spins is defined as:

$$B_1{}^+ = \frac{B_{1x}+iB_{1y}}{\sqrt{2}} \qquad (2.7)$$

While the receiving field is in the opposite rotation of the $B_1{}^+$ field, with an equation given as:

$$B_1{}^- = \frac{B_{1x}-iB_{1y}}{\sqrt{2}} \qquad (2.8)$$

From the Q_{ratio} calculated above, we showed that the sample noise or sample loss

R_{sample} dominates in the total noise, and the SNR can be simplified as:

$$\text{SNR} \propto \frac{B_1}{\sqrt{R_{sample}}} \qquad (2.10)$$

Sample noise is mainly from the thermal noise in the sample [91], which can be derived from the

power dissipation in the sample [92]. The summarized derivation was seen in [93, Eq. (1)-(14)].

The derivation starts by assuming a unit of alternating current to be flowing in a circular coil at

the resonance frequency. The magnetic vector potential in the coil is given as:

$$\boldsymbol{A}(\boldsymbol{R}) = \frac{\mu_0 I}{4\pi} \oint \frac{d\boldsymbol{l}(\boldsymbol{R'})}{|\boldsymbol{R}-\boldsymbol{R'}|} \qquad (2.11)$$

where μ_0 is the permeability of the free space, $I = I_0{}^{-i\omega_0 t}$ is the current flowing in the

differential length $d\boldsymbol{l}$ at position $\boldsymbol{R'}$. The time-averaged power dissipated in the resistive load R

can be expressed by:

$$W = \frac{1}{2}RI * I = \frac{1}{2}RI_0{}^2 \qquad (2.12)$$

In spherical coordinates, the differential length in the *xy* plane is given as:

$$d\boldsymbol{l} = a(-\mathbf{i}\sin\phi + \mathbf{j}\cos\phi)\,d\phi \qquad (2.13)$$

where **i** and **j** are the unit vectors along the *x* and *y* axis, respectively, and a is the coil radius. In spherical coordinates, $\boldsymbol{R}$ is represented by coordinates (r,θ,ϕ) and $\boldsymbol{R}'$ is represented by (r',θ',ϕ'). Then we can expand the denominator in Eq (2.11) in a series of spherical harmonics:

$$\frac{1}{4\pi}\frac{1}{|\boldsymbol{R}-\boldsymbol{R}'|} = \sum_{l=0}^{\infty}\frac{f_l(r,r')}{2l+1} \times \sum_{m=-l}^{m=l} Y_l^{m*}(\theta',\phi')\,Y_l^{m}(\theta',\phi') \qquad (2.14)$$

where $f_l(r,r') = \begin{cases} \frac{1}{r}\left(\frac{r'}{r}\right)^l, & r > r' \\ \frac{1}{r'}\left(\frac{r}{r'}\right)^l, & r < r' \end{cases}$.

$d\boldsymbol{l}$ can be rewritten as:

$$d\boldsymbol{l} = a\left[\mathbf{i}\left(\frac{i}{2}\right)\left(e^{i\phi'} - e^{-i\phi'}\right) + \mathbf{j}\left(\frac{1}{2}\right)\left(e^{i\phi'} + e^{-i\phi'}\right)\right]d\phi' \qquad (2.15)$$

Substitute Eq (2.14) and Eq. (2.15) into the magnetic vector potential and let $r' = a$, $\theta' = \pi/2$, integrate over ϕ':

$$\boldsymbol{A} = \mu_0 I\pi a \sum_{l=1}^{\infty}\frac{f_l}{2l+1}\{\mathbf{i}i[Y_l^1(\theta,\phi)Y_l^{1*}\left(\frac{\pi}{2},0\right) - Y_l^{-1}(\theta,\phi)Y_l^{-1*}\left(\frac{\pi}{2},0\right)] +$$

$$\mathbf{j}[Y_l^1(\theta,\phi)Y_l^{1*}\left(\frac{\pi}{2},0\right) + Y_l^{-1}(\theta,\phi)Y_l^{-1*}\left(\frac{\pi}{2},0\right)]\} . \qquad (2.16)$$

The above equation uses the orthogonality property of spherical harmonics:

$$\int_0^{\pi} Y_l^{m'*}(\theta',\phi')e^{im\phi'}\,d\phi' = 2\pi Y_l^{m*}(\theta,0)\delta_{m'm} .$$

The electric field in the medium is given by:

$$\boldsymbol{E} = -\frac{\partial \boldsymbol{A}}{\partial t} \qquad (2.17)$$

and it is related to the current density by the medium conductivity σ:

$$\boldsymbol{J} = \sigma\boldsymbol{E} . \qquad (2.18)$$

Then the time-averaged dissipated power in a volume dV can be written as:

$$dW = \frac{1}{2} \boldsymbol{J}^* \cdot \boldsymbol{E} \, dV \ . \qquad (2.19)$$

And the total time-averaged power dissipation in the medium is found to be:

$$W = \frac{1}{2} \sigma \omega_0^2 \int \boldsymbol{A} \cdot \boldsymbol{A}^* \, dV \ . \qquad (2.20)$$

The differential volume in spherical coordinates is given by:

$$dV = r^2 dr \, d\Omega$$

with the differential solid angle to be:

$$d\Omega = \sin\theta \, d\theta \, d\phi \ .$$

The following properties of spherical harmonics are used to solve the integration:

$$\int_{4\pi} Y_l^m(\theta, \phi) \, Y_{l'}^{m'}(\theta, \phi) \, d\Omega = \delta_{mm'} \delta_{ll'} \text{ and } Y_l^{-m} = (-1)^m Y_l^{m^*} \ .$$

We then have:

$$\int \boldsymbol{A} \cdot \boldsymbol{A}^* \, d\Omega = (\pi \mu_0 I_0 a)^2 \times \sum_{l=1}^{\infty} \left(\frac{f_l}{2l+1}\right)^2 \times \left[4 Y_l^{1^*}\left(\frac{\pi}{2}, 0\right) Y_l^1\left(\frac{\pi}{2}, 0\right) \right]. \qquad (2.21)$$

In the actual case, since the medium is usually placed on only one side of the coil, factor 4 can be replaced by 2. The integration with respect to r can be evaluated as:

$$\int f_l^2 r^2 dr = \int_0^a \frac{1}{a^2} \left(\frac{r}{a}\right)^{2l} r^2 dr + \int_a^\infty \frac{1}{r^2} \left(\frac{a}{r}\right)^{2l} r^2 dr = \left(\frac{1}{2l+3} + \frac{1}{2l-1}\right) a \ . \qquad (2.22)$$

Substituting Eqs. (2.21) and (2.22) into the total time-averaged power dissipation Eq. (2.20) gives:

$$W = \sigma \, (\omega_0 \mu_0 I_0 \pi)^2 a^3 \sum_{l=1}^{\infty} \left(\frac{1}{2l+1}\right)^2 \left(\frac{1}{2l+3} + \frac{1}{2l-1}\right) \times Y_l^{1^*}\left(\frac{\pi}{2}, 0\right) Y_l^1\left(\frac{\pi}{2}, 0\right). \qquad (2.23)$$

The summation can be approximated by a constant value:

$$\sum_{l=1}^{\infty} \left(\frac{1}{2l+1}\right)^2 \left(\frac{1}{2l+3} + \frac{1}{2l-1}\right) \times Y_l^{1^*}\left(\frac{\pi}{2}, 0\right) Y_l^1\left(\frac{\pi}{2}, 0\right) \approx 0.0166 \ . \qquad (2.24)$$

Thus, the effective sample resistance is given by:

$$R_{sample} = \frac{W}{I_0^2} = 0.0332\sigma(\omega_0\mu_0\pi)^2 a^3 \approx \frac{1}{3}\sigma\mu_0^2\omega_0^2 a^3. \qquad (2.25)$$

The sample and coil were kept the same in a constant 3T MRI scanner when we compared the SNR improvement, with the medium conductivity, the resonance frequency, and the coil radius remaining unchanged. Therefore, the sample noise R_{sample} was the same when evaluating the SNR at various coil orientations, and we can focus on the transverse B_1 field to characterize the SNR improvement factor.

2.3.5. The effective transverse coil field $B_{1xy \ effective}$

As introduced in Chapter 1, transmit coils emit RF pulses (B_1^+) to excite the net magnetization of the spin system away from its initial alignment with the main magnetic field (B_0), generating a transverse precessing magnetization [8]. This results in an induced current in the receiving coil. The strength of the induced current depends on not only the distance from the target but also the orientation of the coil with respect to the magnetization direction [94]. According to Maxwell's equation (2.1b), the induced current should be proportional to the rate of change of the flux density of the magnetic field passing through the coil. The net flux is defined as the sum of the perpendicular components of the magnetic field traversing the surface enclosed by the circular coil. When the static magnetic field is in the $+z$ direction and disturbance is sent in the MRI scanner in the y direction, the magnetization will rotate in the x-y plane with the rotation axis to be the z-axis.

As shown in Figure 2.8, when the coil axis is along the x-axis or y-axis, the magnetic flux sweeps across the coils and generate a periodic signal with the resonance frequency. The maximum signal can be produced when the axis of the coil is perpendicular to the axis of rotation since it has the largest flux change as the magnetization precesses [94]–[96]. On the

other hand, if the coil is placed with its axis parallel to the axis of rotation, no flux change can be detected by the coil in an idealized case and the MR signal is zero. However, in the actual case, coils have components in directions other than the direction orthogonal to the coil face, so there will be some sensitivity in other directions.
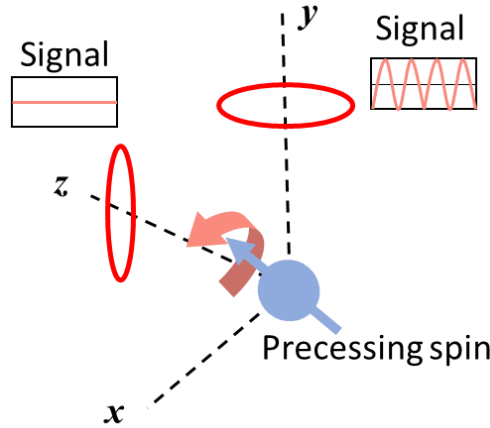
Figure 2.8: *Signals induced in coils as illustrated in* [94]. *When the spin is rotating in the x-y plane, the coil along the y-axis shows oscillating signals while no current is induced in the coil along the z-axis.*

To study the coil SNR at various orientations, we derived the B_1 field at the region of interest from the magnetic field simulation in COMSOL. As illustrated in Figure 2.9, B_0 is in the +z-axis. When the coil is lying in the x-z plane, the axis of the coil is perpendicular to the axis of rotation for the spin system, which should provide the strongest signal with an effective B_1 field = $B_{1\ xy}$. As the coil and the phantom rotate at a certain angle θ respect to the static field B_0, the effective B_1 field will be the magnetic field B_1 projected onto the x-y plane. When θ reaches 90°, the axis of the coil becomes parallel to the B_0 field, where we expect to get the lowest SNR and effective B_1 field should be $B_{1\ xz}$. The amplitude of the effective transverse field at a certain rotation angle θ (0°≤ θ ≤90°) with respect to B_0 was derived as:

$$B_{1y\ effective} = B_{1y} \cdot cos\theta - B_{1z} \cdot sin\theta \qquad (2.26)$$

$$B_{1xy\ effective} = \sqrt{B_{1x}B_{1x}{}^* + B_{1y\ effective}B_{1y\ effective}{}^*} \qquad (2.27)$$

where B_{1x}, B_{1y}, and B_{1z} are the magnetic field components for the RF receiving coil in *x, y,* and

z directions at $\theta = 0°$. B_{1x}, B_{1y}, and B_{1z} remain constant during the rotation.
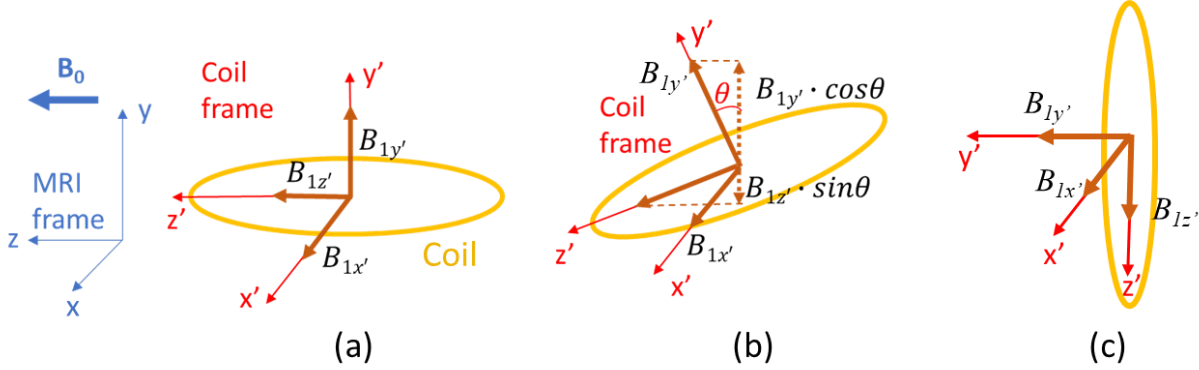
Figure 2.9*: Coil rotation illustration. B₀ is in the +z axis. a: The coil resides in the x-z plane at θ = 0°. b: The coil is rotated around the x-axis at an angle, θ, where: 0°≤ θ ≤ 90°. c: The coil is rotated at θ = 90°.*

Chapter 3: Phantom study & simulation validation

3.1. Agar gel phantom study

3.1.1. Phantom construction

To characterize the coil performance, we designed a phantom system with a similar dimensions of the human head and the sphenoid sinus cavity (Figure 3.1). A cylindrical jar allowed for easy rotation of the assembly so that the coil could be easily placed at a certain rotation angle relative to the B_0 field. An igloo-shaped configuration was 3D printed and mimicked the sphenoid sinus. To evaluate imaging resolution, a resolution with five holes, ranging from 1 mm to 2.8 mm in diameter, was designed and attached under the igloo cavity. The holes were drilled into a 2.5cm thick, 7.5 cm wide acrylic plate. Another hole with a 12.7 mm diameter was drilled at the center of the resolution plate to provide ample signal for reliable SNR measurements. As the average width of the pituitary gland is around 10 mm [97]–[99], the 12.7 mm hole provides sufficient volume coverage to assess the coil performance on pituitary gland imaging. The cavity and the resolution plate were fixed inside the transparent cylindrical plastic jar parallel to the jar wall. The plastic jar was placed on a pair of 3D-printed supporters, enabling the jar to be rotated and set at the desired scan angle.

The plastic jar and the holes in the resolution plate were filled with agar gel. We followed the recipe presented in [100] to prepare the phantom. The phantom consists of distilled water, agar powder, Kappa carrageenan, and gadolinium contrast.
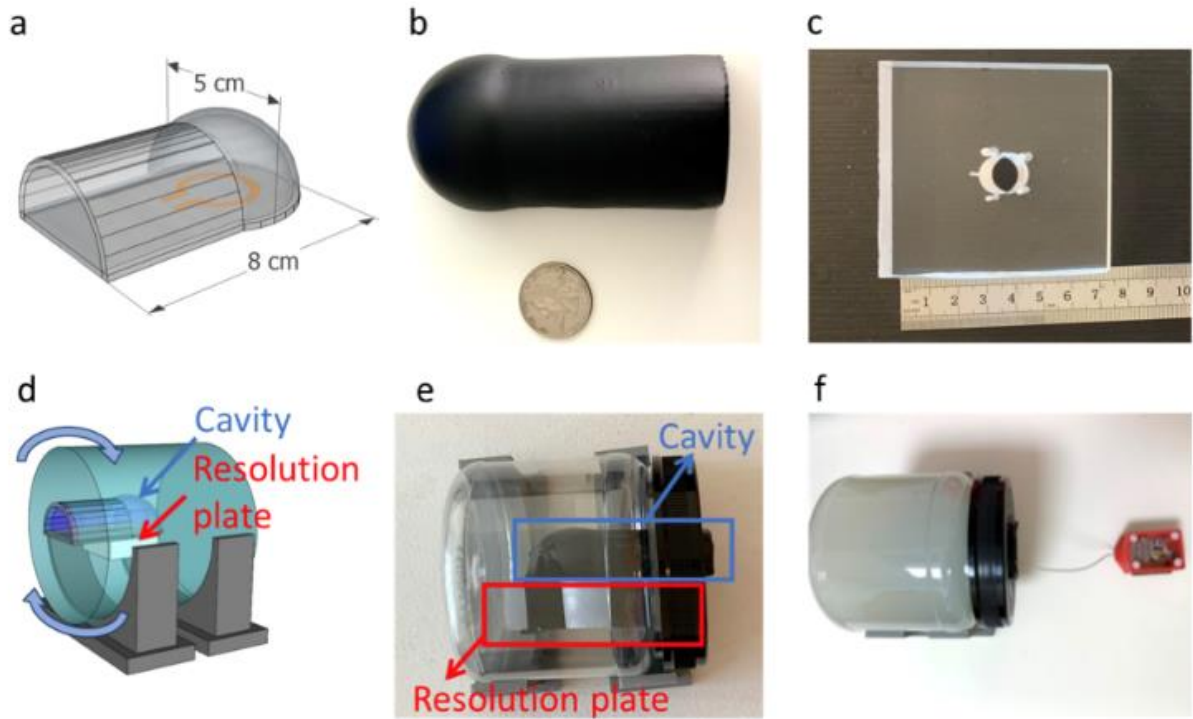
Figure 3.1: Phantom system setup, including the igloo cavity, resolution plate, and agar phantom. a: CAD model of the igloo cavity. The coil was placed inside the cavity. b: The 3D-printed igloo cavity. The cavity was waterproofed with Plasti Dip (Plasti Dip Int., Minneapolis, MN, USA). A U.S. quarter is shown for reference. c: The resolution plate with hole diameters 1 mm, 1.6 mm, 2 mm, 2.4 mm, 2.8 mm, and 12.7 mm. The smaller holes were used for visual demonstration, and the 12.7 mm hole was used for SNR calculation. d: CAD model of the phantom setup. The cavity was fixed inside a plastic jar and then placed on two 3D-printed supporters, allowing the jar to be set to the desired coil angle. e: Assembled phantom set up. The resolution plate was taped tightly under the cavity, and then the cavity was fixed in a plastic jar. f: The plastic jar was filled with agar gel, and the coil was placed inside the cavity [1].

Table 3.1: Components of the agar gel phantom

Component	Weight (%)	Weight (g)
Distilled water	96	1440
Kappa carrageenan	3	45
Agar powder	1	15
Gadolinium contrast	< 0.01	33×10^{-6} (33 μg/ml, 1 ml)
Sum	100	1500

The procedures to prepare the phantom:

1) Weigh all the components. Add the distilled water into a 2 L beaker. Add all other components into the water and heat the mix up to 90 °C (nearly boiling).

2) Maintain the temperature of the mixture at 90 – 100 °C. Continuously stir the mixture until the components dissolve.

3) 10 drops of anti-foaming solution can be added to decrease the bubbles.

4) Turn off the hot plate and let the mixture cool down. Continuously stir the mixture during cooling.

5) When the mixture temperature is below 60 °C, pour the gel into the plastic jar. Put the lid back (the cavity and the resolution should already be fixed on the cap).

6) Tighten the cap and seal it with tape.

3.1.2. MRI scan for the agar gel phantom

A real-time tune and match process to ensure the coil performance after the coil was placed inside the igloo cavity of the phantom. A portable vector network analyzer (VNA) (DG8SAQ VNWA 3, SDR-Kits, United Kingdom) was used to tune and match the coil by measuring the frequency response for loaded and unloaded cases. (Figure 3.2). Loaded S11 was measured with the phantom placed under the coil, while unloaded S11 was measured with the coil in the air. The miniature coil was tuned to the resonance frequency of 123.2 MHz and matched to the pre-amplifier impedance for both loaded and unloaded cases.
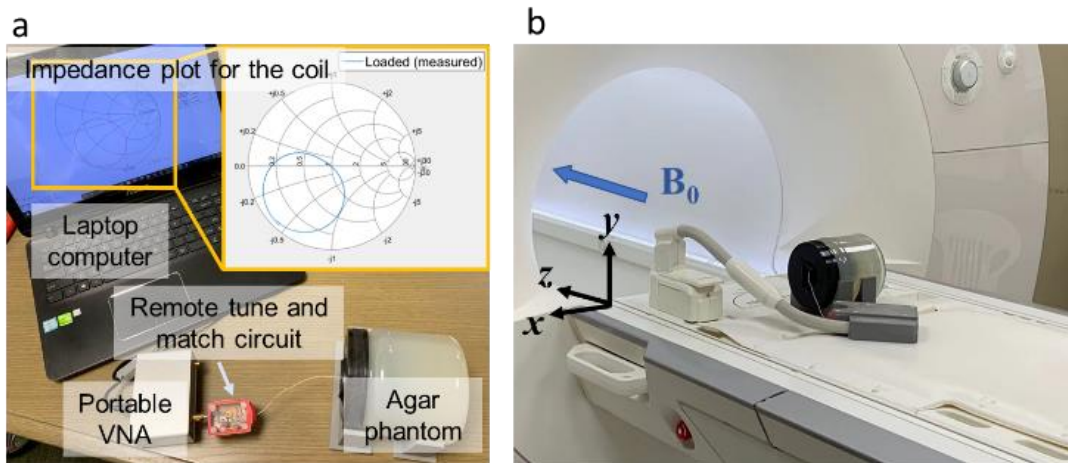
Figure 3.2: *The tune and match process and the MRI scan experiment setup. a: A portable vector network analyzer (DG8SAQ VNWA 3, SDR-Kits, United Kingdom) was used for the tune and match analysis after placing the coil inside the agar phantom. b: The tune and match box was connected to the pre-amplifier, and MRI scans were performed on the phantom* [1].

The T1/T2 value of the agar phantom was measured to be 1250/64 ms, with T1/T2 map sequences [101]. Standard resolution proton density Turbo Spin Echo (SD PD-TSE) sequences (Table 2.2) were used on both the miniature coil and the commercial Siemens 20-channel HeadNeck coil. The performance of the two coils was compared. The proton density sequence was chosen because it is a direct measure of the maximum signal and is therefore readily compared to the simulation results. The 2D SD PD-TSE sequence was scanned at 10 different coil rotation angles, ranging from 0 ° to 90°.

A 2D high-resolution proton density Turbo Spin Echo (HD PD-TSE) sequence (Table 2.2) was also performed at 0° and 60° coil angles to show the expected higher SNR. Images were reconstructed from the frequency data directly via inverse Fast Fourier Transform (iFFT). The HD PD-TSE scan was used on the miniature coil and the commercial head coil to compare the performance. The commercial head coil images were sum-of-square combined after coil reduction.

Table 3.2: *The parameters for standard-resolution PD-TSE sequence and high-resolution 2D PD-weighted TSE sequence* [1].

	SD PD-TSE	HD PD-TSE
Echo time (ms)	9.1	14
Repetition time (ms)	3000	3000
Refocusing angle (degree)	160	160
Bandwidth (Hz/pixel)	250	250
Acquisition matrix size	320×320×15	320×320×35
Field of view (mm^3)	220×220×45	64×64×25
Resolution (mm^3)	0.7×0.7×3	0.2×0.2×0.7
Phase oversampling	0%	100%
Scan time (mm:ss)	03:09	06:21
Parallel imaging	No	No

3.1.3. Scan SNR computation

At each coil rotation angle, SNR measurements for the single-channel miniature coil were calculated from two repeated standard-resolution 2D PD-TSE scans. The region of interest (ROI) was divided into five cylindrical slices inside the resolution plate center hole below the coil, with 1 cm diameter and 3 mm thickness (Figure 3.3). The target depth was chosen to be 3 mm to 18 mm away from the miniature coil.
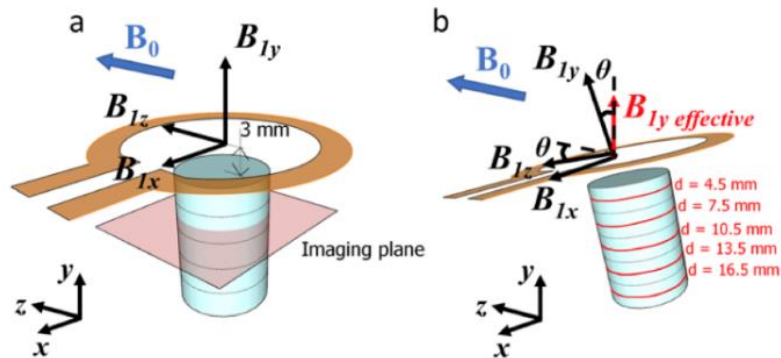
Figure 3.3: *The blue cylinders represent the region of interest (ROI) at various distances d from the coil. B_0 is in the +z axis. a: The coil resides in the x-z plane at θ = 0°. b: The coil is rotated around the x-axis at an angle, θ, where: 0° < θ ≤ 90°* [1].

The scan SNR measurements for the miniature coil were calculated based on the methods described by Constantinides et al. for magnitude images of a single-coil array [102]. SNR was defined as the ratio of signal and noise ($SNR = S / \sigma$). The signals were measured as the mean intensity within the ROI:

$$S = \frac{1}{N_{ROI}} \sum_{i=1}^{N_{ROI}} A_{ROI_i} \qquad (3.1)$$

where N is the number of samples, and A is the pixel intensity. The noise was measured as the background standard deviation on a signal-free region:

$$\sigma = \sqrt{\frac{1}{N_n} \sum_{i=1}^{N_n} \left(A_{n_i} - \overline{A_{n_i}} \right)^2} \qquad (3.2)$$

For our phantom scan, the signal-free region was selected in the region of the acrylic plastic part on the resolution plate.

For the 20-channel commercial head coil, the SNR was calculated based on Kellman's method for root-sum-of-squares magnitude combining images, which is the standard method for multi-channel phased array coils [103]. The scaled noise covariance matrix was calculated from the average pixel SNR within ROI from two repeated standard-resolution 2D PD-TSE scans.

3.2. Single loop coil simulation and phantom experiment results

Standard-resolution proton density Turbo Spin Echo (PD-TSE) MRI scans were performed with the agar gel phantom for SNR measurements. The results for the miniature flexible coil and commercial head coil were compared, and a coil simulation model was developed to characterize the performance of the coil. We plotted the SNR maps and the amplitudes of the simulated effective transverse B_1 field distributions for θ from 0° to 90° at

defined ROIs from 4.5 mm to 16.5 mm distance to the coil, shown in Figure 3.3.

3.2.1. S11 comparison
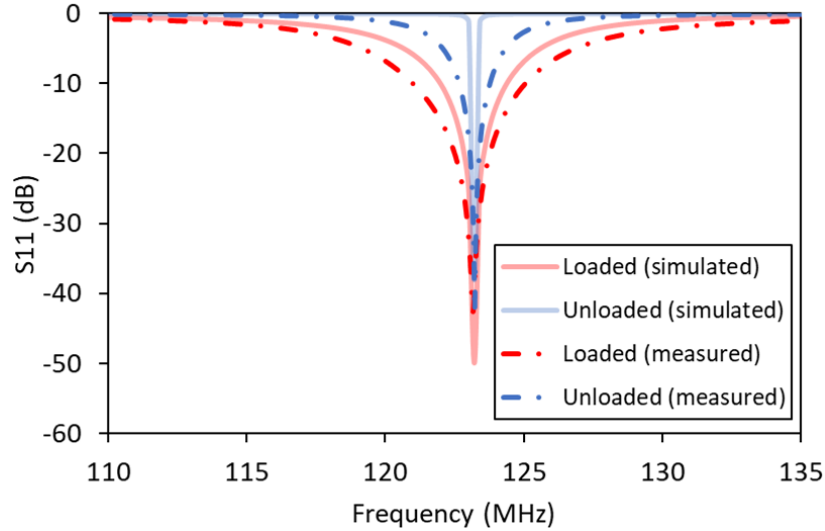
Figure 3.4: *Comparison of S11 with and without the load measured with the VNA and simulated using COMSOL. The coil in both loaded and unloaded cases was tuned and matched to the resonance frequency* [1].

We first characterized the coil electrically. Tuning the coil to the resonance frequency and matching the impedance to the pre-amplifier can assure the optimal coil efficiency and SNR. The measured reflection coefficient S11 was recorded and compared with the simulated S11 for the loaded and unloaded cases. As shown in Figure 3.4, the simulated S11 generally agrees with the measured S11. In all cases, the coil was tuned to the resonance frequency at 123.2 MHz. The quality factor Q-factor can be approximated as described in section 2.3.3. The loaded Q-factor (with the phantom placed under the coil) is given as:

$$Q_{loaded}^{mea} = \frac{f_0}{\Delta f} = \frac{123.2\ MHz}{128.6\ MHz - 117.6\ MHz} = 11.2 \qquad (2.15)$$

And the Q-factor for an unloaded case (without sample/ phantom) is

$$Q_{unloaded}^{mea} = \frac{f_0}{\Delta f} = \frac{123.2 \ MHz}{124.8 \ MHz - 121.4 \ MHz} = 36.2 \qquad (2.16)$$

The measured quality factors are lower than the simulated ones in section 2.3.3. This is likely to result from the environment loss that was not included in the simulation. Q-ratio can be calculated to assess coil sensitivity. The measured Q-ratio is found to be $Q_{ratio}^{mea} = \frac{Q_{unloaded}}{Q_{loaded}} = 3.23$. A Q-ratio larger than 2 indicates that the sample noise dominates the coil noise [8].

3.2.2. In-plane SNR map

As shown in Figure 3.3, imaging planes were set to be the planes that are parallel to the coil surface. In-plane phantom scan SNR maps selected at 4.5 mm and 10.5 mm below the coil as zoom-in shots on the resolution plate are shown in Figure 3.5. The amplitudes of the simulated effective transverse B_1 field distributions at the same coil depth distance and rotation angles as the SNR maps are also shown in Figure 3.5. In the simulation, the in-plane effective field amplitudes were normalized based on the maximum $B_{1xy \ effective}$ field at 4.5 mm below the coil.

As the coil angle increases, the overall SNR and the amplitude of the $B_{1xy \ effective}$ within the ROI decrease. Because of the circular shape of the small coil, the magnetic field from the coil is not uniform. The magnetic field near the coil trace is higher than the field at the coil center. And dead spots, which are the low signal regions, were found in the in-plane results. When the rotation angles increased from 0° to 90°, the dead spot gradually moved from the edge of the ROI to the center of the ROI in both the experiment and simulation. The dead spots were located at where the coil field B_1 field is mostly parallel to the main field B_0 field as shown on Figure 3.6. At these locations, B_1 is in the z direction, thus $B_{1x} = B_{1y \ effective} = 0$, leading to $B_{1xy \ effective} =$

$\sqrt{B_{1x}{}^2 + B_{1y\ effective}{}^2}$ dropping to zero and dead spots being presented. The simulated field

distributions qualitatively matched with the scan experiment SNR maps.
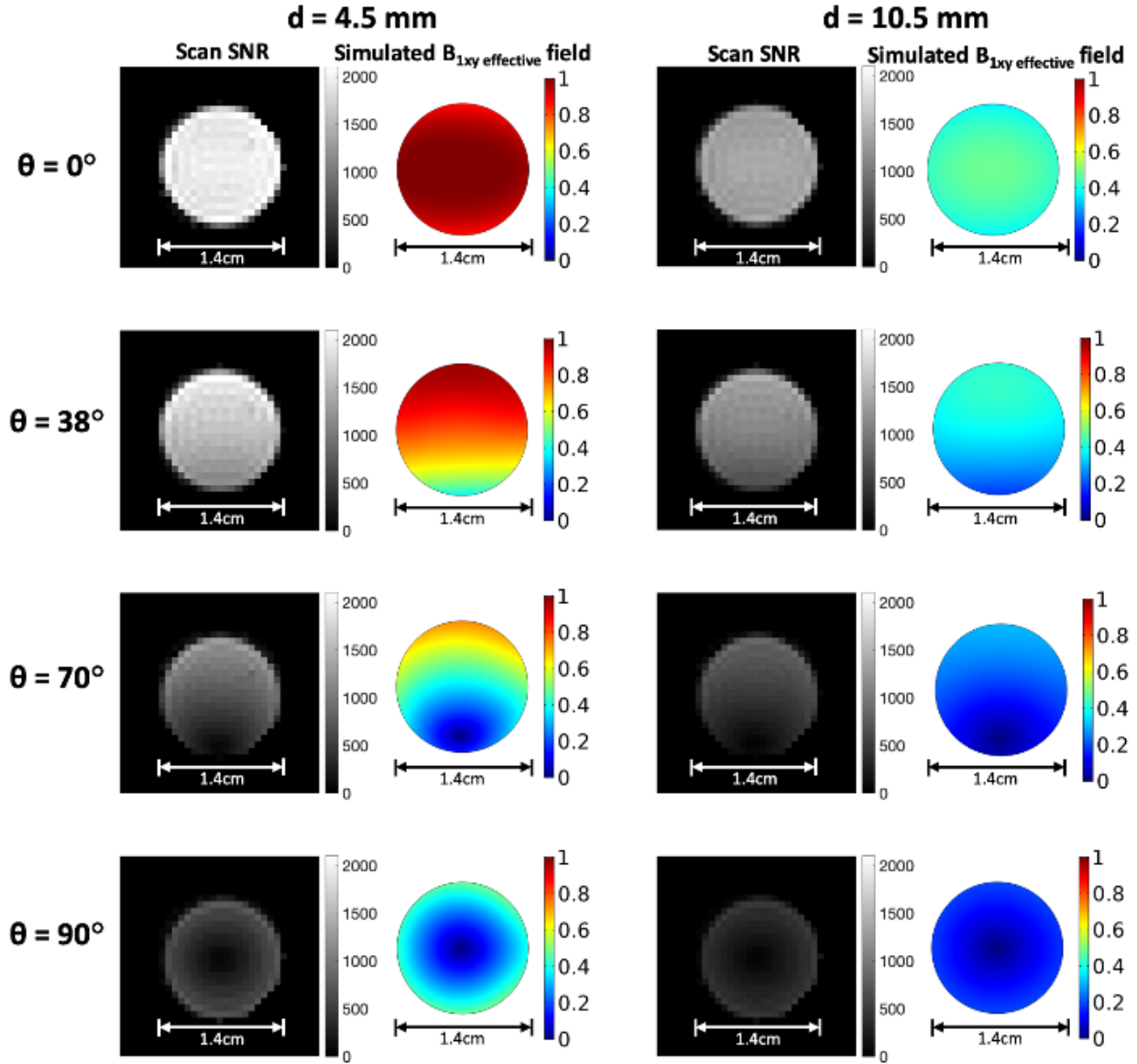
Figure 3.5*: The standard-resolution PD-TSE scan (Table 3.2 line 1) signal SNR maps and normalized amplitude of the simulated effective transverse B_1 field distributions at $\theta = 0°$, $38°$, $70°$ and, $90°$, respectively. d indicates the distance between the coil and the imaging plane. The imaging planes were selected to be parallel to the coil plane. Columns 1&3: The SNR maps at the respective coil distances d and rotation angles θ. Column 2&4: The amplitudes of the simulated effective transverse B_1 field distributions at the central hole on the resolution. Linear color scale indicates the level of the SNR and the normalized $B_{1xy\ effective}$. The simulation fields were normalized based on the maximum $B_{1xy\ effective}$ field at d = 4.5 mm [1].*

Figure 3.6: Dead spots location illustrations. The dead spots are located at where the B_1 field is mainly parallel to the B_0 field.

Scan images from the high-resolution PD-TSE scan (Table 3.2 line 2) using the commercial head coil and the miniature coil are shown in Figure 3.7. Though the SNR decreases with increasing rotation angle, the phantom scan shows a relatively high signal intensity from the miniature coil even at 60° coil angle, and the image SNR is high enough to show the 1 mm hole on the resolution plate clearly. On the other hand, the commercial coil SNR is so low that the 1 mm can hardly be identified on the high-resolution image.
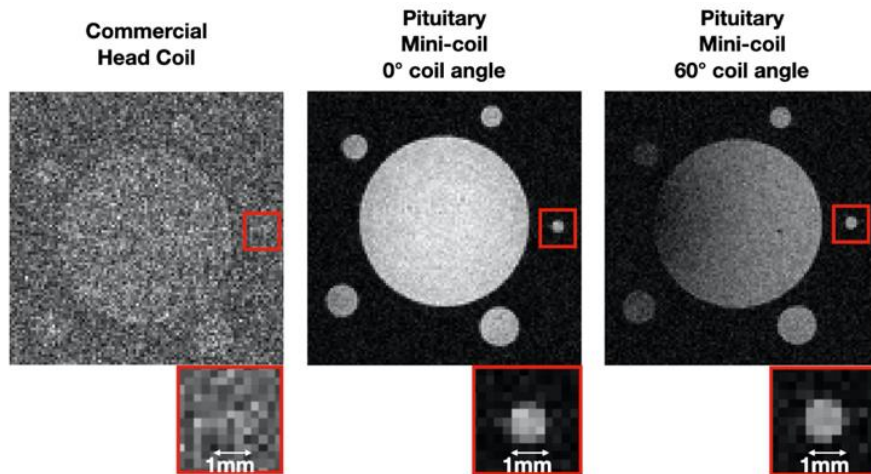
Figure 3.7: High-resolution PD-TSE image comparisons, using the commercial head coil (left) and the pituitary miniature flexible coil at θ = 0° (middle) and θ = 60° (right). The voxel size is 0.2 × 0.2 × 0.7 mm³. Imaging planes were selected 1 cm from the coil. Images from the miniature flexible coil are at the same window level, while the image from the commercial head coil is at its own window level for better visualization [1].

3.2.3. Mean SNR vs. coil distance & rotation angle

The mean SNR of the ROI from the phantom scan with respect to distance from the coil and the rotation angles are shown in Figure 3.8. The normalized mean $B_{1xy\ effective}$ within the ROI from the simulation is also plotted and compared with the scan results. The effective transverse field predicted by simulation was normalized at a single point ($\theta = 0°$ at 4.5 mm below the coil), and no further normalization was performed. By setting this one point equal to the experimentally measured SNR, we can see that the simulations of magnetic field amplitude match with the experimentally measured SNR, with an error of 1.1% ± 0.8%.
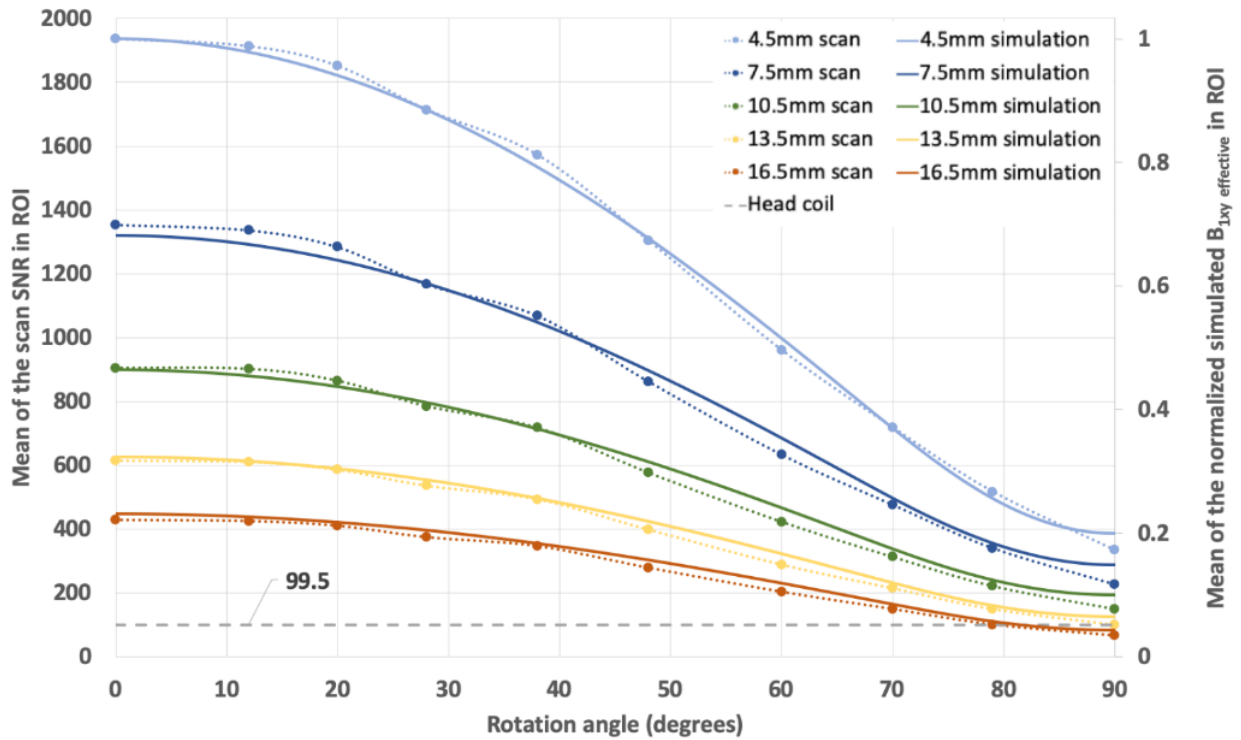
Figure 3.8: Mean SNR from the scan at various ROI depths and rotation angles, compared with the corresponding mean of the normalized effective transverse B₁ field from the simulation. The simulated fields were normalized to a single point, the mean B₁xy effective at θ = 0° at 4.5 mm below the coil [1].

The effective field decreases with the rotation angles. For all ROI depths, the mean effective field at $\theta = 90°$ dropped to around 20% of the mean field found at $\theta = 0°$. The effective

field also decreases with the target depth. At $\theta = 0°$, the mean effective field at the 16.5 mm slice was 23.1% of the mean effective field at the 4.5 mm slice. In the ideal case, at $\theta = 90°$, the coil magnetic field B_1 is parallel to the main field B_0, and the SNR is expected to drop to zero. However, in the actual case, only the B_{1y} component of the coil field is parallel to B_0 at $\theta = 90°$ (Figure 2.9 (c)), and spins can still be excited by B_{1x} and B_{1z} components, producing a reduced but detectable signal. The mean SNR of the 20-channel commercial head coil based on Kellman's method was 99.5 (Figure 3.8) [103] and was uniform across the ROI at different rotation angles.

A Bland-Altman plot of two repeated standard-resolution PD-TSE scans was plotted to show the inter-scan SNR consistencies (Figure 3.9). The 95% confidence interval demonstrates the consistency and the repeatability of measured SNRs from phantom scans.
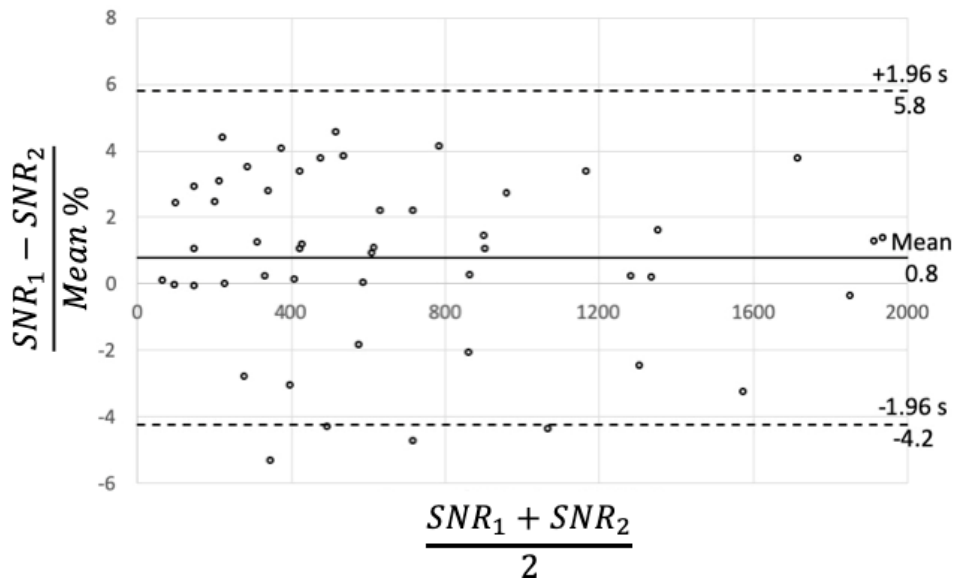
***Figure 3.9**: Bland-Altman plot for SNR of two repeated SD PD-TSE scans, SNR$_1$ and SNR$_2$. The x-axis is the mean of the two scans, and y-axis is the percentage difference* [1].

3.2.4. Surgical placement prediction

The cross-validated numerical simulation model of the coil is not only valuable for further optimizing the coil in the future but can also be used to help select an optimal coil from a

predetermined range of coil shapes and sizes and predict the potential SNR improvement. An example hypothetical miniature coil surgical placement with the simulated SNR improvements in the pituitary region is shown in Figure 3.10. In this zoom-in image of the sphenoid sinus and the pituitary, the 2.6 cm miniature coil can be placed at a 30° angle with respect to the B_0 field. Both coil placement and pituitary gland contour were drawn by an experienced neurosurgeon. The gradient contour line plots represent the predicted SNR improvement factors of our coil compared to the commercial head coil, which was estimated based on the mean SNR results from the scan of the miniature coil and the commercial head coil described in section 2.6.3. In this specific example, we predict to see 12 to 19 times SNR improvement at the region of the pituitary gland that is close to the coil, and at least 3 times SNR improvement at the region further away.
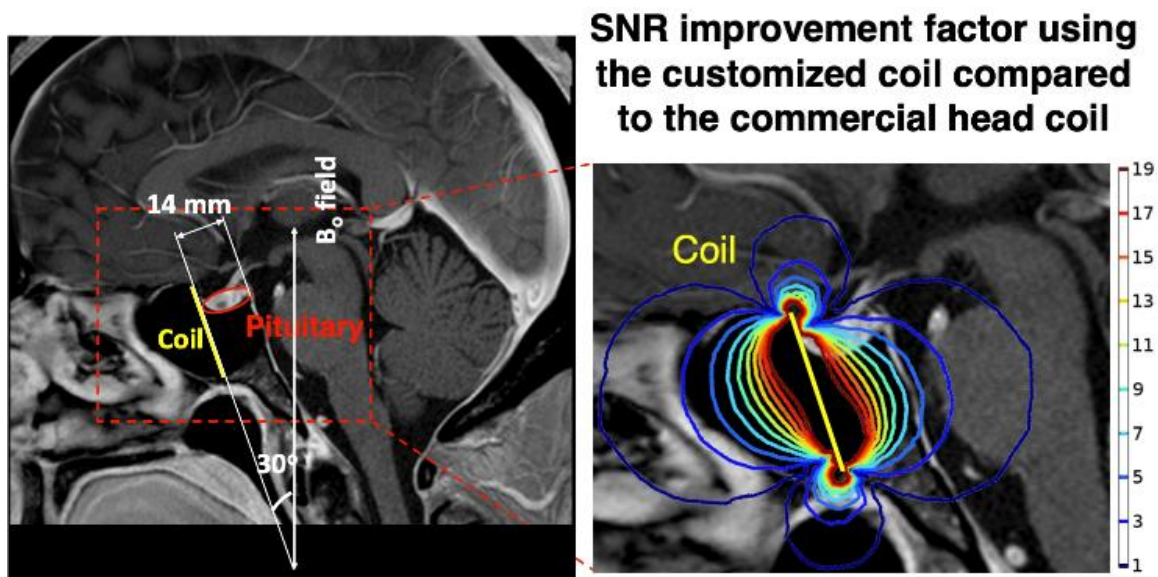
Figure 3.10: *Coil surgical placement example on the retrospective patient image. SNR improvement using the miniature coil compared to a commercial head coil was estimated using the simulated effective field at θ = 30°. The red ellipse indicates the location of the pituitary gland* [1].

3.3. Butterfly coil design & simulation

As we can see in section 3.2.2, "dead spots" were found in the SNR maps and the simulated B_1 field distributions. The dead spots were observed at the locations where the coil field B_1 is parallel to the MRI main field B_0 (Figure 3.6). At these locations, little or no spins were excited and thus, the signal dropped significantly. This low signal region is a common issue observed in MRI images when using the single loop coil and limits the placement region of the coils. This limitation can possibly be circumvented by using coils with a transverse B_1 field at the center of the coil, such as the butterfly coils or figure-of-eight coils [29], [104]. The benefit of butterfly coils is that their orthogonal sensitivity to the loop coil might be beneficial in some patients. In this section, we performed an exploration of the potential for butterfly coils using simulation. The simulation shows that the butterfly coil appears to have reduced overall SNR performance compared to the single loop in the pituitary gland region and thus may not be the optimal design for this application.

3.3.1. Numerical optimization of the butterfly coil

Due to the physical limitation of the sphenoid sinus, a circular shape butterfly coil was designed and optimized through numerical simulation. The coil geometry and current flow on the 2-layer coil are illustrated in Figure 3.11 (a). Since the current flows in opposite directions in the two loops, the magnetic fields in the vertical direction are canceled, and the main field is in the transverse direction (Figure 3.11 (b)). A 3D electromagnetic field simulation was developed in COMSOL in the frequency domain. A Perfect Electric Conductor boundary was assigned to the coil surface, and lumped elements (inductors and capacitors) were arranged on the coil trace for tuning and matching. All the coil models with various geometry designs were tuned to the 123.2

MHz resonance frequency of the 3 T MRI. A uniform lumped port was fed on the coil trace for excitation. The simulated coil field B_1 field was exported from COMSOL and imported into MATLAB (The MathWorks, Inc., Natick, Massachusetts, United States) for post-processing.
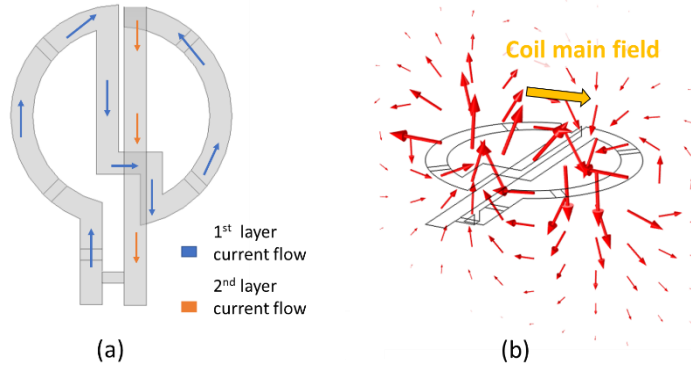
Figure 3.11: *The designed butterfly coil schematics. (a) The current flow direction on the 2-layer coil design. (b) The simulated magnetic field of the butterfly coil.*

The optimal distance of the gap between the center two legs of the butterfly coil (Figure 3.12 (a)) was first determined by examining the effective B_{1xy} field amplitude along the coil center axis, which is perpendicular to the coil plane, up to a depth of 20 mm beneath the coil (Figure 3.12 (b)). The distances of the gap on the coils ranged from 0.5 mm to 10 mm, while the radius of the coils was fixed at 10 mm. The magnetic field was normalized based on the effective B_{1xy} field for the coil with a 0.5 mm gap distance at 0 mm depth.

To find the optimal radius of the designed butterfly coil at a certain target depth, we simulated the amplitude of the effective B_{1xy} field of coils with radius ranging from 10 mm to 50 mm at 2 mm increments. Small coils can fit in limited physical space (sphenoid sinus), but the diameter also needs to be large enough to provide sufficient coverage for the pituitary gland and keep the system in the sample noise dominates regime [1], [26]. At a given depth d ($0 \leq d \leq 90$ mm), the coil that provided the maximum effective B_{1xy} field on the center axis in the interval d to ($d + 1$ mm) was chosen to be the optimal coil for this depth d. A linear fitting was performed

to derive the relationship between the optimal radius and the target depth.
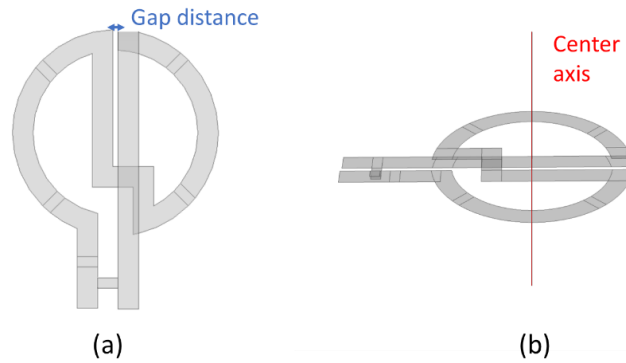
Figure 3.12: *(a) The gap between the center two legs of the butterfly coil is defined as the gap distance. (b) The magnetic flux density was examined along the center axis perpendicular to the coil plane.*

The effective B_{1xy} field from coils with 0.5 mm – 10 mm gap distance was simulated, and the optimal gap distance was determined. The effective B_{1xy} field increases as the coil gap distance decreases, and the field decreases as the depth increases. The optimal gap distance is found to be ≤ 2 mm. When the gap is smaller than 2 mm, a limited improvement in the effective B_{1xy} field was observed.
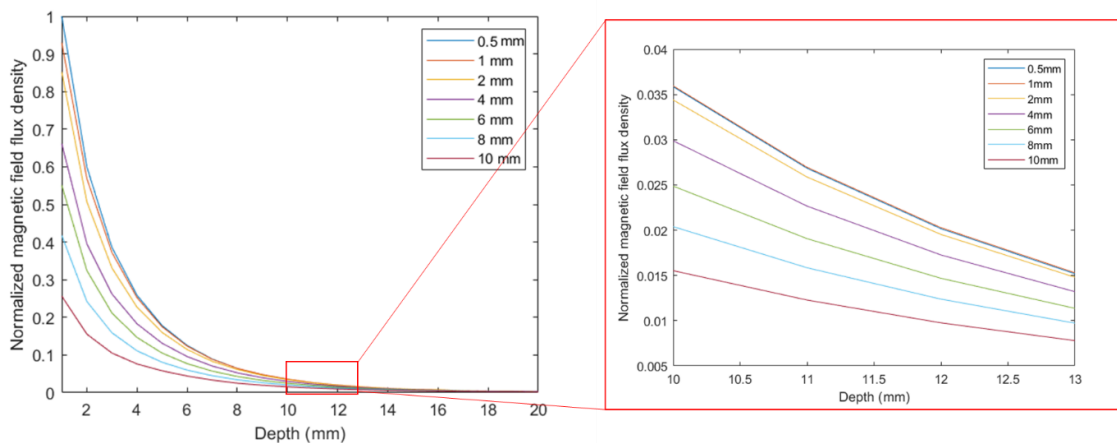
Figure 3.13: *The normalized effective B_{1xy} field from coils with 0.5 mm – 10 mm gap distance.*

The radius of the coil that provides the maximum effective B_{1xy} field amplitude at each depth built with a 2-mm gap distance is plotted in Figure 3.14. The linear relationship of best fit

47

to the data was given as

$$r = 0.45193d + 1.7747 \approx 0.5d + 1.8$$

where r is the optimal butterfly coil radius and d is the target depth. The size of the pituitary glands varies with the patients and physiological status. In general, the normal height of the pituitary gland is less than 8 mm, with some extreme cases being over 10 mm [105]. To fully cover the pituitary gland, the radius of the coil was chosen to be 10 mm for the following analysis.
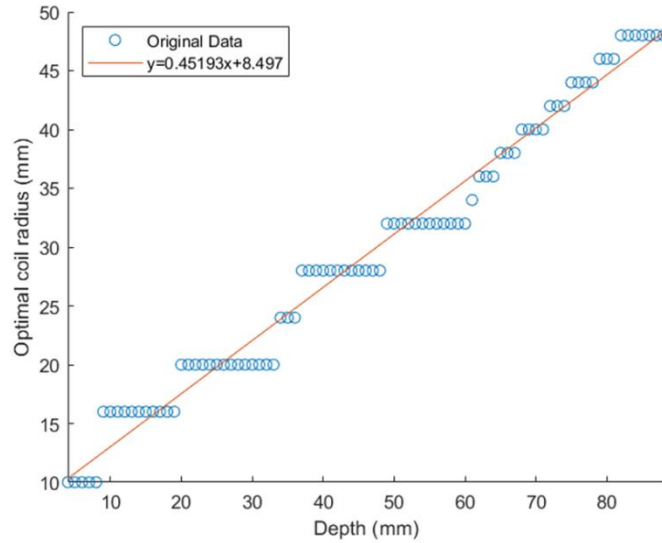
Figure 3.14: *Simulation of the butterfly coils producing the maximum effective B_{1xy} field for target depth $0 \leq d \leq 90$ mm along the coil center axis. The results are quantized because we simulated with discrete radius.*

3.3.2. Single loop coil vs. butterfly coil

To compare the performance of the two types of coils, we simulated the magnetic field from a 2-cm diameter single loop coil and compared it with the field from a 2-cm diameter butterfly coil. Both coils were tuned to the resonance frequency with a simulated S11 value < -30 dB. The same excitation was applied, and the same mesh size was assigned to both models. ROI was defined as cylinders with a 1.4-cm diameter and 3-mm thickness with a depth of 3 mm – 15

mm below the coil planes.

The in-plane effective B_{1xy} field at rotation angles of 0°, 45°, and 90° for both coils are shown in Figure 3.15. The image plane was selected at 3 mm below the coil planes. The field was normalized based on the maximum effective B_{1xy} field. As the rotation angle increased, a dead spot was found in the single loop coil image (Figure 3.15 (a)-(c)), while the butterfly maintained a high field amplitude at the center of the ROI at an even 90° rotation angle (Figure 3.15 (d)-(f)). The transverse-field butterfly coil preserves the signal at the center of the ROI at a near coil depth which can be helpful when an arbitrary coil orientation is required in the MRI scan. However, variation in the field distribution was also found within the ROI.
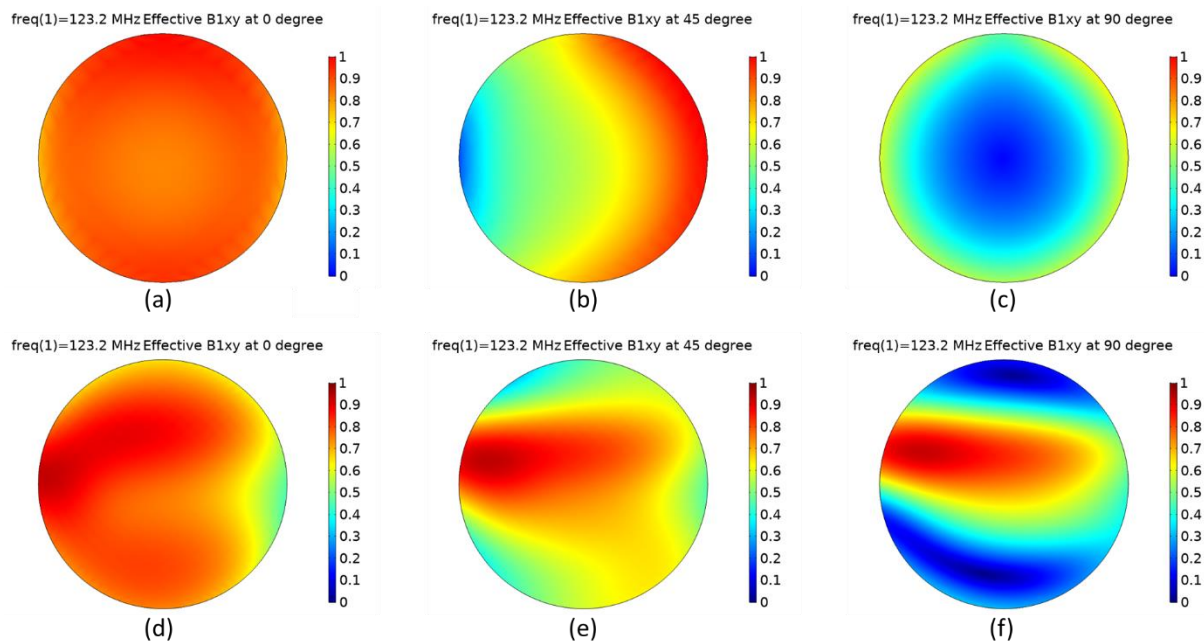
Figure 3.15: *The in-plane effective B$_{1xy}$ field at rotation angles of 0°, 45°, and 90° for (a)–(c) a 2-cm single loop coil, and (d)-(f) a 2-cm butterfly coil.*
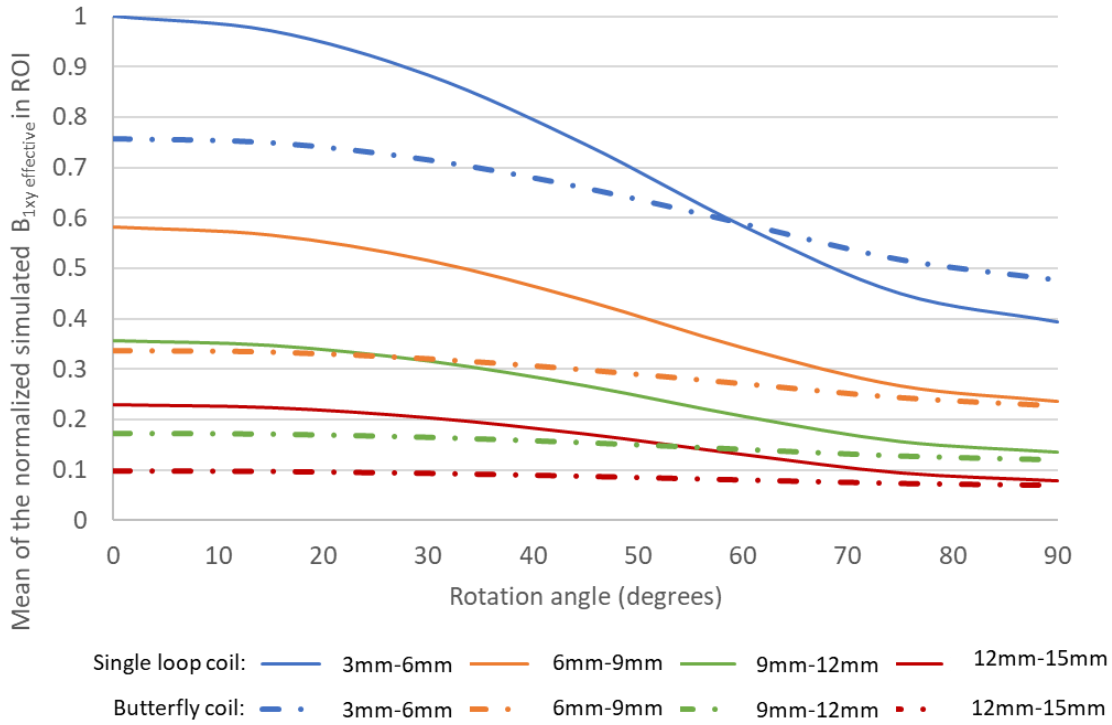
Figure 3.16: *Mean normalized effective transverse B_1 field from the simulation at various ROI depths and rotation angles for single loop coil and butterfly coil. The simulated fields were normalized to a single point, the mean $B_{1xy\,effective}$ at $\theta = 0°$ at 3 mm below the single loop coil.*

The average effective B_{1xy} field within the ROI at various depth and rotation angles was plotted in Figure 3.16. The simulated fields were normalized to a single point, the mean effective B_{1xy} field from the single loop coil at $\theta = 0°$ at 3 mm below the coil. In general, the butterfly coil showed a smaller variation in the mean effective field than the single loop coil as the rotation angle increased. The mean effective field for the butterfly coil at $\theta = 90°$ dropped to 60-70% of the mean field found at $\theta = 0°$, while the single loop coil at $\theta = 90°$ dropped to 20% of the mean field $\theta = 0°$. Although the butterfly coil field was more stable across different rotation angles, the mean effective field from the single loop coil was found to be generally higher than the butterfly coil. At 3 mm – 6 mm depth and $\theta = 0°$, the mean field of the butterfly coil was 75.6% of the mean field of the single loop coil, while at 12 mm – 15 mm depth, the mean field of the butterfly

coil was only 39.4% of the single loop coil. The butterfly coil exhibited a higher mean effective

B_{1xy} field than the single loop coil only when the rotation angle was larger than 60° at a 3 mm – 6

mm depth.

3.4. Temperature characterization on meat phantom

During the MRI scan, which uses electromagnetic waves for imaging, the radiofrequency

field from the transmit coil induces a current in the conductive material inside the human body.

The currents can heat up the surrounding tissue and impose a risk on the patients. To further

ensure the RF energy absorbed by the patient during the scan does not lead to thermal damage to

the tissue, we conducted temperature measurements with the mini coil.

(a)   (b)
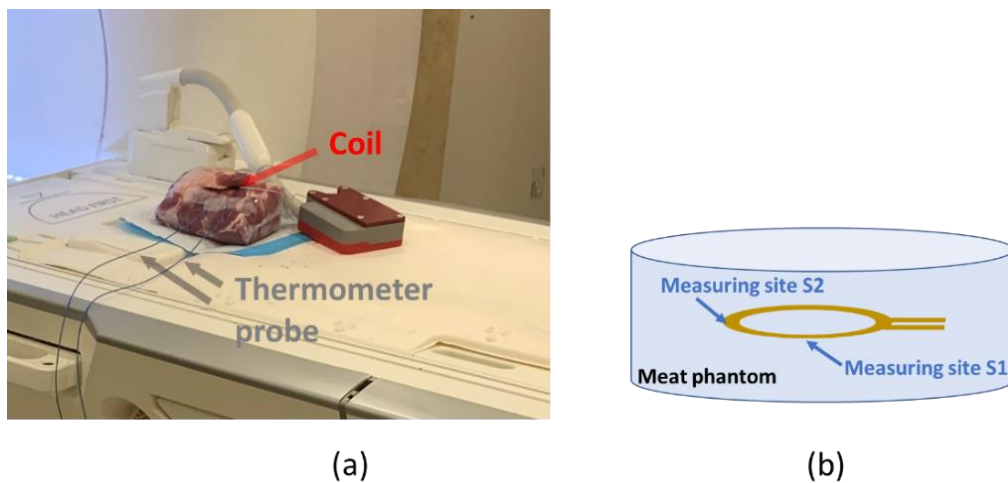
Figure 3.17: *Temperature measurements experimental setup. (a) The meat phantom on the MRI scanner. (b) The schematic illustration of the measuring sites.*

The measurements were performed with a benchtop fiber optic thermometer (FOTEMP1-

4, Optocon ®, resolution = 0.1°C). The probe was positioned at two different positions inside a

980 g meat phantom (Figure 3.17). One probe was placed right beneath the coil (measuring site

S1), and the other one was on the coil trace (measuring site S2). A continuous 15-minute fast low

angle shot three dimensional imaging (FL3D) sequence was performed on the meat phantom during the temperature measurement. The room temperature was kept at 20 °C.

The time-averaged RF power transmitted by the body coil during the FL3D sequence for our mini coil is 0.3 W. The body average Specific Absorption Rate (SAR) can be obtained by dividing the time-averaged RF power by the sample mass. Therefore, the experimental average SAR for the meat phantom was 0.31W/kg, which is well below the 1.6 W/kg limit by the Federal Communication Commission (FCC), 3.2 W/kg limit for the head in the MRI product safety standard IEC 60601-2-33, and the 3 W/kg limit in US Food and Drug Administration (FDA) regulation [4][106][107]. Figure 3.18(a) shows the temperature change during the 15-minute scan. No detectable temperature rise was found at both measurement sites.
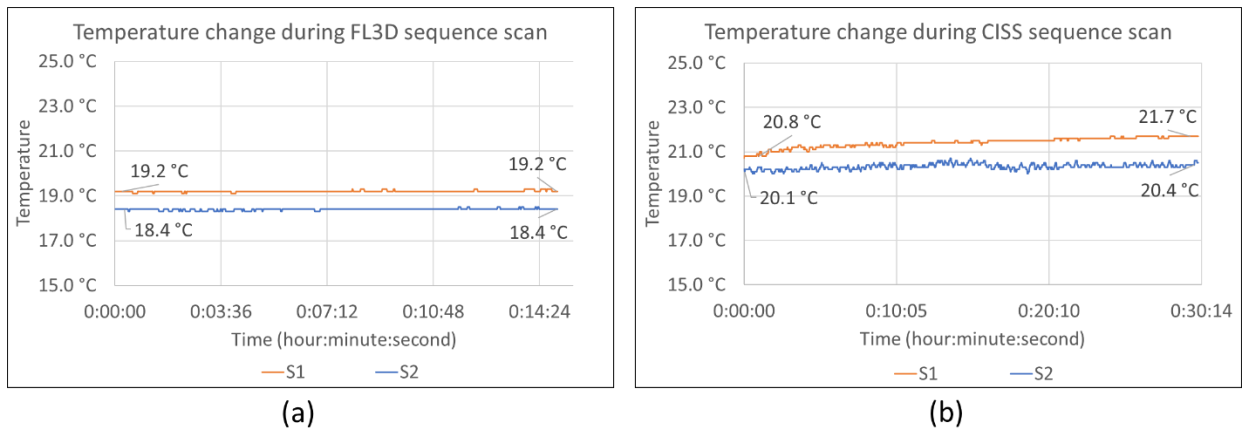
Figure 3.18: Temperature recordings at measuring sites S1 and S2 for (a) time-averaged RF power at 0.3 W for a 15-minute continuous FL3D sequence scan and (b) time-averaged RF power at 6.2 W for a 30-minute continuous CISS sequence scan. The maximum temperature increase is 0.9 °C over 30 minutes.

We then changed the sequence to a Constructive Interference in Steady State (CISS) 3D sequence with a time-averaged RF power of 6.2 W and continuously scanned for 30 minutes. This is not the usual sequence used for the mini coil, and it was only used to investigate the temperature change of the coil in a high-SAR sequence. The temperature increased from 20.8 °C to 21.7 °C at

52

site S1, with a maximum temperature rise of 0.9 °C (Figure 3.18(b)), which fell within the 1 °C

temperature increase limit of FDA regulation [108]. The temperature change at site S2 was

smaller, increasing from 20.1 °C to 20.4 °C. The temperature measurements demonstrated that the

mini coil is unlikely to cause thermal damage to the patient and should be safe to be used in the

clinical environment.

3.5. Discussion & conclusion

A flexible single-loop coil was designed for intra-operative imaging of the pituitary

gland. It achieved up to a 19-fold SNR improvement compared to a commercial head coil in the

agar phantom study. Even at a rotation angle of 60 degrees and an ROI depth of 16.5 mm, the

coil still produced a 2-fold relative increase in SNR. This study showed the feasibility of the

miniature coil for high-SNR MRI of pituitary microadenoma.

The increased SNR from the miniature coil makes it possible to use a higher resolution

imaging compared to the commercial head coil. The voxel size of the high-resolution sequence is

approximately 1/50th of the standard-resolution. Because the SNR is proportional to the voxel

size [109], our coil enabled a much-increased spatial resolution of that currently used with

standard 3T imaging. At this reduced voxel size, the commercial coil demonstrated an

inadequate SNR. To the contrary, our phantom study suggests that pituitary adenomas of 1 mm

and smaller may be detectable using our coil.

The electromagnetic behavior and performance of our custom coil were accurately

simulated in COMSOL Multiphysics. The simulation of the effective magnetic field matches

with the experimentally measured SNR across a clinically relevant range of coil angles and

distance, both in-plane pixel-wise and through-plane. The consistency of these two groups of

simulation data and experiment data validates both the numerical simulation model and SNR experiments. The difference between the mean SNR curve and the simulation curve is likely to be a result of the errors in the imaging plane alignment. The imaging planes were selected manually on the scanner, and any mismatches in distance or rotation angle can create shifts in the SNR curves.

Validated with the phantom scan experiment, this coil simulation model is important in studying the interaction between the fields from the surface coil and the ROI of the phantom. As demonstrated in the surgical placement example, the simulated coil field can be potentially used to predict the SNR improvement of using the miniature coil compared to a commercial head coil. It will also allow us to simulate the performance of other surface coil designs with different diameters, geometries, resonance frequencies, and placement configurations and therefore accelerate the development of improved coil designs for future phantom and cadaveric studies prior to clinical trials. Furthermore, we anticipate the simulation model will potentially enable selection of an optimal coil size and shape from a set of existing coil designs based on the specific anatomy of each patient.

An additional advantage of our design approach is that in theory the same relative multiplicative improvements in SNR would be achievable with higher field MRI scanners as they become clinically available. Prior research has qualitatively examined the image quality improvement for pituitary MRI with 7T scanners [47], [110]. Since a real-time tune and match is performed, the coil can be tuned to other resonance frequencies and is thus suitable for any MRI scanner.

Coils with a transverse B_1 field at the center of the coil are useful in solving the "dead spot" problem of the single loop coil found at large coil rotation angles. However, the main field of the

transverse-field coil is smaller than that of the single loop coil, leading to a lower mean effective transverse field within the ROI. At a small coil rotation angle or a large target depth, a single loop coil may be a better choice as it provides a higher mean SNR within the ROI. A quadrature coil that combines the single loop coil and a butterfly coil can be used to further improve the SNR. In theory, a quadrature coil can provide up to a $\sqrt{2}$-fold SNR improvement compared to the coil of the same geometry when used as a single coil [111], [112].

Based on the temperature measurement experiment, the temperature rises for both tested sequences were smaller than 1 °C. However, the temperature response of the patients to RF-related heating depends on multiple physiological conditions and MR parameters [113]. Specialty coatings and adhesives, such as Plasti Dip (Plasti Dip Int., Minneapolis, MN, USA), can be applied to make the coil heat insulated to prevent RF-induced heating when a sequence with high time-averaged RF power is used.

Chapter 4. Cadaver study

4.1. Cavity measurement

To find the optimal coil design that fits at least 95% of the patients, we measured the dimensions of the sphenoid distance with bony removal on retrospective patient images from 50 patients by an experienced neurosurgeon. The sphenoid distance is the maximum allowed dimension for the mini coil. An example of the measured sphenoid distance is shown in Figure 4.1. The distance was measured at 3 coil rotation angles: 0°, 20°, and 30°. Based on the mean SNR from the pituitary scan (Figure 3.8), within the 30° rotation angle, we can get a reasonably good coil performance with no "dead spot" in the ROI.
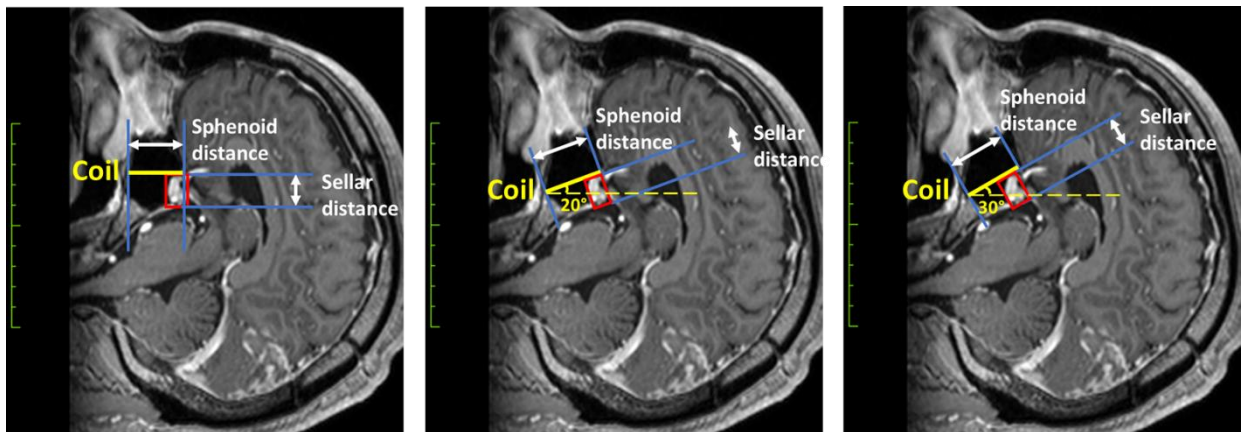
Figure 4.1: *The sphenoid distance and the sellar distance measured at (a) 0°, (b) 20°, and (c) 30° coil rotations. The pituitary gland is indicated in the red rectangular box. The yellow indicates the intended coil placement.*

The distributions of the measured sphenoid distance in the sagittal plane are presented in Figure 4.2 and Table 4.1. For the 0° rotation angle, the maximum sphenoid distance is 32.9 mm, and the minimum distance is 19.4 mm. To fit more than 95% of the patient, the coil diameter should be smaller than the 5th percentile of the sphenoid distance, which is 19.6 mm. The 5th percentile for 20° and 30° rotation angles were measured to be 22.1 mm and 21.9 mm, respectively. In general, as the rotation angle increases, the sphenoid distance that allows for the

coil placement increases. There is a tradeoff between the coil size and the coil SNR in the

sphenoid cavity. A large coil is preferred because it covers the pituitary in the region of high

sensitivity, and the high-sensitive region reaches the depth of the farthest point of the pituitary. A

large coil may fit in a tilted orientation inside the cavity. However, the tilted orientation may also

sacrifice the SNR of the coil as the SNR decreases with the rotation angle.
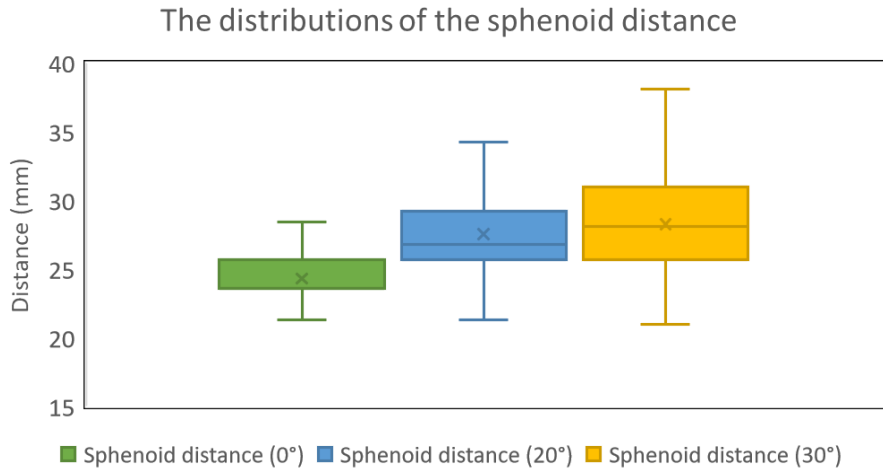
Figure 4.2: *The distributions of the measured sphenoid distance in the sagittal plane. The bottom line of the box represents the 1st quartile, and the top line of the box represents the 3rd quartile. The center line inside of the box indicates the median. For 0° rotation angle (green box), the 1st quartile and the median lines overlay. The whiskers (vertical lines) extend from the ends of the box to 1.5 times the interquartile range below the 1st quartile and above the 3rd quartile. The cross (×) represents the mean value.*

Table 4.1: *The values of the measured sphenoid distance in the sagittal plane.*

Measurement (mm)	0°	20°	30°
Minimum	19.356	20.0012	20.969
5th percentile	19.61408	22.06584	21.9368
25th percentile	23.5498	25.808	25.808
Median	23.5498	26.7758	28.0662
75th percentile	25.4854	29.034	30.9696
95th percentile	29.74372	33.873	33.29232
Maximum	32.9052	35.1634	38.0668

We are also interested in measuring the maximum target depth for the coil, which is the sellar distance, as shown in Figure 4.1. The distributions of the measurement are shown in Figure 4.3 and Table 4.2. The sellar distance ranges from 9 mm to 14.5 mm, 5.8 mm to 14.8 mm, and 8.7 mm to 14.5 mm for 0°, 20°, and 30°. Based on the MoM Full-Wave simulation for the optimum coil radius including coil losses in [25], the optimal coil radius for a target depth from 10 mm to 20 mm at 3 T MRI should be between 7.8 mm and 13.7 mm.
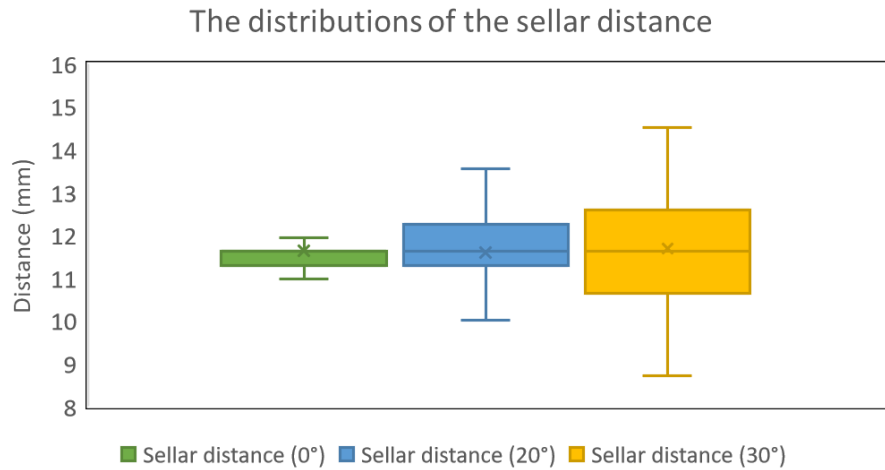
Figure 4.3: *The distributions of the measured sellar distance in the sagittal plane. For 0° rotation angle (green box), the 3rd quartile and the median lines overlay.*

Table 4.2: *The values of the measured sellar distance in the sagittal plane.*

Measurement (mm)	0°	20°	30°
Minimum	9.0328	5.8068	8.7102
5th percentile	10.12964	9.678	10.0006
25th percentile	11.291	11.291	10.6458
Median	11.6136	11.6136	11.6136
75th percentile	11.6136	12.2588	12.5814
95th percentile	13.2266	13.5492	13.2266
Maximum	14.517	14.8396	14.517

The maximum lateral intercarotid distance (as shown in Figure 4.4) is the maximum space available for the coil in the coronal plane. The minimum intercarotid distance measured in

the 50 patients was 23.2 mm, while the maximum distance was 37.7 mm. This distance is larger than the sphenoid distance in the sagittal plane and thus imposes less constraint on the coil dimension.
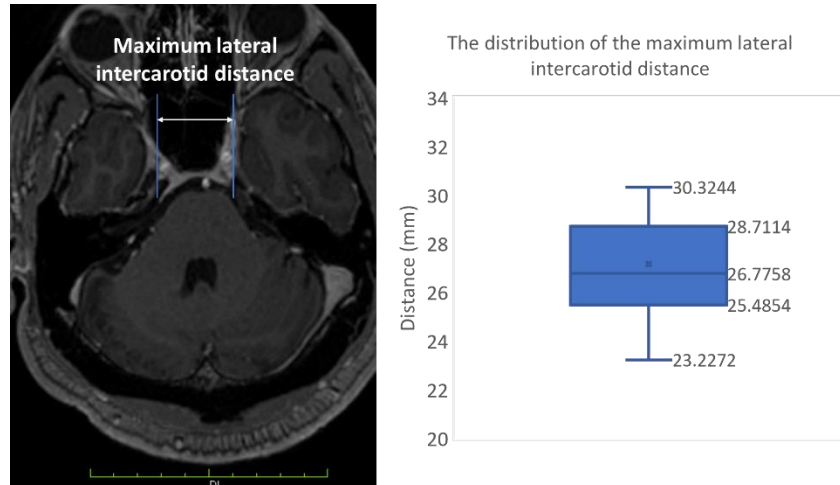
Figure 4.4*: The illustration of the maximum lateral intercarotid distance in the coronal plane and the distribution.*

Based on the measured sphenoid distance, sellar distance, and intercarotid distance, we designed a single loop coil with a 20-mm diameter for clinical use. The coil should fit more than 95% of the patients with a rotation angle smaller than 30°, providing sufficient coverage for the entire pituitary gland.

4.2. Cadaver head MRI scan with mini coil

4.2.1. Cadaver specimens

Two human cadaver heads were used for MRI imaging with a 3T MRI scanner (Prisma, Siemens Healthcare). The heads were frozen and brought to room temperature one day before the scanning. For preparation, the specimens underwent a transsphenoidal endoscopic approach to place the coil endonasally. The mini coil was inserted through the nostril and secured at the pituitary gland using a saline-soaked Helostat sponge. The intended coil placement method

inside the sphenoidal cavity is shown in Figure 4.5.
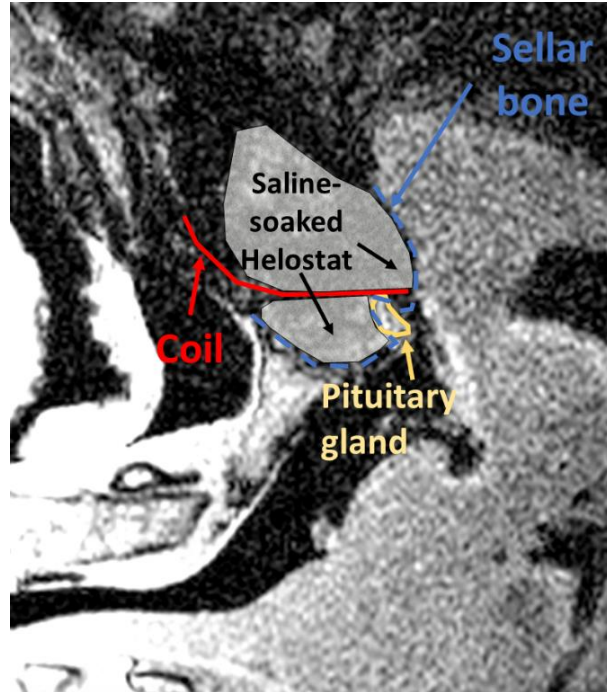
Figure 4.5: *An illustration of the coil position (red line). Saline-soaked Helostat was used to secure the coil above and beneath the coil. The pituitary gland is circled in the yellow line.*

4.2.2. Mini coil preparation

The coil and circuit box interface were the same as in the phantom study. The 20-mm diameter coil (2-mm wide trace, 17.8 μm thick) was built on a Flexible PCB and connected to the circuit box with a 20-cm coaxial cable. The circuit box was kept outside of the cadaver head for tuning and matching. It was also used for active decoupling during the body coil transmit mode. The circuit box was inserted into the pre-amplifier that connected to the MRI scanner. For waterproofing, the coil was coated with 3 layers of Plasti Dip coating (Plasti Dip Int., Minneapolis, MN, USA). The coil was placed as parallel as possible to the MRI scanner bed during the surgical placement (Figure 4.5). As mentioned previously, the MRI signal decreases as the coil rotation angle increases while the maximum SNR is achieved at 0 ° rotation angle or when the coil plane is parallel to the scanner bed.

After the surgical placement of the coil, a custom tune and match was performed to ensure the coil performance. A comparison of the measured S11 with various loading conditions after tune and match is shown in Figure 4.6. The measured S11 values were all below – 30 dB and the coil was tuned to the resonance frequency at 123.2 MHz ± 0.1 MHz. The impedance was matched to the desired value with an error of less than 3%. Q_{ratio} of the various loading conditions are listed in Table 4.3. For a 20-mm coil, the Q_{ratio} was slightly smaller than that of a 26-mm coil. We demonstrated that the tune and match circuit box for the mini coil has a sufficient tuning and matching range, and the coil can be used under different environments.
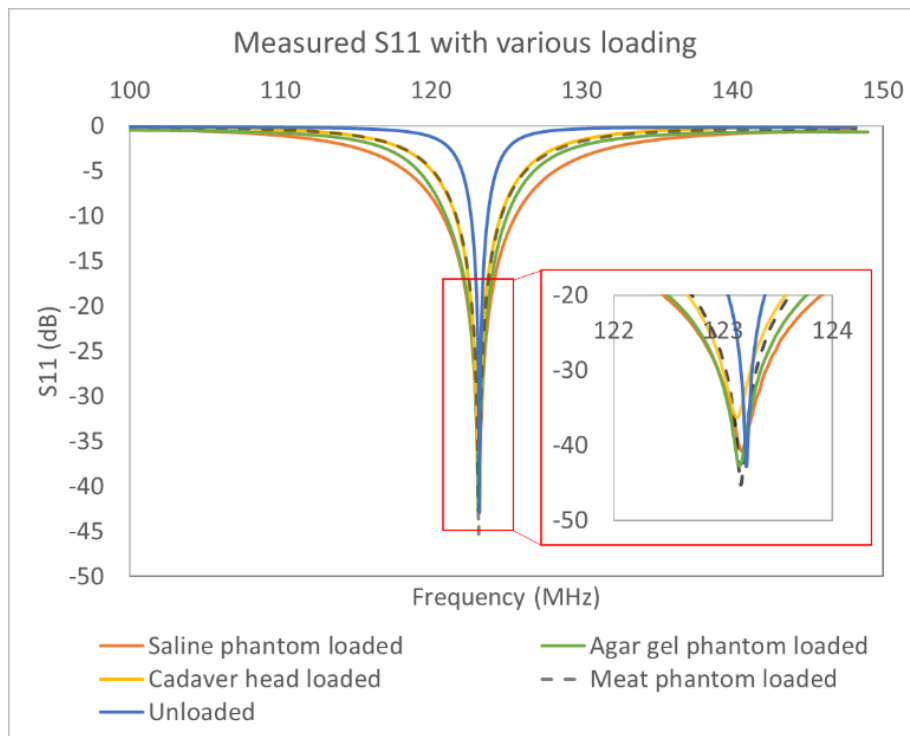
Figure 4.6: *A comparison of the measured S11 with various loading conditions.*

Table 4.3: *The loaded Q factors and Q ratios for various loading conditions.*

	Q_{loaded}	Q_{ratio}
Saline phantom (26 mm coil)	$\dfrac{123.2\ MHz}{130.8\ MHz - 116.1\ MHz} = 8.4$	4.3
Agar gel phantom (26 mm coil)	$\dfrac{123.2\ MHz}{128.6\ MHz - 117.6\ MHz} = 11.2$	3.2
Cadaver head (20 mm coil)	$\dfrac{123.1\ MHz}{127.6\ MHz - 118.6\ MHz} = 13.7$	2.6
Meat phantom (20 mm coil)	$\dfrac{123.2\ MHz}{127.9\ MHz - 118.7\ MHz} = 13.4$	2.7

4.2.3. Feasibility of the mini coil

The mini coil was specifically designed to provide high-resolution MR imaging of the pituitary gland and the surrounding structure. The mini coil included a real-time tune and match circuit box to ensure the coil's performance under various environmental conditions. Saline-soaked Helostat sponge was used to secure the coil at its optimal location during the scanning (Figure 4.7 (a) (b)). The flexible coil can be easily folded through the nostril and placed close to the pituitary gland. The coil was coated with Plasti Dip coating for waterproofing and thermal insulation (Figure 4.7 (c)). In this feasibility study, we demonstrated that the mini coil could be surgically placed through the transsphenoidal endoscopic approach and tuned and matched inside the cadaver head, improving the SNR of the pituitary gland MR imaging.
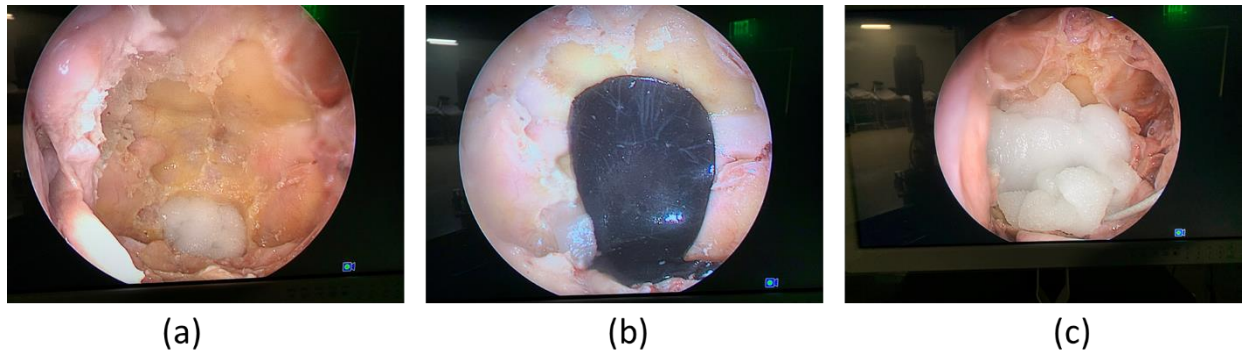
Figure 4.7: *(a) Picture of the Helostat placed below the coil. (b) The picture of the coil inside the sphenoid cavity (waterproofed with Plasti Dip). (c) Picture of the Helostat placed above the coil.*

4.2.4. Pituitary gland imaging

Scan parameters

The T1-MPRAGE sequence images in both the sagittal and coronal planes were obtained with the commercial Siemens 20-channel HeadNeck coil and our mini-coil. The T1-MPRAGE pulse sequence is commonly used in brain MR imaging, which offers a good visualization of the lesions in the cord [114], [115]. For the head coil, phase oversampling was enabled to avoid phase wrapping artifacts due to the small Field of View (FoV). Phase oversampling was unnecessary in the mini coil since it had a localized signal. Therefore, a smaller FoV could be used for the mini coil. For the 0.9 mm $\times$ 0.9 mm $\times$ 0.9 mm resolution image, the mini coil used a FoV of 55 mm $\times$ 55 mm $\times$ 55 mm and an acquisition matrix size of 64 mm $\times$ 64 mm $\times$ 64 mm. The head coil had a FOV of 240 mm $\times$ 240 mm $\times$ 240 mm and an acquisition matrix size of 256 mm $\times$ 256 mm $\times$ 256 mm. The FoV of the mini coil was reduced by a factor of 4, which resulted in a much shorter scan time while maintaining the same in-plane resolution. No degradation in the image quality was observed on the mini coil sequence.

T1-MPRAGE sequence was also used for the image with a resolution of 0.4 mm $\times$ 0.4 mm $\times$ 0.4 mm. The scan parameters for all the sequences are listed in Table 4.4 for the

commercial head coil and Table 4.5 for the mini coil. SD PD-TSE sequence with the same resolution used in the phantom study was performed and repeated for 3 times for SNR evaluation. The body coil was used as the transmit coil in the cadaver head scans.

Table 4.4: *The parameters for the T1-MPRAGE sequence and standard resolution PD-TSE sequence used on the commercial head coil.*

	T1_MPRAGE isotropic	T1_MPRAGE isotropic	PD_TSE
Resolution (mm³)	$0.9 \times 0.9 \times 0.9$	$0.4 \times 0.4 \times 0.4$	$0.7 \times 0.7 \times 3$
Echo time (ms)	2.32	3.09	9.1
Repetition time (ms)	2300	2300	3000
Acquisition matrix size	$256 \times 256 \times 256$	$256 \times 256 \times 256$	$320 \times 320 \times 15$
Field of View (mm³)	$240 \times 240 \times 240$	$100 \times 100 \times 100$	$220 \times 220 \times 45$
Scan time (mm:ss)	09:48	14:43	03:11
Phase oversampling	0%	50%	0%

Table 4.5: *The parameters for the T1-MPRAGE sequence and standard resolution PD-TSE sequence used on the mini coil.*

	T1_MPRAGE isotropic	T1_MPRAGE isotropic	PD_TSE
Resolution (mm³)	$0.9 \times 0.9 \times 0.9$	$0.4 \times 0.4 \times 0.4$	$0.7 \times 0.7 \times 3$
Echo time (ms)	2.32	3.09	9.1
Repetition time (ms)	2300	2300	3000
Acquisition matrix size	$64 \times 64 \times 64$	$256 \times 256 \times 256$	$320 \times 320 \times 15$
Field of View (mm³)	$55 \times 55 \times 55$	$100 \times 100 \times 100$	$220 \times 220 \times 45$
Scan time (mm:ss)	02:25	09:48	03:11
Phase oversampling	0%	0%	0%

MR image

The T1-MPRAGE images from the commercial Siemens 20-channel HeadNeck coil were compared with the images from the mini coil. Due to the low resolution, the structure of the pituitary gland can not be clearly identified on the images with 0.9 mm × 0.9 mm × 0.9 mm resolution. With the same in-plane resolution, no visible degradation of image quality was found on the images (Figure 4.8 (a)&(c), Figure 4.9 (a)&(c)), while the scan time was reduced by a factor of 4.

Figure 4.8: Comparative T1-MPRAGE images of the pituitary gland of a cadaver head obtained using the 20-channel coil (left columns a & b) and mini coil (right columns c & d) in the coronal plane. The resolution is 0.9 mm × 0.9 mm × 0.9 mm (top rows a & c) and 0.4 mm × 0.4 mm × 0.4 mm (bottom rows b & d).
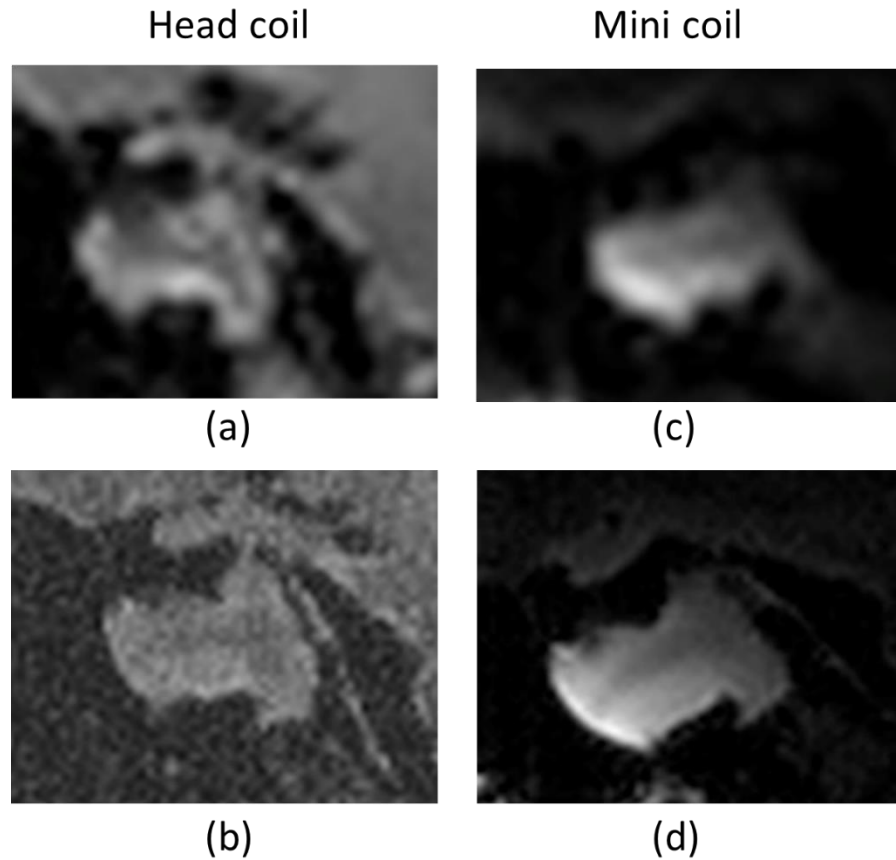
Figure 4.9: Comparative T1-MPRAGE images of the pituitary gland of a cadaver head obtained using the 20-channel coil (left columns a & b) and mini coil (right columns c & d) in the sagittal plane. The resolution is 0.9 mm × 0.9 mm × 0.9 mm (top rows a & c) and 0.4 mm × 0.4 mm × 0.4 mm (bottom rows b & d).

As shown in Figure 4.8 and Figure 4.9, remarkable SNR improvement within the pituitary gland was obtained using the mini coil. The image quality of the high-resolution images (resolution = 0.4 mm × 0.4 mm × 0.4 mm) from the mini coil was superior to those using the commercial head coil. The detail of the internal structure of the gland was no longer obscured by large speckling noise.

The images from the PD-TSE are shown in Figure 4.10. The mini coil image shows a brighter signal within the pituitary gland and a lower background noise than the head coil image. The pixel SNR was calculated based on the images (Figure 4.11). The maximum SNR of the

mini coil was found to be 2140, with a mean SNR within the pituitary gland to be 677. The mean

SNR of the head coil was calculated to be 130 and was uniform across the pituitary gland. A

maximum of a factor of 16 SNR improvement was obtained by the mini coil compared to the 20-

channel commercial head coil, and the mean SNR within the ROI was improved by a factor of 5,

enabling high-SNR pituitary MRI in the pre-clinical environment.
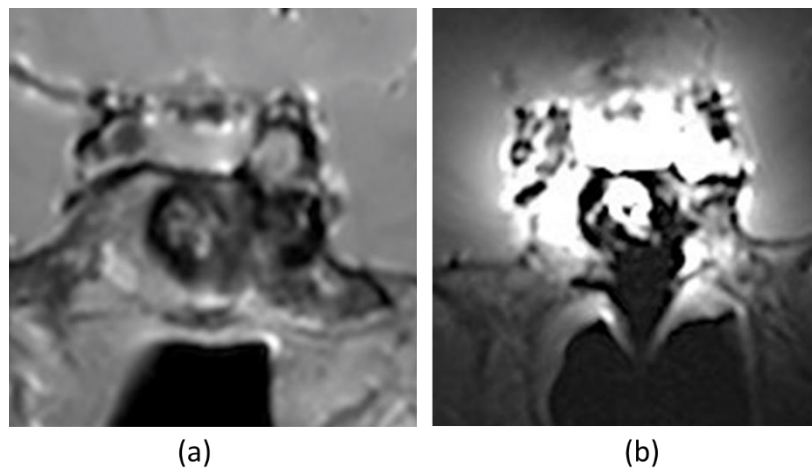
Figure 4.10: Comparative PD-TSE images of the pituitary gland of a cadaver head obtained using the (a) 20-channel coil and (b) the mini coil in the coronal plane. The resolution is 0.7 mm × 0.7 mm × 3 mm.
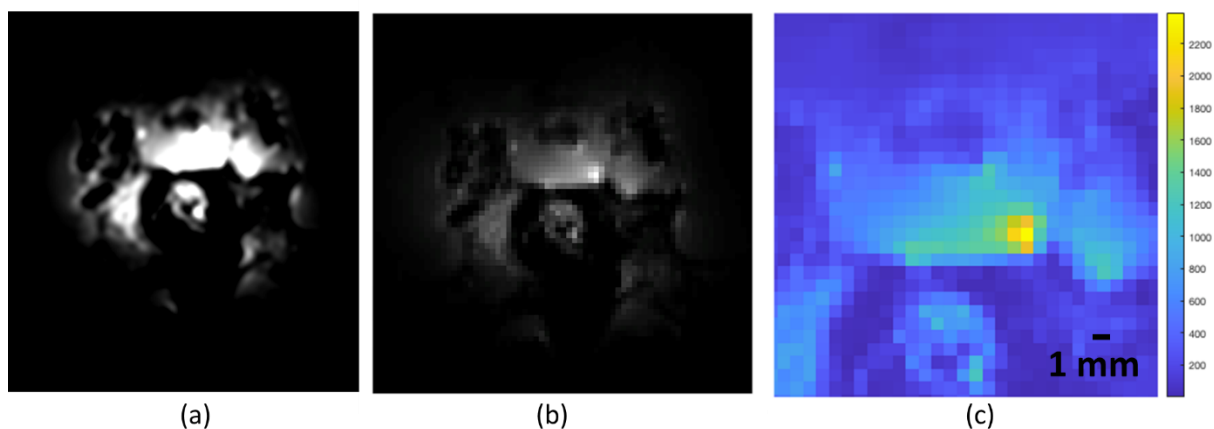
Figure 4.11: MATLAB post-processing on the PD-TSE image. (a) The image filter imposed by the MRI scanner was removed from the image. (b)&(c) Pixel SNR were calculated. The size of the pixel is 0.7 mm × 0.7 mm. The color legend indicates the SNR value.

4.3. Conclusion

  The feasibility of using the miniature flexible coil for high-SNR pituitary MR imaging in the pre-clinical environment has been demonstrated. The mini coil design was waterproofed before the experiment and tuned and matched after the surgical placement inside the cadaver heads. The coil can provide a maximum of 16-fold SNR improvement compared to a 20-channel commercial head coil. The mean SNR within the pituitary gland was improved by approximately 5-fold with the mini coil. The miniature flexible coil has great potential to improve the detection and characterization of pituitary microadenomas.

Chapter 5. Future work

A novel miniature flexible surface coil positioned millimeters from the pituitary gland was developed for high-resolution pituitary MRI. To further improve the microadenomas identification of the work, three major advances in the areas of coil development, motion correction techniques, and surgical protocol could be considered.

Coil development

A more robust and reliable connection between the coil and the coaxial cable could be used. For example, a low-profile UF.L connector could be attached at a variety of angles on the coil to allow for easier coil placement in the sphenoid sinus (Figure 5.1). To enhance the soldering strength of the connector on the FPCB, we could add a thin stiffener could at the back of the coil.

The biocompatibility of the coil is another concern. A biocompatible Parylene C could be deposited on the coil through a microfabrication process. Parylene C is a conformal coating, which has attained ISO 10993 status and has been used on various implantable flexible devices [116], [117]. Additionally, sterilization of the device before in vivo use needs to be addressed. Several methods for sterilizing Parylene devices have been developed in literature [118]–[120]. For example, hydrogen peroxide plasma could be used to sterilize Parylene-based electrochemical sensors with no changes in device and electrode properties after the treatment [121].
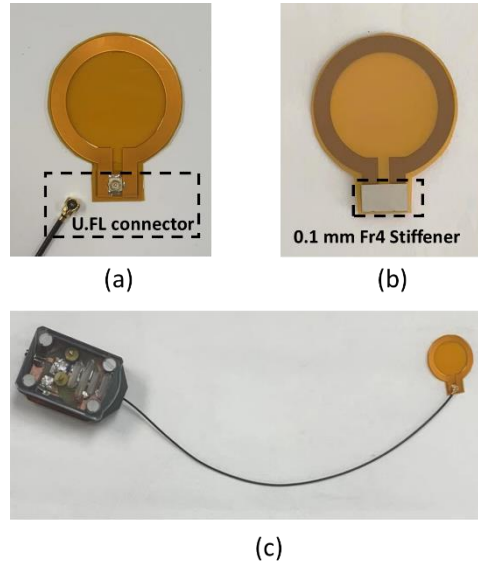
Figure 5.1: *A new version of the coil with a UF.L connector. The coil is built on a FPCB. (a) The front of the coil. (b) The back of the coil. (c) The coil is connected to the coaxial cable and the tune and match circuit box.*

Motion correction techniques

In addition to limited SNR, motion-related image degradation is also one of the major factors limiting high-resolution pituitary MR imaging [54]. These motions involve breathing motion as well as cardiovascular-induced head motion, which is caused by the transmission of the arterial pulse. The motions have a sub-millimeter displacement range and may affect the detection of millimeter-sized pituitary microadenomas. Tracking coils could be integrated with the mini coil to address the physiologic motion-related image degradation issue (Figure 5.2). The tracking coils could be composed of electromagnets and microcylinders filled with MRI contrast agents. The location of the tracking coils could be firstly determined and the displacement along the motion direction will be calculated at each cardiac phase. The motion parameters could then be used to adjust the imaging parameters in real time and correct the motion artifacts. Moreover, the technique could also prove helpful information about the coil position in vivo to ensure optimal placement of the coil during the scanning.
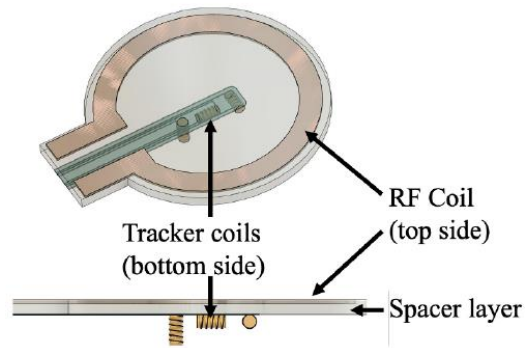
Figure 5.2: *Integration of a 2-cm diameter coil with tracking coils (top). The miniature coil is on the front side, while tracker coils are on the back side, with spacing between them determined by a PDMS spacer layer. Side view of the coil (bottom). Three tracker coils are shown for demonstration.*

Surgical protocol

A more systematic surgical procedure to place the coil and secure the coil at its optimal position could be developed. The key is to position the coil parallel to the floor (perpendicular to the B_0 field) and minimize the offset between the center of the coil and the center of the pituitary gland. In the preliminary clinical experiment, we found that the coils might be shifted during the transportation to the MRI room after the placement in the operation room. To ensure the coil performance, technique could be developed to secure the coil to prevent accidental dislodgement.

Various materials could be investigated as the support for the coil. Using saline-soaked Helostat is convenient. However, the sponge might also show a high-intensity signal on the MR images, which could be misleading when identifying the target structure. For example, the Helostat could be replaced by an inflated balloon to secure the coil (Figure 5.3).
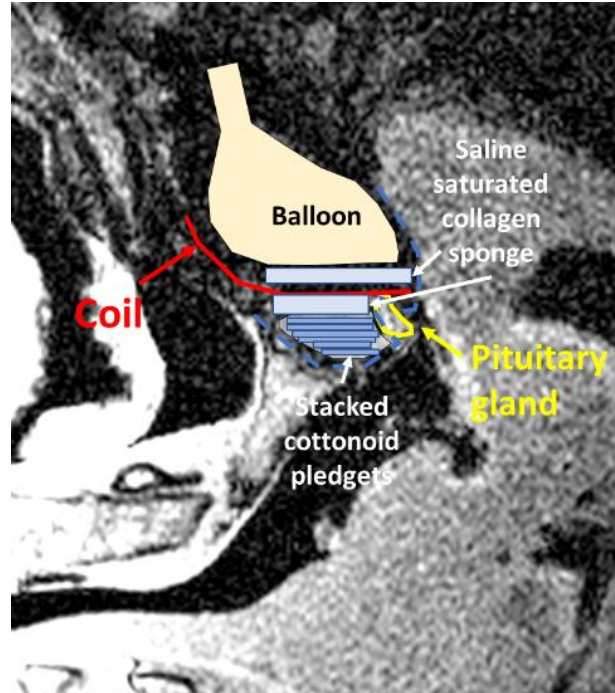
***Figure* 5.3**: *Possible coil positioning method. The sinus could be filled with layered materials to support the coil. An inflated balloon could be used to secure the coil.*

Magnetic Shielding for a Single Chip on Multi-chip-module

Chapter 6. Introduction and Motivation

6.1. Magnetic shielding

The Digital Revolution in the mid-20th century brought society into a brand-new era, marking the beginning of the information age. Since then, electronic devices and communication technology have been employed in every area of life. For communications, the trend has been heavily transitioning from wired information transfer to wireless information transfer. Wireless information transfer involves the use of electromagnetic waves in free space and is a fast and easy way for sensing and information transfer. For sensing, the Ultra-Wideband (UWB) short-range radar has been used for monitoring human vital activities and for geometrical structure recognition of an unknown environment [122]. For information transfer, radio waves are commonly used in mobile communication and surveillance technologies [123], [124]. However, as more electromagnetic waves penetrate life and create a complicated electromagnetic environment, electromagnetic radiation pollution becomes a surging issue [125], [126]. Exposure to electromagnetic waves not only has a possible severe effect on human health but also affects the functionality of sensitive electronic equipment such as atomic clocks, transmission cables, and microprocessor-controlled devices [127]–[129]. Electromagnetic interference shielding is essential to alleviate this influence from electromagnetic waves.

There are three kinds of electromagnetic interference shielding: electric field shielding, magnetic field shielding, and electromagnetic shielding [130]. Electrical field shielding usually uses grounded metal to keep the external electric field from the target area. The surface charge on the metal shell is redistributed to cancel out the external electric field inside the shield. Magnetic field shielding can be distinguished into two categories: passive shielding and active shielding. The principle of magnetic shielding is discussed in detail in the following paragraph.

Electromagnetic shielding combines electric shielding and magnetic shielding by using conductors and magnetic materials to weaken both fields simultaneously. All these shielding methods are realized by changing or transferring the propagation path of the electromagnetic energy [131].

Magnetic shielding plays a significant role in a wide range of scientific fields. A stable and low-noise magnetic field environment is essential for sensitive devices like electron microscopy and experiments conducted on ultracold atoms, quantum simulations, and precision measurements [132]–[135]. Active shielding is often used for high-frequency magnetic field shielding. The induced current in the good conductors generates a magnetic field that opposes the magnetic field outside the shield, which protects the volume inside the shield from magnetic field interference. On the other hand, passive magnetic shielding is usually used for low-frequency magnetic fields. A passive magnetic shield is often structured as a multi-layer shield composed of ferromagnetic materials with high magnetic permeability, such as permalloy and Mu-metal [136]. With higher magnetic permeability, the material has lower magnetic reluctance and thus transmits the magnetic field through the material more easily [130]. By attracting and focusing the magnetic field lines in the shielding material, the magnetic shield prevents the field from entering or spreading in the protected area. One application for passive magnetic shielding is to shield the DC magnetic fields for superconducting electronic (SCE) devices. The following section is dedicated to the introduction to the superconducting multi-chip module (MCM) and the potential of using a compact multi-layer magnetic shield on a single SCE chip that can be integrated with the MCM.

6.2. Superconducting multi-chip-module

Superconducting devices, or Josephson junctions, are widely used in many technological applications. They demonstrate the "ultimate" performance by providing the lowest power dissipation, high switching, counting or computation speed, low attenuation, and low-dispersion transmission lines [137]. For example, the rapid single flux quantum (RSFQ) is a digital electronic device that takes advantage of superconductivity for digital signals processing [138]. RSFQ logic system stores the information in the form of single magnetic flux quanta and transfers the information in the form of single voltage pulses of the area [139]. RSFQ electronics have been utilized in ultra-fast, low-noise, and low-power consumption analog-to-digital converters (ADC) that outperform all other sigma-delta A/D converters [140].

In the fabrication process of the Josephson junctions, the defect rate is about one defect junction per 10,000, causing the current limitation in the circuit complexity [141]. To overcome this defect density issue and the problems with bias currents larger than a few amperes, multi-chip module (MCM) technique was introduced. In 2008, Kameda et al. successfully developed a 4x4 SFQ network switch using MCM packaging for superconducting electronics [142]. The switch fabric and switch scheduler were attached to an MCM carrier that enabled a hybrid critical current density technology. In this way, the critical current density was increased for the driver chip to improve the speed while maintaining wide bias margins.

However, relying heavily on single-flux-quantum digital control, the SFQ chip is required to be operated in a clean magnetic field environment. Electromagnetic fields, especially magnetic fields and flux vortices, can go through the superconducting films and devices. DC field biasing, electromagnetic interference or even motion in Earth's magnetic field caused by equipment vibrations may bring parameter changes, noises, or loss of flux lock in SQUID magnetometers

[143]. These undesirable effects affect the performance of the devices and are usually prevented or minimized by using magnetic shielding. Shielding for a large superconducting system is available. For example, magnetically shielded rooms for non–zero electric dipole moment (EDM) experiment have been demonstrated to shield the experiment from external magnetic disturbances [144]. Shielding is also used on qubits to study internal quality factors for resonators intended for quantum coherent circuits [145].

6.3. Motivation for the magnetic shielding for SCE

The development of SCE device integration has led to the need to protect physically larger areas from DC magnetic fields. The technique of adding an additional shielding plane on top of the RSFQ circuits has been studied, and the benefit of local magnetic shielding has been proven [146], [147]. This approach surrounds a circuit by one or several superconducting niobium loops on the same layers of the SFQ circuit [148]. However, the local magnetic field is reduced by only a factor of 4 in the best scenario, which may not be sufficient. Also, the shielding needs to be fabricated together with the chip, constraining the design of the chip and being less flexible on shielding modification. Another approach is to place all superconducting circuits inside a single shield. For example, 3D shields are designed to create shielding systems with low residual magnetic field for a Superconductor Quantum Interference Filter (SQIF) based magnetic sensor [149]. The design uses 3 separate shields with magnetizing coils for $x, y,$ and z direction fields, which is bulky and may not be suitable for MCMs with multiple chips as it doesn't account for chip-to-chip coupling. Multilayer magnetic shielding has been designed for superconducting circuit chips, providing a less than 50 nT magnetic field environment with shielding effectiveness higher than 60 dB [150]. The work demonstrates that the multi-layer

magnetic shielding is an effective shielding method for the SCE chip. However, the multilayer

shield is larger than 100 mm, with a 1 mm thickness for each layer and 3 mm gap between the

layers, which is good for the entire chip shielding but not useful for the single chip shielding on

the MCM.

To solve the problem of integrating shields with MCMs, we proposed a novel way to

isolate SCE chips from each other and the external environment. This approach uses separated

magnetic shields on each SCE chip to reduce the chip-to-chip coupling effect of the circuits or

signal currents influence from local magnetic fields. The shields consist of high permeability

material that redirects the magnetic flux lines to protect the enclosed devices. The microscale

multi-layer shields provide high-efficiency shielding around arbitrary shapes and enable the

fabrication of chip-scale shielding [128]. Additionally, magnetic through silicon vias (mTSVs)

are developed to help achieve the desired level of magnetic shielding. We expect to improve the

magnetic shielding to potentially decrease the noise floor and increase the device stability and

circuit margins in SCE devices. In this dissertation, we mainly focus on the design and

fabrication of the proposed magnetic shielding, and shield characterization is discussed in future

work.
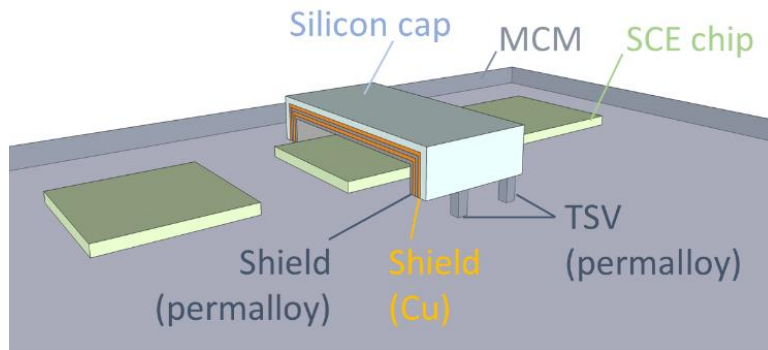
Figure 6.1: Cutaway illustration of proposed magnetic shielding. The shield encapsulates the entire SCE chip and is integrated into the MCM.

Chapter 7. FEA Modeling of Permalloy-Plated Magnetic Shielding

Materials with high permeability are commonly used as magnetic shielding against the external magnetic field. The magnetic shielding needs to be properly designed with the optimum parameters to ensure the effectiveness of the shielding. There are different approaches to solving the shielding problem analytically. The field can be theoretically determined by considering the induced eddy currents [151]. However, an approximation of the mutual inductance between the coil and the image coil has to be made in this method, which limits the solution to 10% accuracy. The shielding problem can be analyzed by solving the differential equation of the magnetic vector potential [152][153]:

$$\nabla^2 \vec{A} + k_0{}^2 \vec{A} = 0 \qquad\qquad (7.1)$$

where $k_0{}^2 = \mu_0 \varepsilon_0 \omega^2$. Equation (2.1) is difficult to solve, and evaluation must be done by numerical integration on a computer, requiring great skill in programming to keep the calculation within the upper and lower limits of the machine [154]. Both these methods can only be applied in limited cases where the system coordinate fits the natural coordinate system. The third method is the application of the transmission theory of shielding by Schelkunoff [155]. Although approximations are also made in this method, it is still one of the most useful analytical methods in shielding effectiveness and proved to be applicable to normal incidence waves on an infinite metal plane [154]. These analytical methods provide good results for the shielding effectiveness at high frequencies. For low frequency magnetic shielding problems, a numerical solution is usually necessary [153].

7.1. Finite element method

Finite Element Analysis (FEA) was performed using COMSOL Multiphysics® [74] to

study the shielding performance of the magnetic shielding designs. Since the shielding problem

is related to the interaction between the material and the electromagnetic waves, Maxwell's

equations are solved and coupled to other physics in the COMSOL Multiphysics® AC/DC

module:

$$\nabla \times \mathbf{H} = \mathbf{J} + \frac{\partial \mathbf{D}}{\partial t} \qquad (7.2a)$$

$$\nabla \times \mathbf{E} = -\frac{\partial \mathbf{B}}{\partial t} \qquad (7.2b)$$

$$\nabla \cdot \mathbf{D} = \rho \qquad (7.2c)$$

$$\nabla \cdot \mathbf{B} = 0 \qquad (7.2d)$$

where **H** is the magnetic field intensity; **J** is the current; **D** is the electric displacement field; **E** is

the electric field; **B** is the magnetic flux density; and ρ is the electric charge density.

In COMSOL Multiphysics®, a set of boundary conditions and material constitutive

relations are needed to relate the **E** to the **D** field, the **J** to the **E** field, and the **B** to the **H** field

[156]. To model the magnetic material with high permeability, we chose the Magnetic Field

physics. The model was set up to solve the reduced field H_{red}, and the total magnetic field in the

model is the sum of the background magnetic field H_0 and the reduced field. With no current

flowing in the model, Maxwell's equations can be simplified by solving the magnetic scalar

potential V_m:

$$\nabla \cdot (-\mu \nabla V_m) = 0 \qquad (7.3)$$

where μ is the permeability. The Zero Magnetic Scalar Potential condition needs to be specified

for at least one point in the model.

When a steady-state current flows in the model, the magnetic vector potential **A** is solved:

$$\nabla \times (\mu^{-1} \nabla \times \mathbf{A}) = \mathbf{J} \qquad (7.4)$$

Then, the magnetic vector potential is used to solve the magnetic field flux density by:

$$\boldsymbol{B} = \nabla \times \boldsymbol{A} \qquad\qquad (7.5)$$

In the frequency domain, instead of equation 2.4, we are now solving:

$$\nabla \times (\mu^{-1} \nabla \times \boldsymbol{A}) = -\sigma \frac{\partial \boldsymbol{A}}{\partial t} \qquad (7.6)$$

where σ is the conductivity and $\boldsymbol{E} = -\frac{\partial \boldsymbol{A}}{\partial t}$. This equation considers the conduction currents and

induced currents and is used for material nonlinearities like the B-H nonlinear material [156].

7.2. 2D shield simulation

The aim of the simulations was to determine the internal magnetic flux density of the

shield and to optimize the shield designs, which can ensure an internal magnetic flux density

lower than 4 µT. The modeling simulated the internal magnetic field of the shield under an

external field of 50 µT (Earth's magnetic field).

Though a full 3D simulation is more accurate in shielding performance characterization,

the runtime is usually long, and the model sometimes has difficulty converging. With a film

thickness of several tens of micrometers, the shield layers need a micrometer-scale mesh size,

which also increases the memory needed for solving the model. Additionally, using nonlinear

magnetization curves in the material properties worsens the simulation time and convergence

problems. Therefore, we simplified the simulation to a 2D model to reduce the simulation load.

Figure 7.1(a) displays a cross-section of the simulated shield geometry for a single SCE

chip. The shield dimension was set to 10 mm in length and 3 mm in height to ensure a full

enclosure of the chip. The 3-layer magnetic shield was composed of two 100 µm thick permalloy

layers plated onto either side of the 100 µm thick copper (Cu) layer. The shield was attached to a

500 µm thick silicon (Si) substrate, which was chosen for simulation purposes and can be varied

to match other substrates of interest. A 50 µT external magnetic field was applied for all

simulations (Figure 7.1(b)). In the 2D simulation, nonlinear magnetization curves (BH curves) for the permalloy measured in [157] were assigned to the permalloy material properties. As shown in Figure 7.1(c), the minimum magnetic flux density at the surface of the MCM is 40.8 µT, which is much higher than the 4 µT requirement for the internal field. The effectiveness of shielding can be characterized by the shielding factor, which is defined as the ratio between the external magnetic field and the magnetic field inside the shielding:

$$S = \frac{H_{ext}}{H_{in}} \qquad (2.7)$$

This cap design has very limited shielding effectiveness, with a shielding factor $S = 1.23$. An improved shield design is necessary.
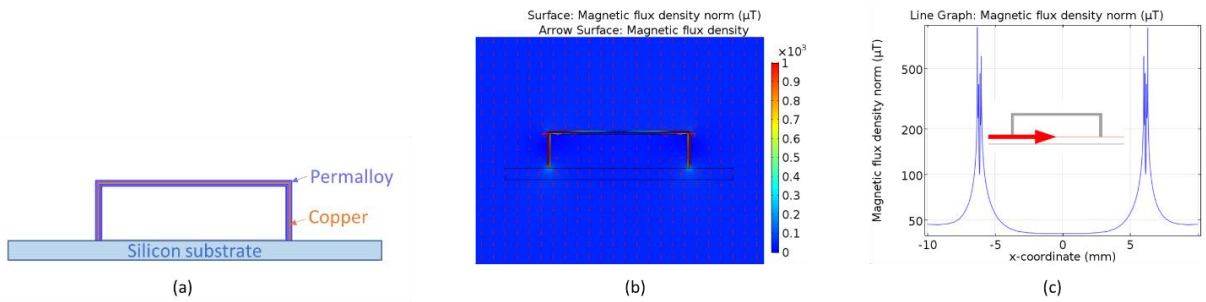
Figure 7.1: *2D cap shield model. a: The top shield cap consisted of 3 layers: permalloy, Cu, and permalloy. The cap was placed on the MCM substrate (500 µm). b: Simulated magnetic flux density for the cap shield model. Magnetic flux density was attracted to the magnetic material. c: The magnetic flux density along the surface of the MCM (the red line).*

To enhance the shielding effectiveness, an additional 100 µm thick permalloy layer was added to the bottom of the Si substrate (Figure 7.2(a)). The shield cap design stayed the same as before. In this way, the magnetic flux can also be shielded from the bottom of the MCM. The minimum simulated magnetic flux density inside the shield on the MCM is 27.3 µT, and the shielding factor increases to $S = 1.83$.
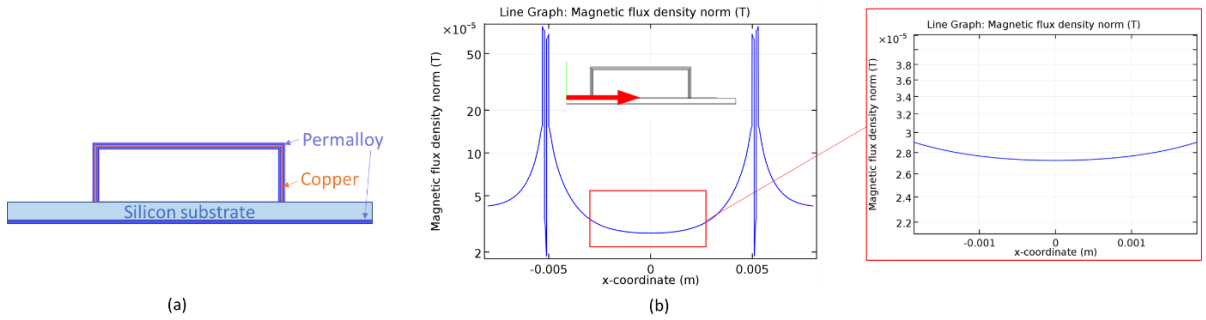
Figure 7.2: *2D cap shield model with bottom permalloy layer. a: The top shield cap and the bottom permalloy layer (100 µm). b: Simulated magnetic flux density for the model. The magnetic flux density along the surface of the MCM (the red line) is 27.3 µT.*

However, the 27.3 µT minimum flux density exhibited by the magnetic shield is still significantly higher than the maximum allowable 4 µT field. The thickness of the Si substrate of the MCM also affects the shielding effectiveness. With a thinner substrate, we get a better enclosure for the shield, thus a lower field inside the shield. Simulations were done to investigate the thickness required for the Si substrate to achieve 4 µT field. Figure 7.3 shows that the Si substrate needs to be less than 10 µm to get the magnetic flux density around 4 µT, which is not practical for the MCM chip.
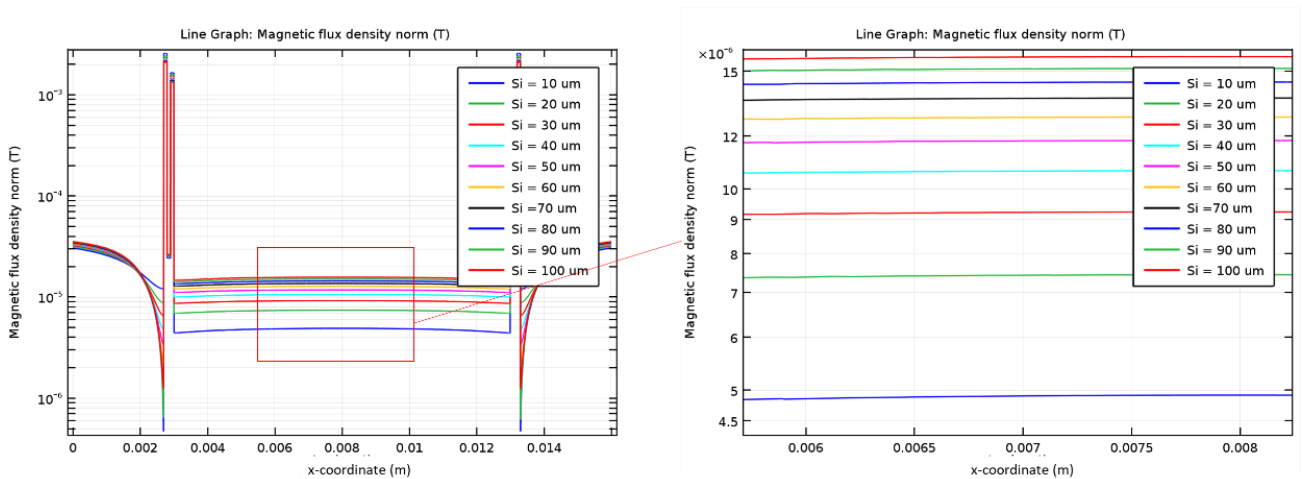
Figure 7.3: *The magnetic flux density at the surface of the MCM at various Si substrates for the MCM.*

83

7.3. 3D shield simulation: Through silicon vias design

To improve the shielding, magnetic through silicon vias (TSVs) composed of permalloy were introduced into the shield design to form a closed loop of the magnetic flux. Four vias were added to the shield design, one at each of the corners of the shield (Figure 7.4(a)). The vias connected the magnetic shield to the permalloy layer beneath the Si substrate, as shown in Figure 7.4(b). To better study the TSV performance, a 3D shield model was built in COMSOL Multiphysics®. The magnetic permeability of the permalloy was set to a constant value $\mu_r = 8500$ [157] to shorten the computation time of the 3D model. The 3-layer shield cap design was changed to 50 μm of permalloy, 50 μm of Cu, and 50 μm of permalloy, and the bottom permalloy was decreased to 75 μm to reduce the fabrication complexity.
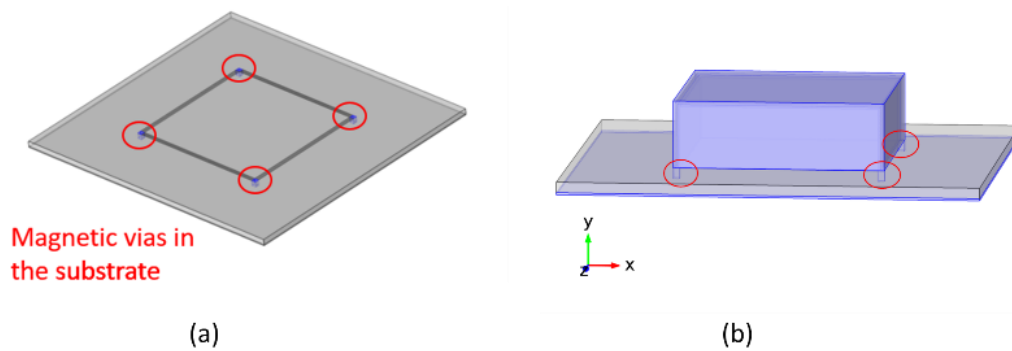
Figure 7.4: *Addition of magnetic vias to magnetic shield. a: Location of magnetic vias at corners of shield. b: The vias connect the shield cap to the bottom permalloy layer beneath the substrate.*

The effectiveness of the TSV in shielding the magnetic field is demonstrated in Figure 7.5, which compares the magnetic flux density inside the shield with TSVs and without TSVs. The minimum magnetic flux density at the surface of the MCM decreases from 27 μT to 2 μT by adding the TSVs at the corners, increasing the shielding factor to $S = 25$.
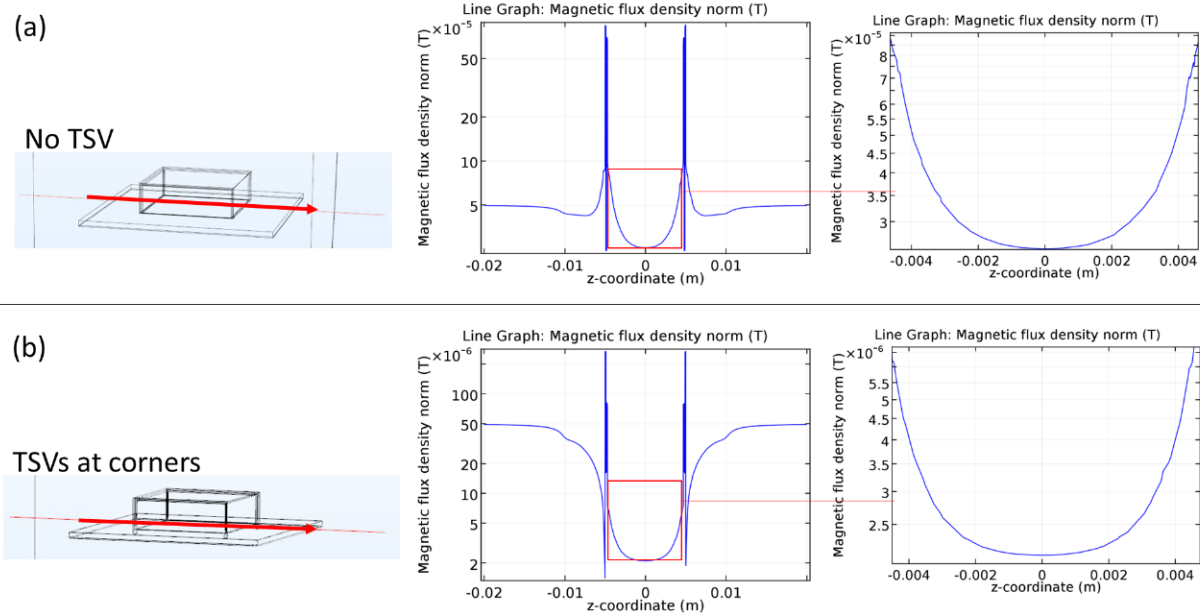
Figure 7.5: *Comparison of the magnetic flux density at surface of the MCM inside the shield (along the red lines). a: When there is no TSV in the shield design. b: TSVs are placed at each corner of the shield.*

The multi-layer shield design with TSVs simulation showed good shielding effectiveness. Meanwhile, it is also important to consider the magnetic material behavior under a strong external field. In ferromagnetic materials, the magnetic moments interact with each other strongly even when there is no external magnetic field present. The moments form in magnetic domains, and the internal fields align the moments in parallel. Under an external magnetic field, the domain walls shift, and larger domains then align to the field. The domain walls will eventually disappear as the external field reaches the saturation field. At this time, the material is fully magnetized, which is called saturation. The permeability of the material decreases as the external field increases near the saturation and finally drops to $\mu_r = 1$ at the saturation field. Since high permeability is the key ensuring the shielding effectiveness, we need to make sure that the field inside the permalloy is not reaching the saturation field. Figure 7.6 shows that the maximum magnetic flux density inside the permalloy material is 0.11 T, much smaller than the saturation

85

field (1 – 1.1 T) [157]. Since the maximum field in the material is an order of magnitude smaller

than saturation, the high permeability assumption for the permalloy should be valid.
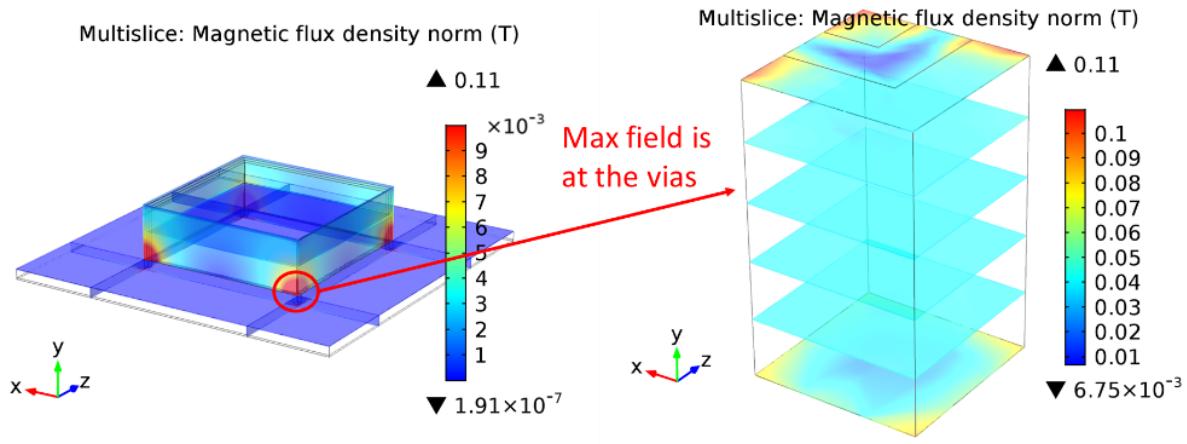
Figure 7.6*: The magnetic flux density simulated inside the permalloy material.*

We showed that 4 TSVs at the corner of the shields help to decrease the minimum field

inside the shield to 2 µT. It is also important to investigate the entire internal field inside the

shield to ensure that the full SCE chip is protected from the external magnetic field. Figure 7.7

(a) displays an isosurface plot of the internal magnetic fields inside the magnetic shield at the

MCM surface, which exceeds the 4 µT threshold. The fields greater than 4 µT are only present

around the perimeter of the shield, and the field at the center area, where the chip will be placed,

is below the threshold. Figure 7.7 (b) shows the contour field lines for 2, 3, and 4 µT internal

fields. The inclusion of the magnetic vias reduces the internal magnetic field of the shield to well

below the 4 µT threshold. Simulations for both the in-plane and out-of-plane magnetic fields

were performed, as shown in Figure 7.8. The white areas shown inside the shield represent areas

where the field is less than 4 µT.
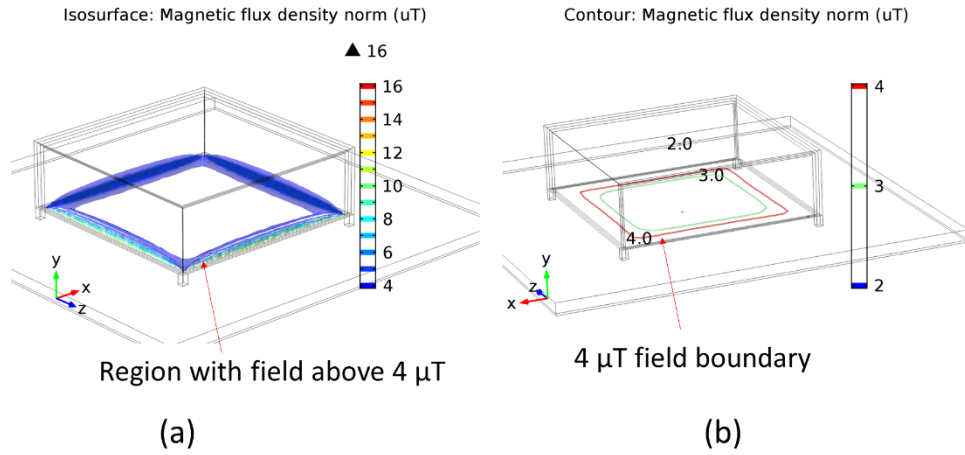
Figure 7.7: *(a) Isosurface plot of internal magnetic fields. (b) Contour plot of the internal magnetic field below 4 µT.*

Figure 7.8: *In-plane and out-of-plane shielding simulations. (a) 50 µT out of plane external field is applied to the magnetic shielding. (b) The magnetic field contours at the bottom of the shield under out of plane external field. (c) 50 µT in plane external field is applied to the magnetic shielding. (d) The magnetic field contours at the bottom of the shield under in plane external field.*

87

The above simulations focused on 5 mm × 5 mm shields, which capture the size scale for state-of-the-art chips. For future chip design, it is likely that chip size will be different. The shield design may need to be modified based on the chip size and field requirements. In preparation for this, simulations with various shield sizes were conducted. The number of vias also influences the shielding effectiveness significantly. Figure 7.9 lists the magnetic flux density simulation results inside the shields for various sizes of the shield with various numbers of vias. The contour plots show the area inside the shield with a magnetic flux density that is below 4 µT. The internal field decreases with the via number increases and also decreases with the shield dimension decreases. For shields with smaller sizes and more vias, the maximum fields on the top of the scale bars are below 4 µT, meaning that all the internal fields are below the threshold. Detailed simulation results of the maximum and minimum magnetic flux density inside the various shields are shown in Table 7.1.
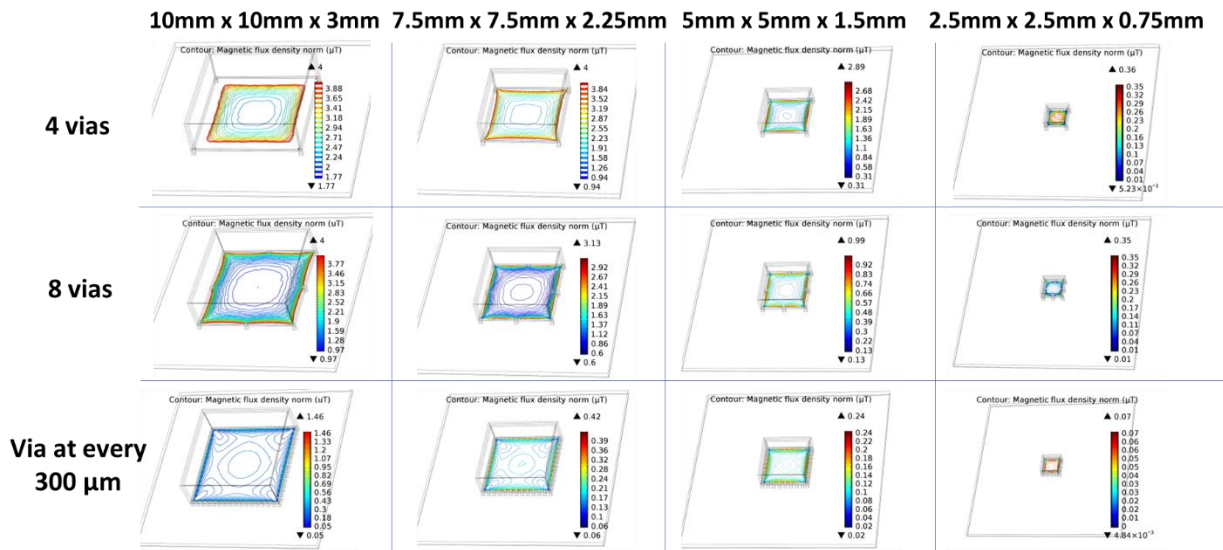
Figure 7.9: *Shields simulation with dimensions of 10 mm × 10 mm × 3mm, 7.5mm × 7.5 mm × 2.25 mm, 5 mm × 5 mm × 1.5 mm, and 2.5 mm × 2.5 mm × 0.75 mm. 4 vias, 8 vias, and via at every 300 µm cases were simulated for each dimension.*

Table 7.1: *The maximum and minimum magnetic flux density simulated at various shield dimensions and vias numbers.*

	10 mm x 10 mm x 3 mm shield	7.5 mm x 7.5 mm x 2.25 mm shield	5 mm x 5 mm x 1.5 mm shield	2.5 mm x 2.5 mm x 0.75 mm shield
4 vias	B_{min} = 1.7658 µT	B_{min} = 0.93952 µT	B_{min} = 0.31358 µT	B_{min} = 0.00523 µT
	B_{max} = 16.634 µT	B_{max} = 8.5751 µT	B_{max} = 2.8885 µT	B_{max} = 0.35521 µT
8 vias	B_{min} = 0.96957 µT	B_{min} = 0.6036 µT	B_{min} = 0.12782 µT	B_{min} = 0.01363 µT
	B_{max} = 6.8364 µT	B_{max} = 3.1303 µT	B_{max} = 0.98995 µT	B_{max} = 0.35216 µT
Via at every 300 µm interval	B_{min} = 0.04714 µT	B_{min} = 0.058204 µT	B_{min} = 0.01784 uT	B_{min} = 0.00484 µT
	B_{max} = 1.4581 µT	B_{max} = 0.4226 µT	B_{max} = 0.2416 µT	B_{max} = 0.07038 µT

Via number increasing ↓   Shield dimension decreasing →   *Field decreasing* ↓   **Field decreasing** →

7.4. Magnetic shielding simulation for chip array

Since the design magnetic shielding is proposed to be used for a multi-chip module, it is important to investigate the shielding effectiveness for the entire SCE chip array. Simulations were performed to verify shield operation in the vicinity of neighboring shields. Figure 7.10 shows the model used to simulate the effects on shielding performance in the presence of proximal shields. Two primary configurations were explored: (1) a single shield centered on the MCM and (2) a 3x3 array of shields. Results for both configurations are shown in Figure 7.11. 200 µT field was used considering the Earth's magnetic field and the field from the current line on the chip. Results from simulations performed suggest that introducing multiple shields in the vicinity of neighboring shields increases the overall shielding performance.
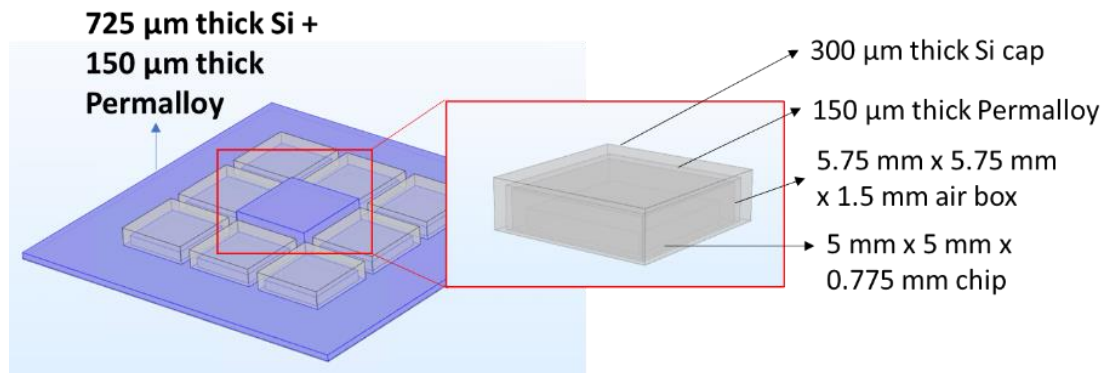
Figure 7.10: *The simulation model to evaluate effects of multiple shields in proximity on a single MCM substrate.*
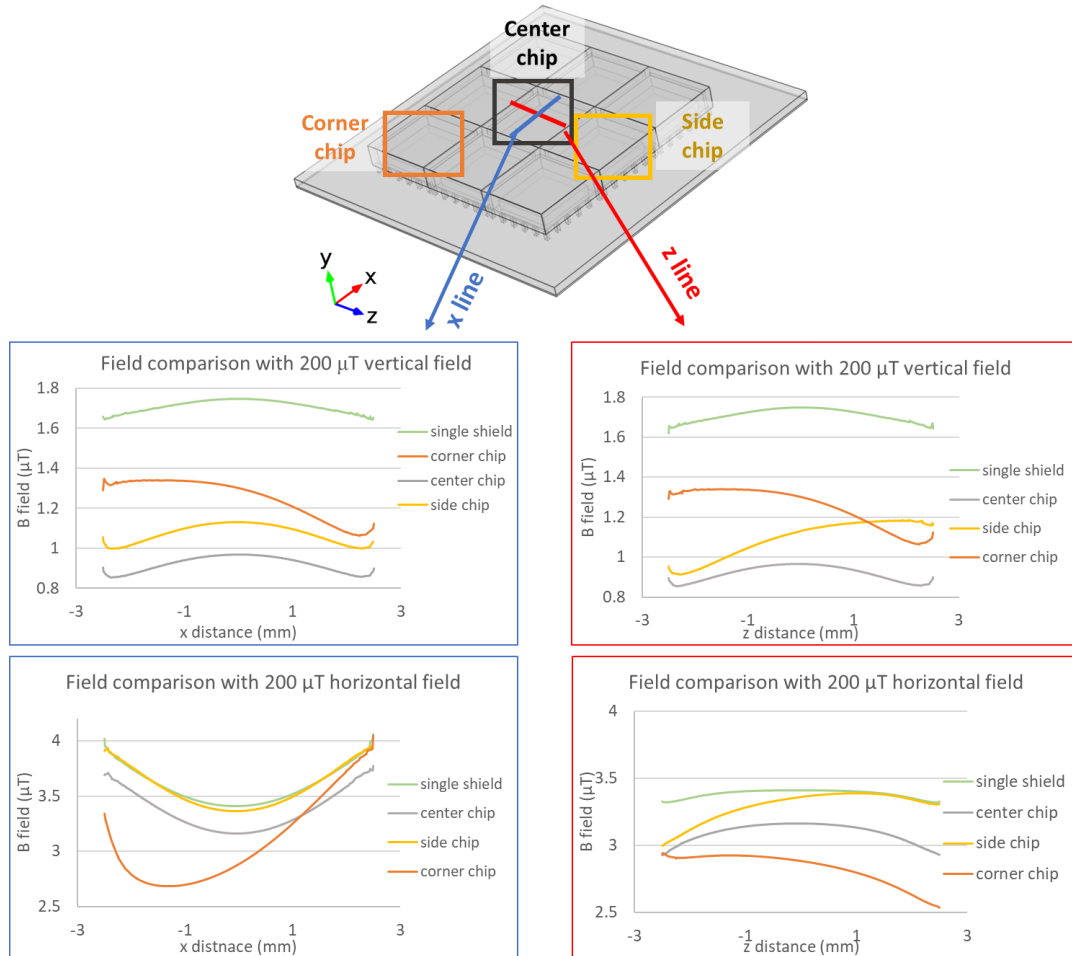
Figure 7.11: *Results from proximity shield simulations. Note that the single shield case is where only the center chip is shielded, and the remaining three cases are when all locations denoted are shielded simultaneously.*

7.5. Heat transfer simulation

We also used COMSOL to simulate the thermal properties of the shields. Cryogenic material properties (e.g., thermal conductivity) were obtained from the literature [158]–[166]. The model was built in Heat Transfer in the Solid module and coupled with the Magnetic Field module through temperature coupling. 1 mW heat source was set at the bottom of the 5 mm × 5 mm chip as the boundary heat source. Assuming an ideal situation, heat sinks were simplified as fixed temperature boundaries of 4 K on the model.
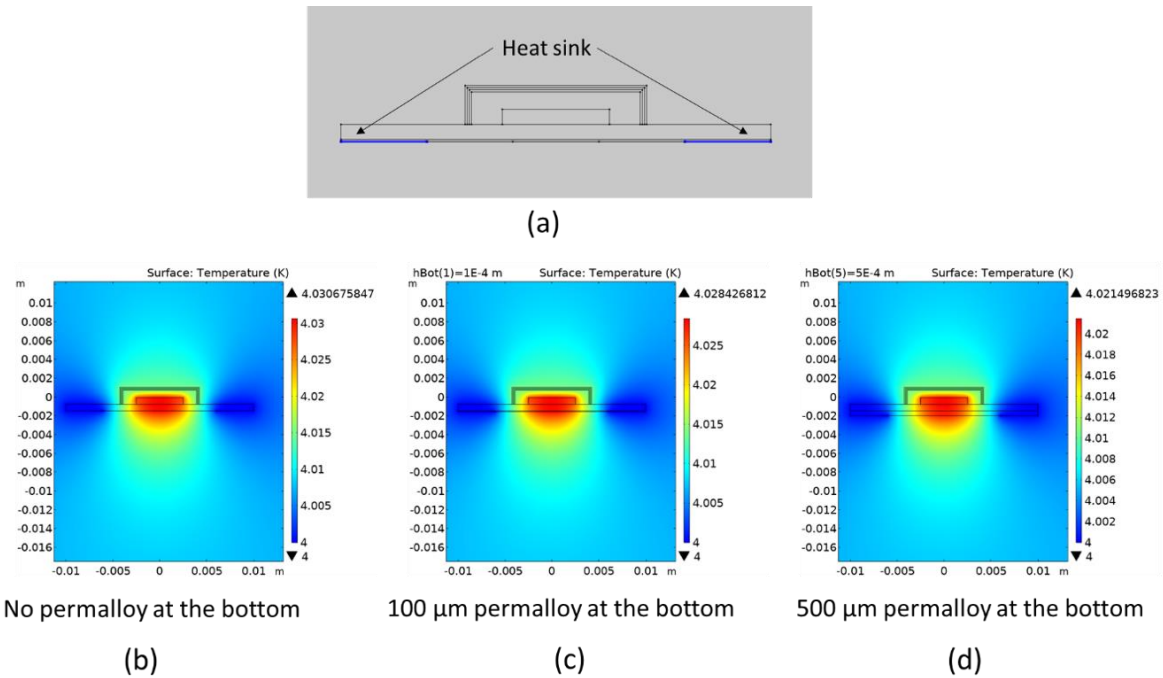
Figure 7.12: Heat transfer simulation with heat sinks at the MCM edges. (a) The model setup. (b)-(d) The simulated temperature maps of the model with various bottom permalloy thicknesses.

The heat sinks were placed at the edges of the MCM (Figure 7.12(a)) to simulate the case where the MCM chip was clipped at the edges. Simulation shows that the temperature increase is only 0.02 K – 0.03 K. A stable temperature ensures that the SCE chip works properly with magnetic shielding. Since the heat sinks are placed at the bottom of the MCM, the thickness of

the bottom permalloy also affects the temperature. With thicker bottom permalloy at the edges, the temperature increase is smaller. If we think of the bottom permalloy as the thermal resistor, increasing the thickness is similar to increasing the cross-section of the resistor. Thus, the resistance is deceased, and the temperature increase is lowered.

Initial simulations show that the thermal ground plane (heat sink) on the back of the substrate under the chip is sufficient for heat transfer. There are other ways to improve thermal conductivity as well. One method is to increase the thickness of electroplated copper layers in the shield cap. We could also add copper vias in addition to mTSVs to help transfer the heat generated from the SCE chip to the environment.

Chapter 8. Shield fabrication

8.1. Magnetic Through Silicon Vias

8.1.1 Process overview

Based on the magnetic field simulation of the shielding, magnetic through silicon vias

(mTSV) are the key to ensuring a sub-4 µT field inside the shield. The microfabrication of these

high-aspect-ratio wafer-thick metal structures has been widely used in packaging, through-wafer

interconnects, and many other MEMS devices and electroplating is the most common technique

used to fabricate metals that are over 10 µm thick on or through the silicon wafers [167]. The

novelty of this work is the integration of soft magnetic materials into TSVs, and the following

process was designed to fabricate the mTSV for shielding.
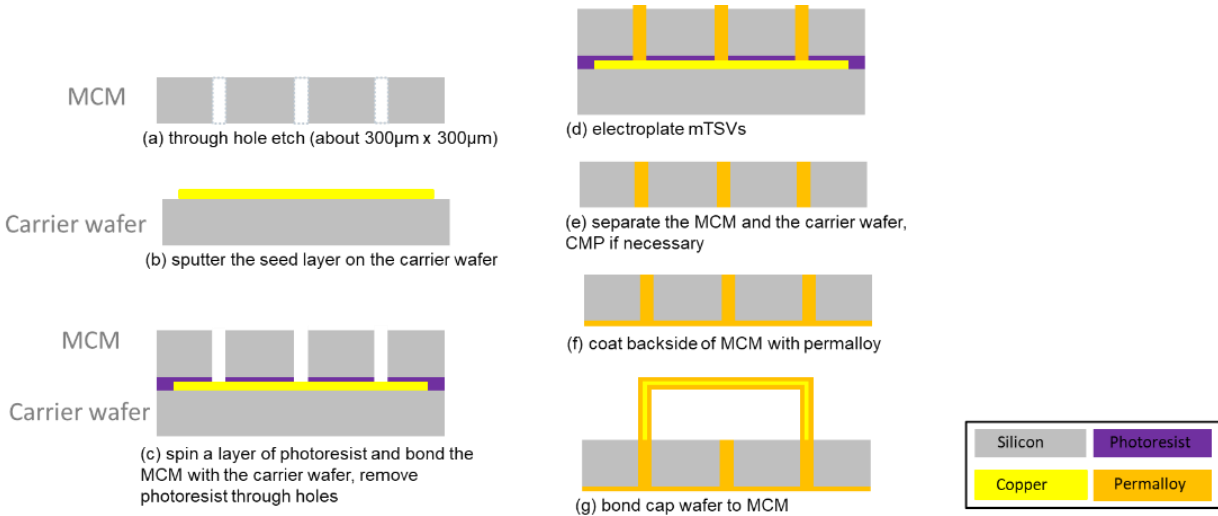
Figure 8.1: *Proposed fabrication process flow for mTSV. MCM with TSVs was integrated with a cap shield. The cap shield can either be microfabricated in a silicon substrate or conventionally manufactured.*

A 750 µm thick silicon wafer (MCM) was first etched with the TSV pattern with a

dimension of 300 µm × 300 µm (Figure 8.1 (a)). The MCM fabrication and TSV etching was

done by our collaborators form Auburn University and MIT Lincoln Labs (LL). In the meantime,

the seed layer was sputtered on the carrier wafer using Denton Discovery 550 (Figure 8.1 (b)).

Then, a layer of the photoresist AZ 1529 was spun on the seed layer, and the MCM wafer was

bonded onto the carrier wafer (Figure 8.1 (c)). The two wafers were exposed with a power of 8.0

mW for 30 sec. AZ developer was used to remove the exposed photoresist through the TSVs.

After that, a DC electroplating process with a current density of 10 A/dm^2 at 60-70 °C was

performed to fill the TSVs with the permalloy (Figure 8.1 (d)). Goldeneye Nickle Iron-BF

solution from Technic Inc was used as the plating solution. Next, the MCM and the carrier wafer

were separated with acetone in an ultrasonic bath (Figure 8.1 (e)). Then we performed the

backside plating. Another seed layer was sputtered on the back of the MCM, and a thin film of

permalloy was electroplated. Finally, the cap shield would be bonded to the TSVs on the MCM.

8.1.2. Bonding between MCM and the carrier wafer

To test the process, we designed a mask with 300 μm × 300 μm vias in a variety of

configurations (Figure 8.2 (a)), and TSVs were laser drilled using LPKF ProtoLaser U4 machine

(Figure 8.2 (b)). The bonded wafers were placed in the permalloy plating solution. However,

bonding failure was found after 4-5 hours of plating (Figure 8.3).
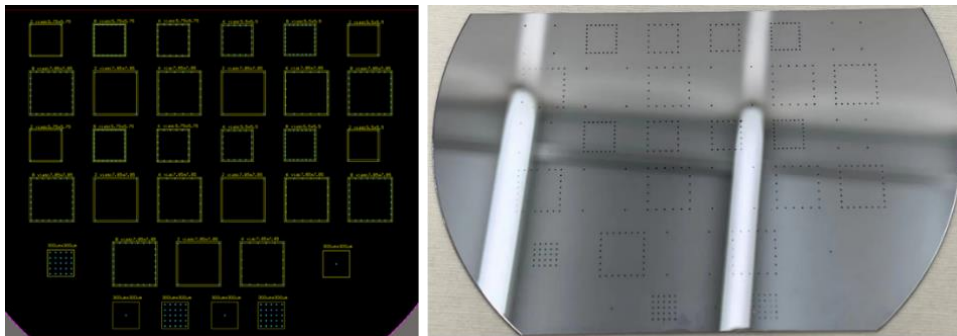
Figure 8.2: *Mask design (left) and drilled TSVs (right) for mTSV electroplating experiments with various configurations.*

The main reason for the bonding failure is that the photoresist needs to be dehydrated to bond the two wafers. Since the most areas of the photoresist were covered by the drilled TSV wafer during the baking process, the photoresist was not fully dehydrated, and the two wafers can be easily separated. This problem can be solved by adding dummy vias on the TSV wafer to help the dehydration of the photoresist. However, this method may not be suitable for the SCE chip since the vias limit the routing space on the MCM. Thus, a pre-baking process was added to help the bonding. After spinning on the photoresist on the carrier wafer, it was first baked on the hot plate for 1 min at 90 °C before the MCM, or the drilled TSV wafer was bonded onto the carrier wafer. We continued the baking process for 2 min after the bonding.
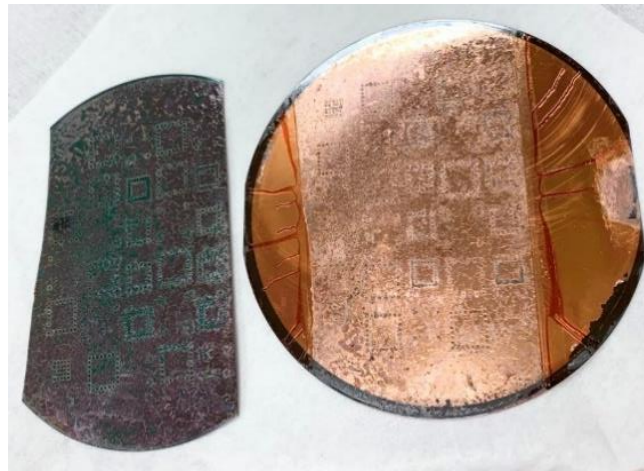
Figure 8.3: *Bonding between the drilled TSV wafer (left) and the carrier wafer (right) failed.*

The pre-baking method was tested using a glass wafer bonded to the TSV wafer. As shown in Figure 8.4 (a), the two wafers were bonded using the pre-baking method. No visible bubbles were shown after bonding. Only tiny bubbles can be found under the microscope (Figure 8.4 (b). The bubbles grew larger after soaking in the solution (Figure 8.4 (c)), but the bonding between the wafer was still strong, and the wafers could only be separated after placing in an ultrasonic acetone bath.
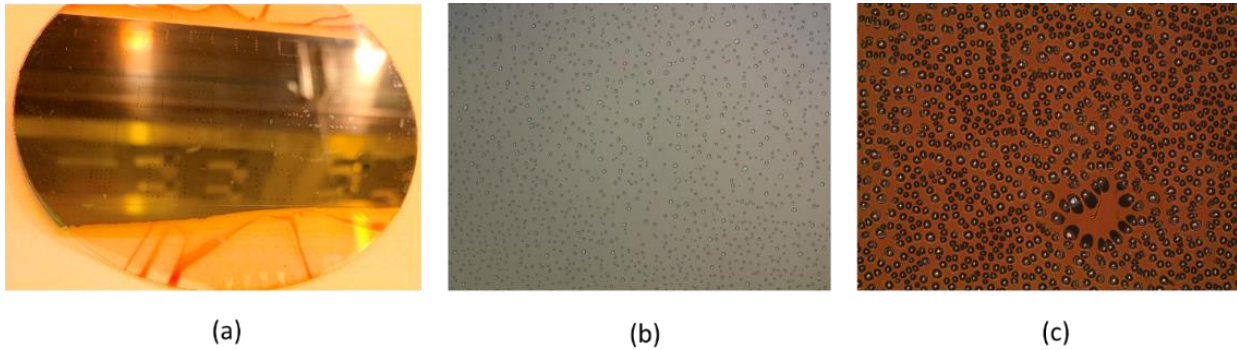
Figure 8.4: *Bonding test using glass wafer. (a) TSV wafer and the glass wafer bonded using the pre-baking method. (b) Microscope pictures of wafers before soaking in the permalloy solution, and (c) after soaking in the permalloy solution for several days.*

8.1.3. Seed layer for the TSV electroplating

The seed layer deposition is usually the first step in electroplating. A thin layer of metal is sputtered or evaporated on the wafer to provide electrical conduction during the electroplating. Denton Discovery 550 was used for the seed layer deposition on the carrier wafer. We used 40 nm of Titanium (Ti) as the adhesion layer and 200 nm of Copper (Cu) as the seed layer. However, in our initial testing of the process, we found that the Cu around the vias sites was dissolved in the permalloy solution after 2-3 days of plating (Figure 8.5). This led to a loss of the electrical connection between the seed layer and the plating area, and the electroplating was discontinued.

The permalloy solution is an acidic solution (pH = 3-4), and the seed layer (Cu) would get dissolved in the solution after several days of plating. This usually won't happen to film plating since the plating time is much shorter. However, for TSV plating, the plating area is deep down through the vias, and thus the solution exchange is limited, which slows down the plating. In addition, film plating usually plates only tens of μm thick, while TSV plates through the entire wafer (500 μm -750 μm). During the long plating process, Cu was dissolved in the acidic permalloy solution, and the electrical connections were lost.

96
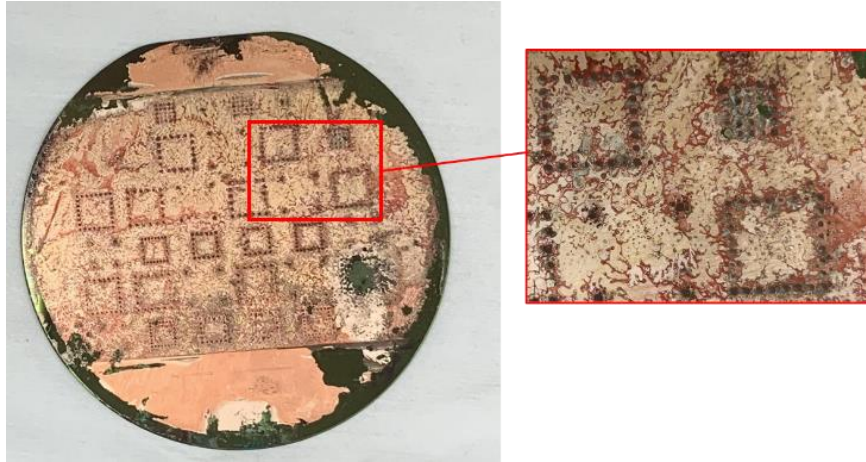
Figure 8.5*: The vias sites on the carrier wafer after 2-3 days of plating. The area in the red rectangle shows that the Cu was dissolved during the plating.*

     Another test was conducted to show the effect of the permalloy solution on the Cu seed layer. The same seed layer (Ti and Cu) was sputtered on a dummy wafer, and then the wafer was soaked in the permalloy solution for a week. As shown in Figure 8.6, the Cu layer was completely dissolved in the permalloy solution, leaving only the Ti layer on the wafer (the silver layer). This test confirmed that the Cu layer might not be suitable for a long-duration TSV permalloy electroplating. To get a stable electrical connection during plating, we changed the seed layer to a 6 nm of Chromium (Cr) adhesion layer and a 200 nm of gold (Au) metal layer, which is more resistant to acid. Figure 8.7 shows the Au layer after a week of permalloy plating (piece plating). The Au layer was still in good condition after the plating.
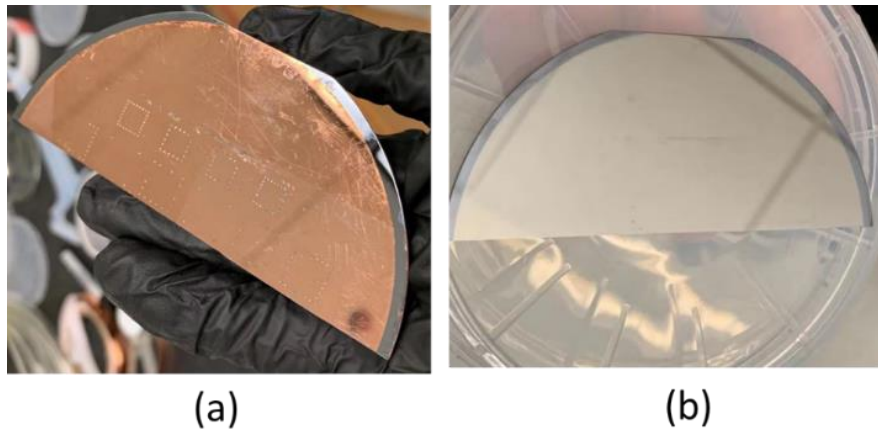
Figure 8.6: *(a) Cu wafer before placing in the permalloy solution. (b) Cu wafer after putting in the permalloy solution for a week.*
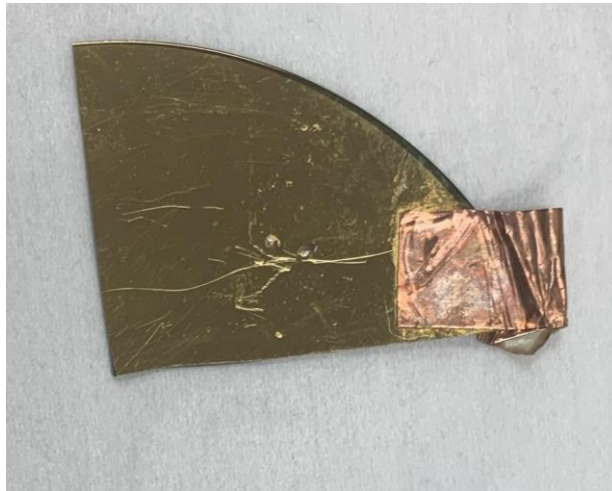
Figure 8.7: *Au seed layer on the carrier wafer after a week of permalloy plating (for pieces plating).*

8.1.4. Electroplating under vacuum

In the initial process development, large bubbles were found inside the TSVs and blocked the electroplating process (Figure 8.8). This is a common issue found in the bottom-up electroplating process as the air and the generated hydrogen bubbles get stuck inside the vias. To solve this problem, we introduced the vacuum plating technique for TSV plating. Studies have

98

shown that an intermittent degassing mechanism effectively removes the trapped air and hydrogen bubbles, which helps fabricate high-aspect-ratio electroplated metals with good quality [168].
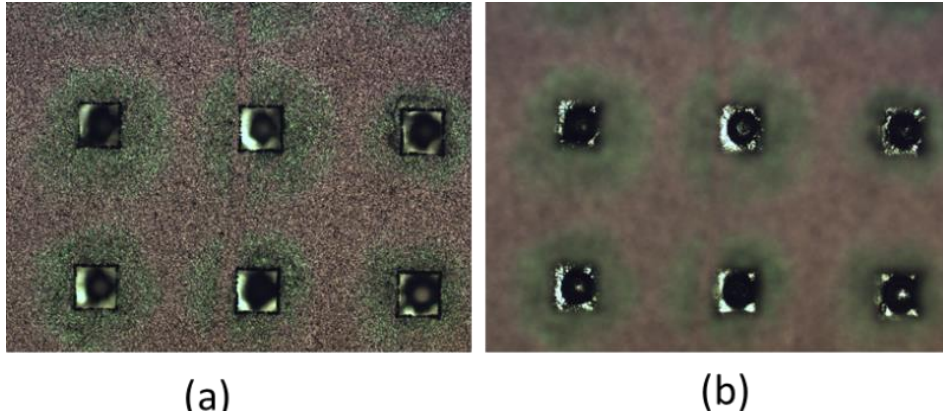
Figure 8.8*: The microscope pictures of the plated TSVs in the initial development process. (a) Top focus. (b) Bottom focus.*

The vacuum electroplating setup is shown in Figure 8.9 and Figure 8.10. A Bacoeng 2.8 QT glass pyrex vacuum and degassing chamber was used for the plating. Two holes were drilled into the acrylic lid for the electrical connections and were sealed with epoxy. The 3-way valve was connected to the pressure gauge, the vacuum pump, and the venting pipe. The permalloy solution was heated up to 60-70 °C during the plating. We first repeated vacuum and venting 2-3 times after placing the sample and before the electroplating to remove the air bubbles that were initially trapped in the vias. During the plating, we pulled the vacuum every hour and maintained the vacuum state for 2-3 minutes before venting the chamber. In this way, we can remove the hydrogen bubbles accumulated in the plating process. The pressure was lowered to around 5 inHg (16.9 kPa) during the degassing stage. Since the boiling point of water varies with the environmental pressure, and the water boiling point at 5 inHg (57 °C) is close to the solution temperature, the pressure needs to be carefully controlled during the degassing stage.

99
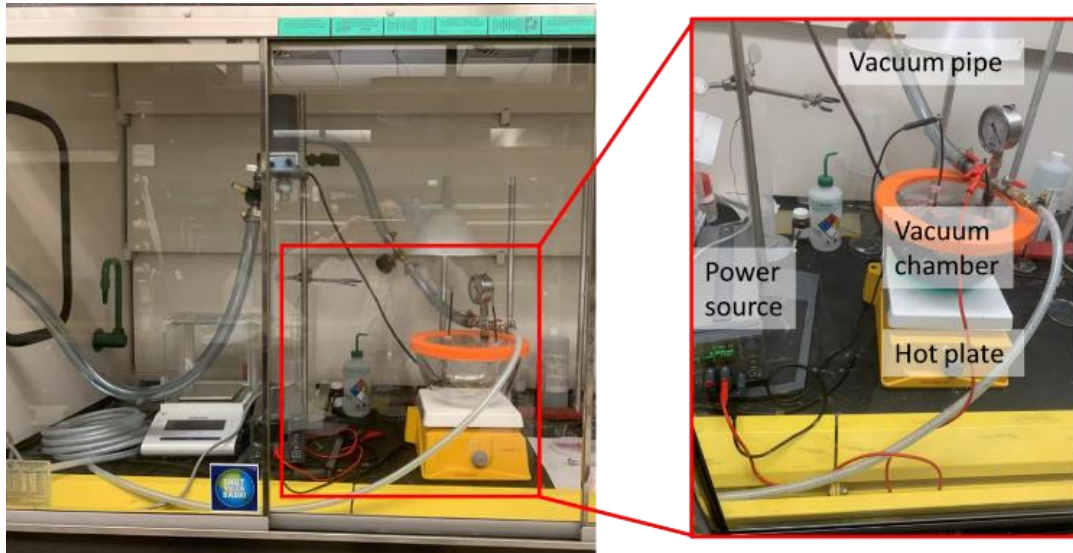
Figure 8.9: *Vacuum electroplating setup.*
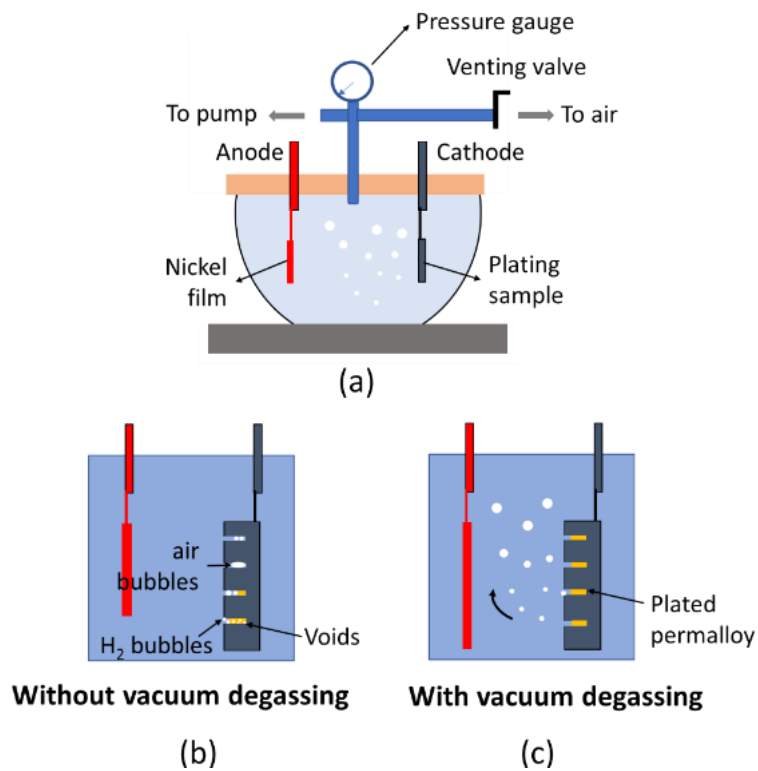
Figure 8.10: *(a) Schematic illustration of the vacuum electroplating process. (b) The air bubbles and hydrogen bubbles are trapped in the vias without the vacuum plating. (c) The air bubbles and hydrogens bubbles are removed in the vacuum pumping stage. Adapted from* [168].

A MCM chip with mTSVs was then electroplated under the vacuum. The MCM chip, which was designed and fabricated by our collaborator from Auburn University, had 5 chips locations and 8 TSVs in total were laser drilled on the chip. As shown in Figure 8.11, the problem of air and hydrogen bubbles blocking plating was mitigated, and we were able to fill some mTSVs with this method. Some of the TSVs seemed to be plated faster than others. This is likely due to varying levels of agitation in the top and bottom parts of the bath. Rotating the orientation of the sample to balance out location-dependent plating is a possible solution.

5 hours of plating   11 hours of plating

16 hours of plating
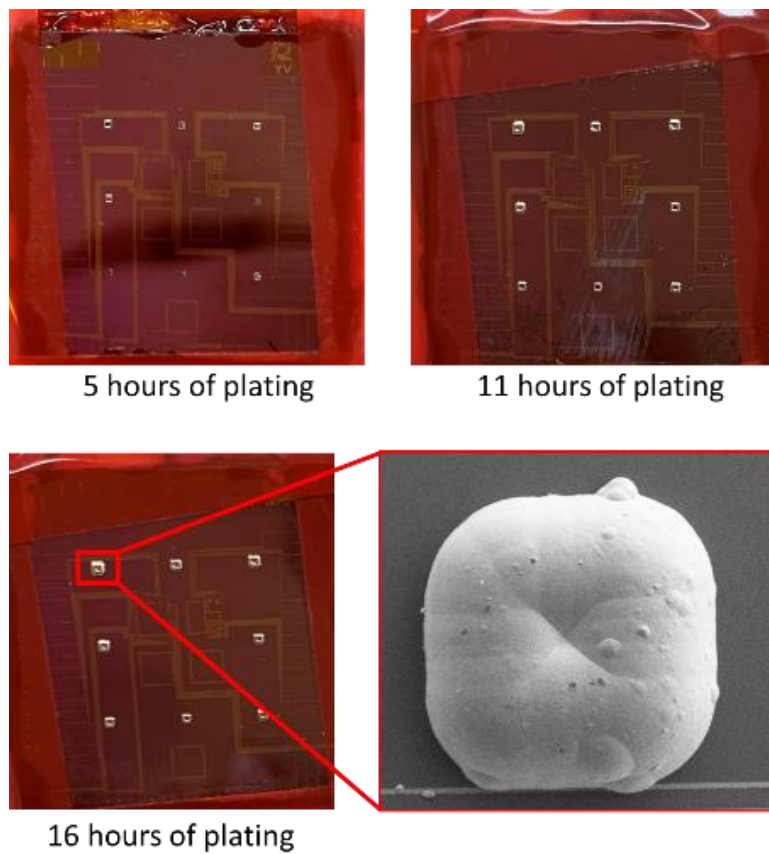
Figure 8.11: Electroplating of MCM structure with laser drilled TSV holes. The red rectangle shows the SEM picture for the plated TSV.

101

8.1.5. SEM and EDS Characterization

Scanning electron microscopy (SEM) is a commonly used technique for surface characterization. It is often combined with energy dispersive spectroscopy (EDS) X-ray diffraction. An electron beam scans across the sample surface in SEM, generating X-ray fluorescence from the atoms, and the energies of the X-ray photons are used for element characterization [169]. In this way, the measurement not only provides high-magnification images of the sample surfaces but also a composition analysis of the elements.

The SEM and EDS characterizations of the electroplated TSVs are shown in Figure 8.12 (a). Two vias, one fully filled and one partially filled, were analyzed. Ni and Fe elements were detected in both vias, and the element composition of different vias is consistent. 11.01% of Fe and 89.99% of Ni were found in the fully filled via, and 10.75% of Fe and 89.25% of Ni were found in the partially filled via. The composition depends on many parameters like the solution properties, plating temperature, and current density. The current density is now limited by the resolution of the power supply. By reducing the plating current density, we expect to get the Ni: Fe ratio closer to the desired ratio of 80:20. A SEM image for the cross-section of the plated TSVs is shown in Figure 8.12 (b). The vias' side walls were fully plated, capable of directing the magnetic flux through the vias and providing effective shielding performance.
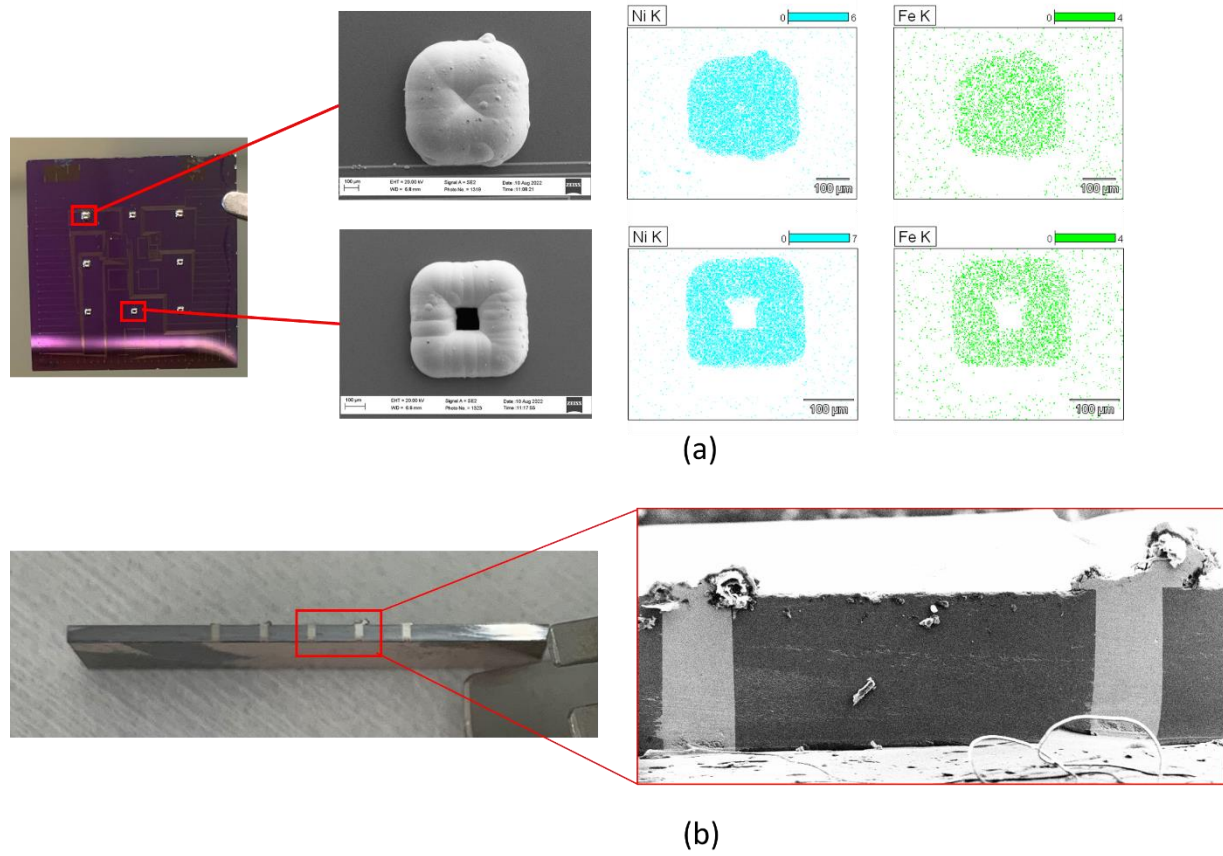
Figure 8.12: (a) SEM and EDS measurements for the plated TSVs. (b) SEM image for the cross-section of the plated TSVs.

8.2. Multi-layer cap shield

8.2.1. Process overview

A process was developed for deep (> 1000 μm) shield caps that are to be placed over the MCMs. The process involved deep etching using KOH and a silicon nitride hard mask, and then electroplating alternating layers of Cu and permalloy. A detailed process flow is shown in Figure 8.13. First, dicing lanes and alignment marks were etched on a 2.1 mm thick wafer using Technics Micro-RIE Series 800. Then a thick layer of low-stress nitride was deposited using LPCVD. A layer of photoresist was coated on the wafer and then developed with the cap shield

pattern. The nitride was etched using Oxford 80+ at the cap shield location. The wafer was then placed in the KOH solution for the deep etch process. The depth for the cap was over 1 mm. The next step was to sputter the seed layer at the shield location and then electroplated alternating Cu and permalloy layers. The wafer can be cut into individual cap shields and integrated into the MCMs.

(a) Etch dicing lanes and alignment marks

(b) LPCVD low-stress Nitride (~1μm)

(c) Spin on photoresist and pattern the shields

(d) Etch the Nitride at the patterned shields

(e) KOH etch the patterned shield (~ 1.5mm)

(f) Deposited seeding layer and electroplate permalloy

(f) Permalloy-Cu-permalloy plating

Silicon	Photoresist
Nitride	Copper
	Permalloy
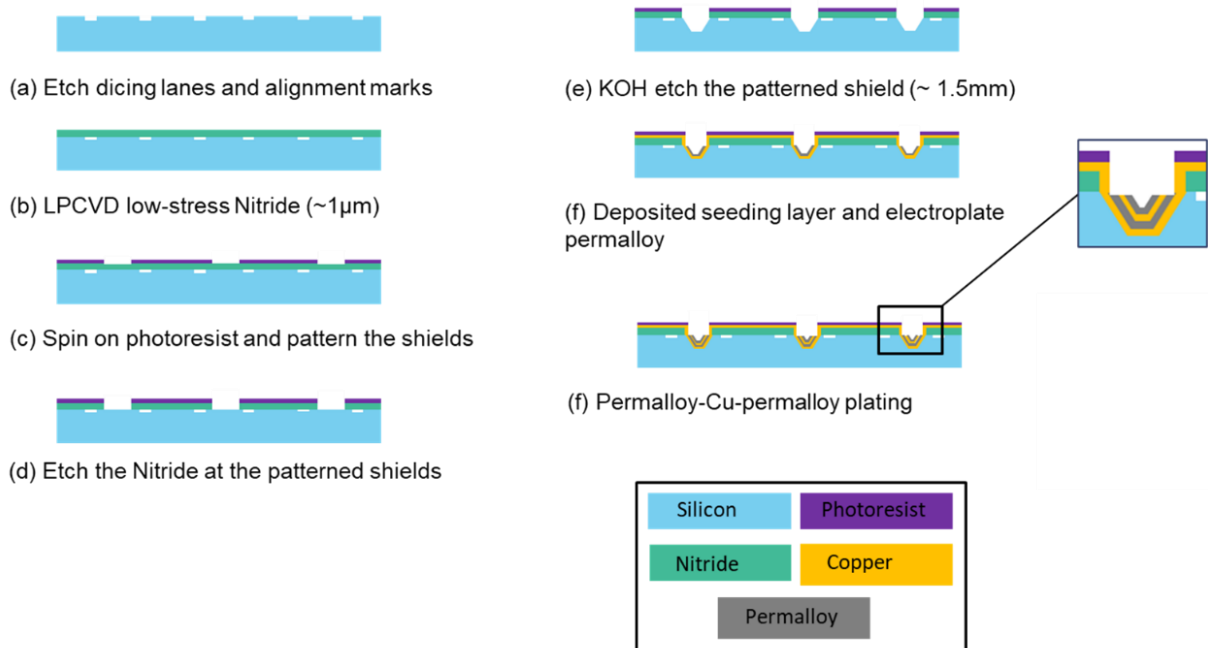
Figure 8.13: Proposed fabrication process flow for cap shield.

8.2.2. KOH etched cavity

KOH etch is an anisotropic Si etch process and is helpful in batch fabrication, providing sloped sidewalls. The sidewalls are defined as <111> plane, and the etched <100> plane is at 54.74 ° relative to the <111> plane. In the initial test, 300 nm of nitride was deposited on a 2.1 mm thick wafer by LPCVD. Then the wafer was coated with AZ1529 photoresist and developed with a mask. Squares with a dimension of 7.85 mm × 7.85 mm and alignment marks were

patterned on the wafer, where the nitride was etched with the Oxford 80+ tool (Figure 8.14 (a)).

The wafer was then etched in 1 liter of 45% KOH solution at 120 °C for 7 hours. 0.15 g sodium

dodecyl sulfate was added to the solution as the surfactant to help detach the hydrogen bubbles

from the wafer during the etch, improving the surface roughness [170]. The depth for the 4

cavities was measured to be: 0.974 mm, 0.976mmm, 0.978 mm, and 0.972 mm (Figure 8.14 (b)).

About 60 nm of nitride was etched in this process. However, large pinholes were found, and the

cross-shaped alignment marks became rectangles after the etch (Figure 8.15), which would affect

the cap shield integration process with the MCMs. A thicker layer of nitride was necessary for the

long KOH etch.

(a)　　　　　(b)
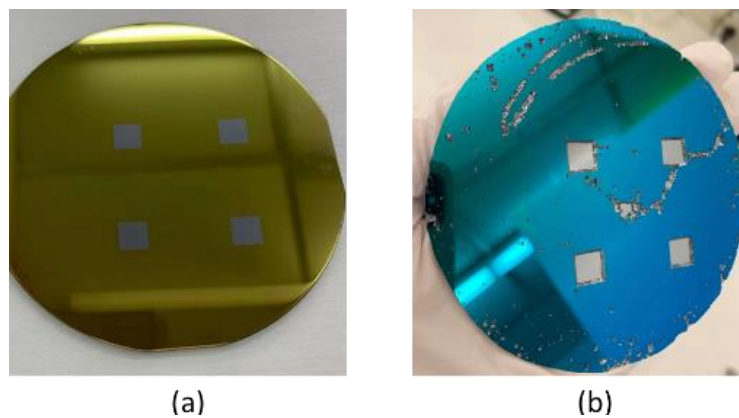
Figure 8.14: Wafer for the KOH etch. (a) Cap shield locations and alignment marks were patterned on the wafer. (b) Wafer after 7 hours of KOH etch.

(a)　　　　　(b)　　　　　(c)
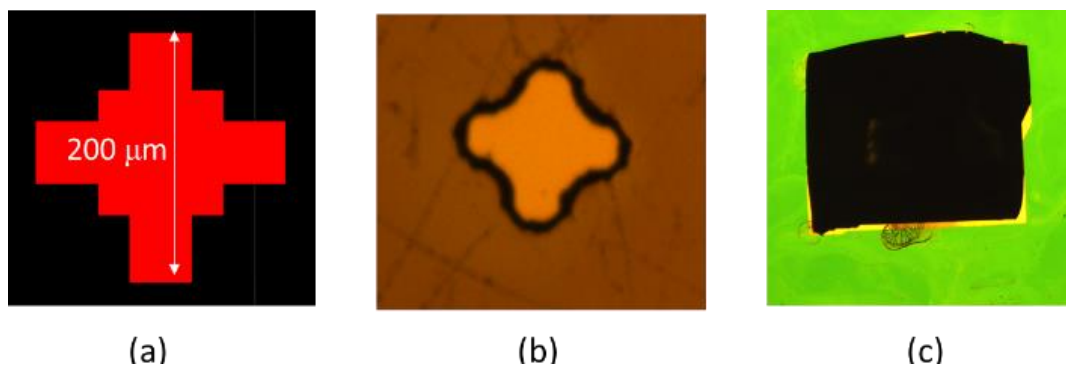
Figure 8.15: Alignment mark for the cap shield wafer. (a) Alignment mark design. (b) Alignment after photoresist development. (c) Alignment mark after KOH etch.

Based on experience from the first experiments, we slightly changed the development process for a better-quality cap shield. The dicing lanes and alignment marks were first etched on the wafer before depositing the nitride layer. Technics Micro-RIE Series 800 etched the lanes and marks for 10-20 nm deep. Then 1 μm thick low stress nitride was deposited with the LPCVD (Figure 8.16 (a)). Then the cap shield locations were defined in a similar way as before. The dicing lanes and alignment marks can be seen clearly after the nitride deposition (Figure 8.16 (b)(c)).
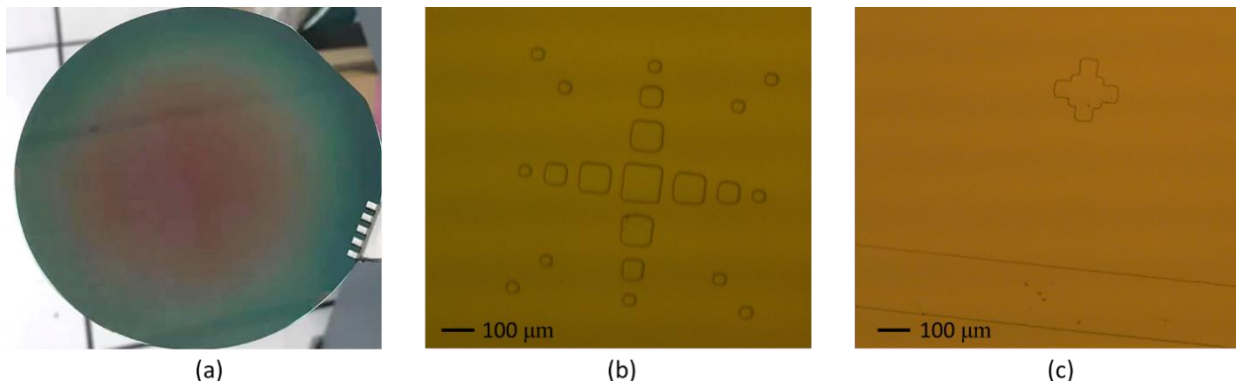
Figure 8.16: *Wafer after nitride deposition. (a) About 0.92 μm (red) to 1 μm (green) thick nitride was deposited. (b)(c) Alignment marks and dicing lanes after the nitride deposition.*

The wafer was then KOH etched for 8.5 hours, and an average depth of 1.1235 mm was reached, providing enough space to enclose a 5.5 mm × 5.5 mm × 0.75 mm chip (Figure 8.17). The depth was consistent for the cavities at different locations on the wafer. The etching rate was also stable throughout the etching process (Figure 8.18). About 0.81 – 0.88 μm of nitride was left after the process. With a 1 μm thick nitride, the wafer surfaces were much smoother than before.
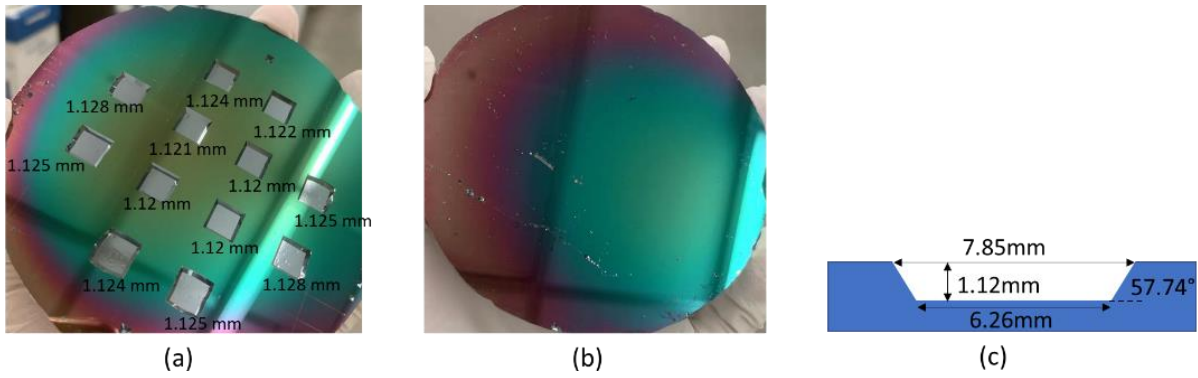
Figure 8.17: *Wafer with 1 μm nitride after 8.5 hours of KOH etch. (a) The front side of the wafer. The depth of each cavity was labeled. (b) The back side of the wafer. (c) Cross-section drawing of cavity dimensions.*
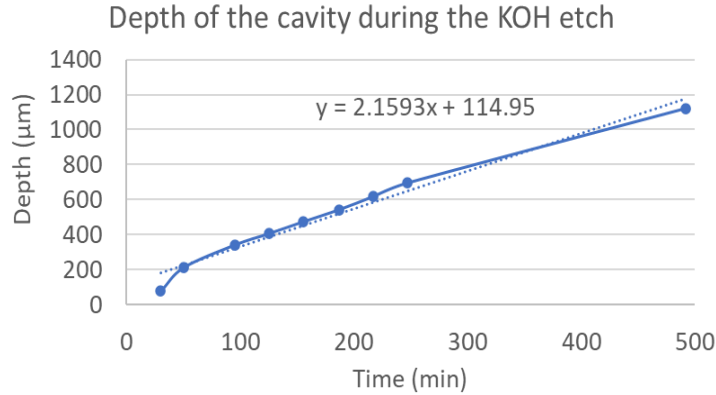
Figure 8.18: *Etch depth vs time for KOH etch process. The etch rate was faster at the beginning and then stabilized at 2.16 μm/min.*

A seed layer was then sputtered on the etched wafer with 40 nm of Ti, 200 nm of Cu, and 40 nm of Ti (Figure 8.19). The top Ti layer protected the Cu from oxidation and was removed using 1% Hydrofluoric acid before electroplating.
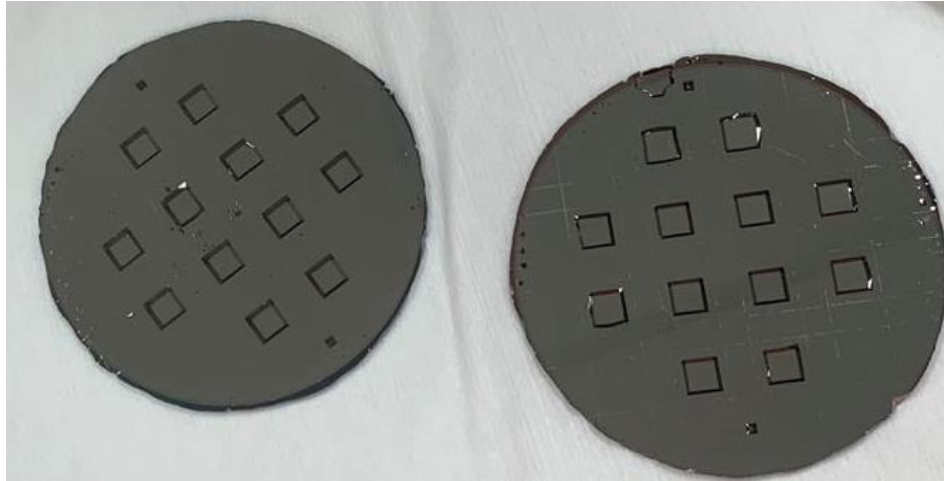
Figure 8.19: Wafers after seed layer deposition. Cavities with an average depth of 1.49 mm (left) and an average depth of 1.12 mm (right) were KOH etched.

8.2.3. Multi-layer electroplating

After developing the etch process, we electroplated alternating layers of permalloy and copper in the shield cavities. The study has shown that for DC magnetic shielding, a comparable or even greater shielding factor can be achieved by alternating between layers of magnetic and non-magnetic material [128]. Moreover, using less permalloy is beneficial because it allows for lower material stress.

Based on the simulation, the cap shield should consist of 50 μm of permalloy, 50 μm of Cu, and 50 μm of permalloy. However, during the electroplating of the first permalloy layer, the permalloy started to peel off at a thickness of 40 μm (Figure 8.20). The edges of the film curled due to strong internal stress, and the film was less adhesive to the substrate. Using lower current density can help reduce internal stress [171], but the applied current was also limited by the power supply resolution.

108
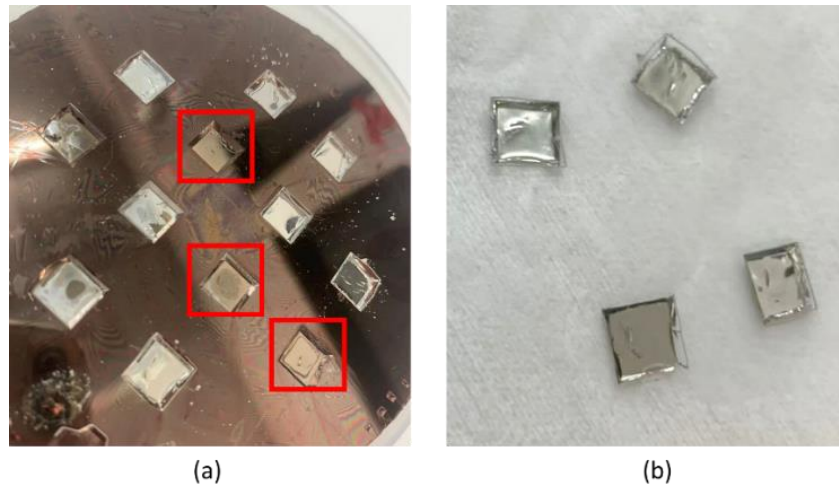
Figure 8.20: *The 40 μm-thick permalloy layer peeled off from the substrate. (a) the Si wafer substrate. The plated permalloy is silver in color. The red rectangles show the Cu seed layer after permalloy peeling off. (b) The peeled-off permalloy layer.*

To solve the peeling-off problem, we changed the plating area to the entire Si wafer so that the permalloy was less easy to peel off from the cavity edge. What's more, we decreased the thickness of each layer to 10 μm while increasing the layer number to 6 layers. Simulation has shown that with 6 alternating thin permalloy-Cu layers, the shielding effectiveness of the cap shield is similar to the case where we have a single 150 μm permalloy layer or 3 alternating layers with 50 μm thickness (Figure 8.21) under a fixed permeability assumption ($\mu_r = 8500$). A 6-layer shield was successfully electroplated with good film adhesion on the substrate (Figure 8.22). However, this method covered the dicing lanes and alignment marks that were initially etched on the wafer. For future process development, dicing lanes and alignment marks should also be patterned on the cap shield wafer after the electroplating.
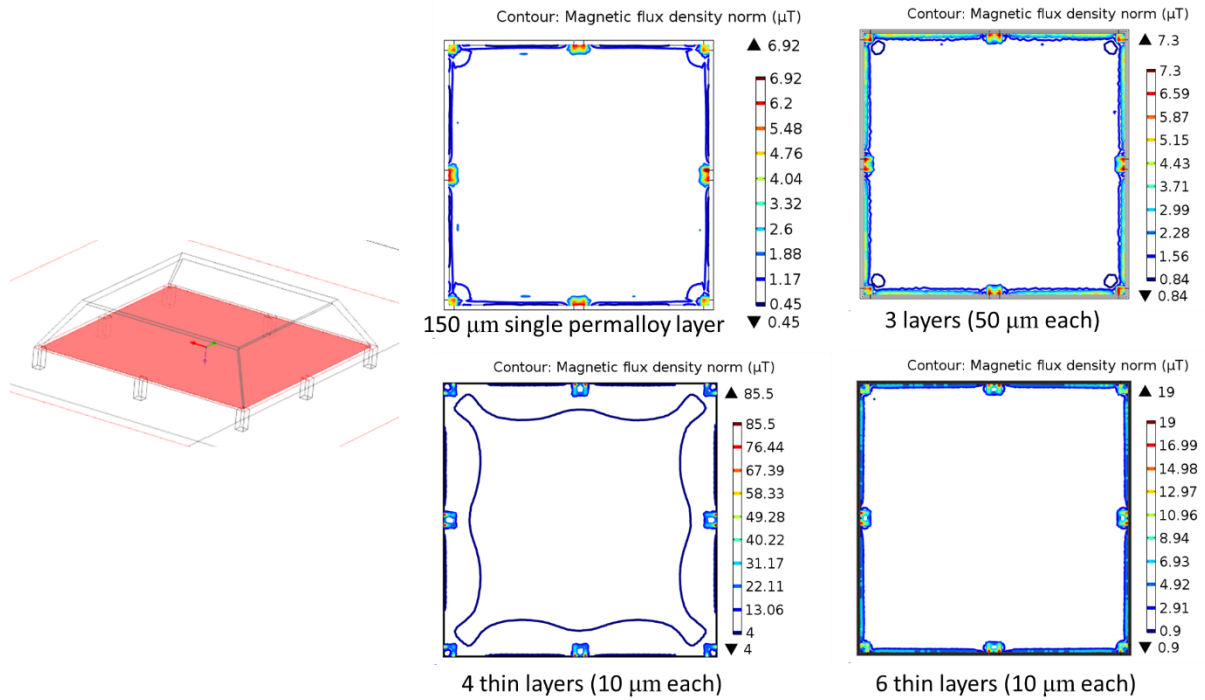
Figure 8.21: *The magnetic flux density inside the shield at the MCM surface (the red area) with various cap shield layer configurations.*
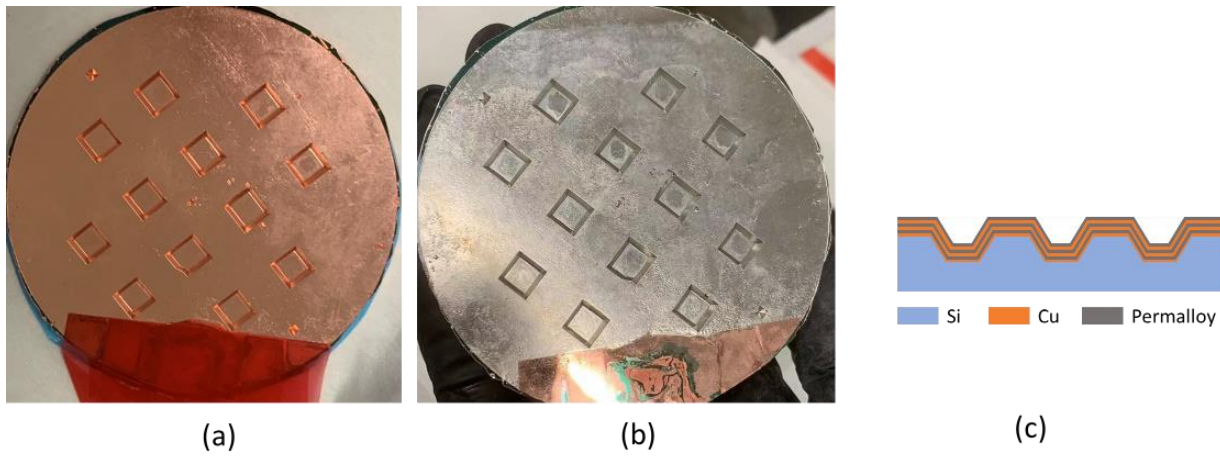
Figure 8.22: *Wafer with 6 thin alternating permalloy-Cu layers electroplated. (a) The Cu layer is plated on the wafer. (b) The permalloy layer is plated on the wafer. (c) Schematic of the cross-section.*

8.2.4. SEM and EDS characterization

The electroplated cap shield wafer was diced to allow for a cross-section view of the multi-layer shield. SEM and EDS measurements showed distinct layers of the plated material. As shown in Figure 8.23 and Figure 8.24, 6 alternating layers of Cu and permalloy (NiFe) were found at both the corner and center part of the cap shield. The sample was sent to Auburn University for low-temperature test and MCM bonding test.

(a)

(b)

(c)
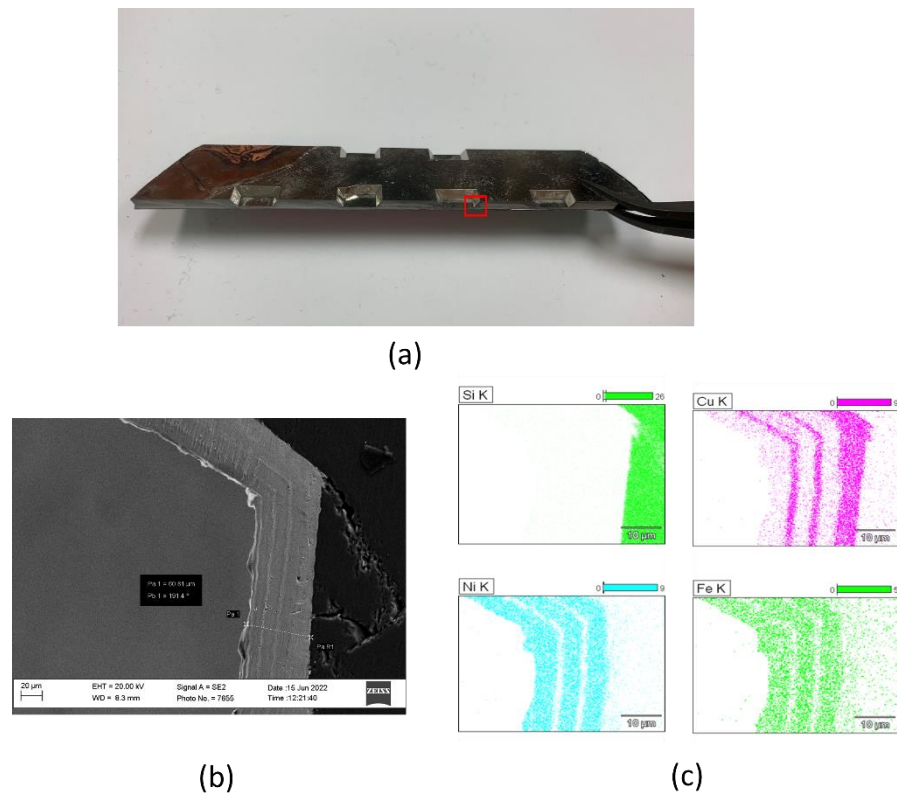
Figure 8.23: The SEM and EDS measurements taken at the corner of the cap shield.

(a)

(b)   (c)
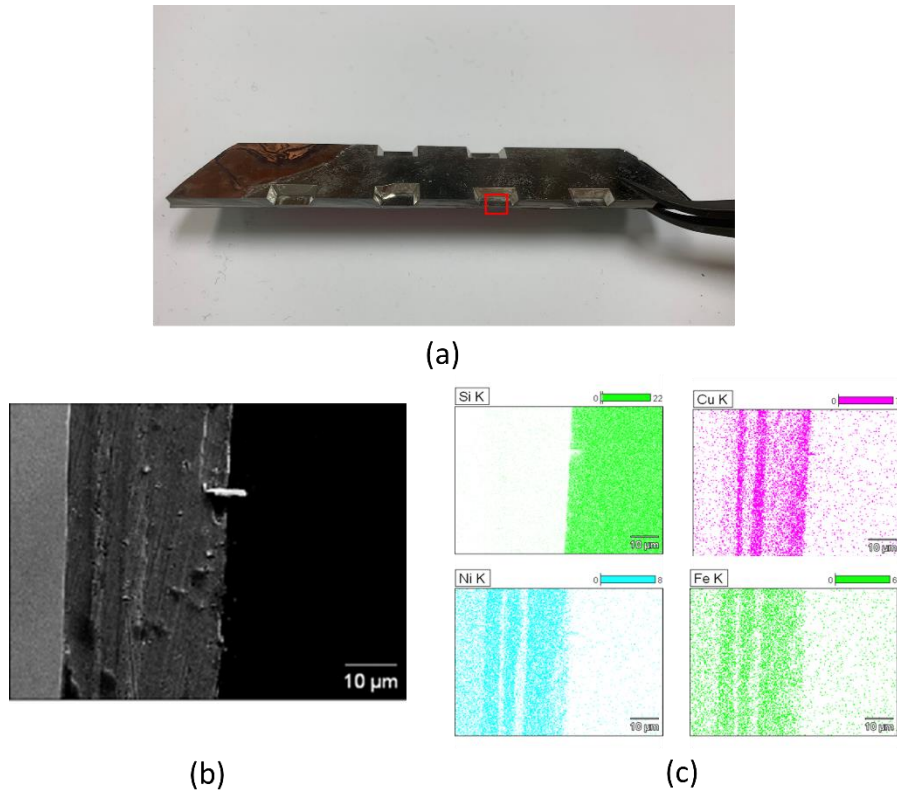
Figure 8.24: The SEM and EDS measurements taken at the center of the cap shield.

8.3. Backside permalloy layer electroplating

Based on the simulation study, a layer of permalloy on the backside of the MCM would help improve the magnetic effectiveness of the shield. We went through several iterations of the plating process, improving the quality of the plating film in each iteration.

A 2 cm $\times$ 2 cm film was electroplated on an Au dummy wafer. On the first try, we used a current density of 10 A/dm^2 as recommended by the datasheet and plated it for 20 minutes. A 50 μm thick film was plated. The plating area was defined by tapes, and permalloy was plated in the gap of the tape, which led to rough surfaces at the edges. For the second try, the plating area was defined by the photoresist, and the current density was decreased to 2.5 A/dm^2. The plating rate

was slower with lower current density, but the film quality was largely improved. The film

thickness was 80 μm after 2 hours of plating. However, the adhesion strength of the film on the

substrate was not sufficient, and the film peeled off after ultrasonic bath cleaning. To relieve the

film stress which caused the detachment issue, we reduced the plating time to one hour in the

third trial and plated a 40 μm thick film. The adhesion of the film improved but still detached

from the substrate after the tape test. In the next iteration, we further decreased the current

density to 1.25 A/dm^2 and plated for 1.5 hours. The film thickness was 25 μm with good adhesion

on the substrate, surviving the tape test. Table 8.1 lists the plate rates at the 10 A/dm^2, 2.5 A/dm^2,

and 1.25 A/dm^2 current density and the Ni: Fe composition in the plated films. Further

investigation on the current density, plating time, and solution chemistry may be needed to

achieve a good-quality film for the backside plating.
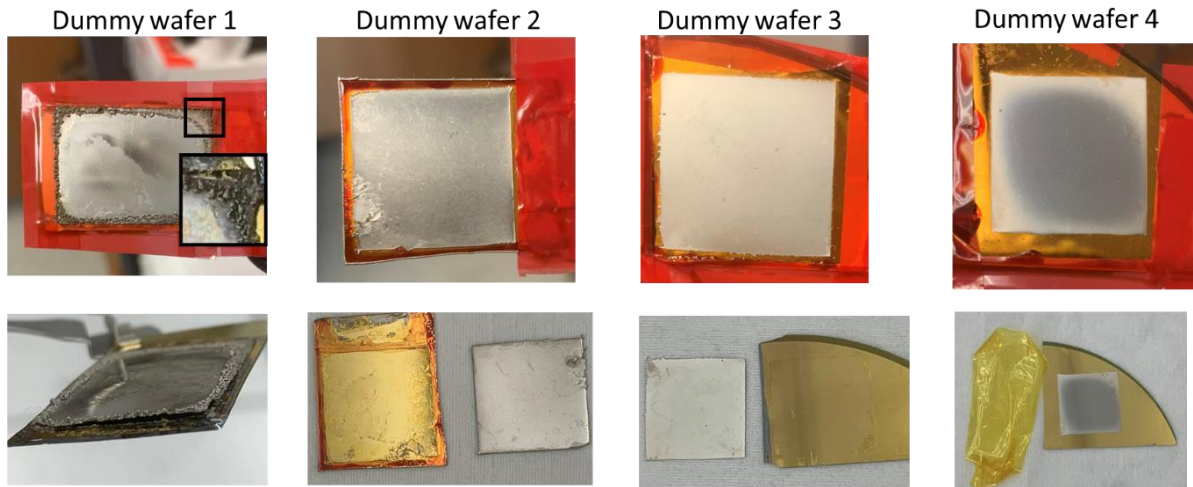
Figure 8.25: *Films electroplated on the dummy Au wafers, with improving quality of the plating film in each iteration. Dummy wafer 1: plated with 10 A/dm^2, 50 μm thick; dummy wafer 2: plated with 2.5 A/dm^2, 80 μm thick; dummy wafer 3: plated with 2.5 A/dm^2, 40 μm thick; dummy wafer 4: plated with 1.25 A/dm^2, 25 μm thick.*

Table 8.1: *The plating rate for various plating current densities and the corresponding Ni: Fe ratio.*

Current density	Plate rate	Ni percentage	Fe percentage
10 A/dm^2	2.5 μm/min	93.14%	6.86%
2.5 A/dm^2	0.67 μm/min	88.82%	11.12%
1.25 A/dm^2	0.28 μm/min	90.76%	9.24%

A seed layer with 40 nm of Ti and 200 nm of Cu was sputtered on the backside of the MCM chip (Figure 8.26 (a)). A constant current density of 1.25 A/dm^2 was used on 3 different chips with various plating times. The plated film thickness was measured to be 27.4 μm, 51.8 μm, and 100.8 μm, with a plating time of 90 min, 180 min, and 300 min, respectively. The average plating rate is 0.31 μm/min. All the plated films had good adhesion on the MCM chip.
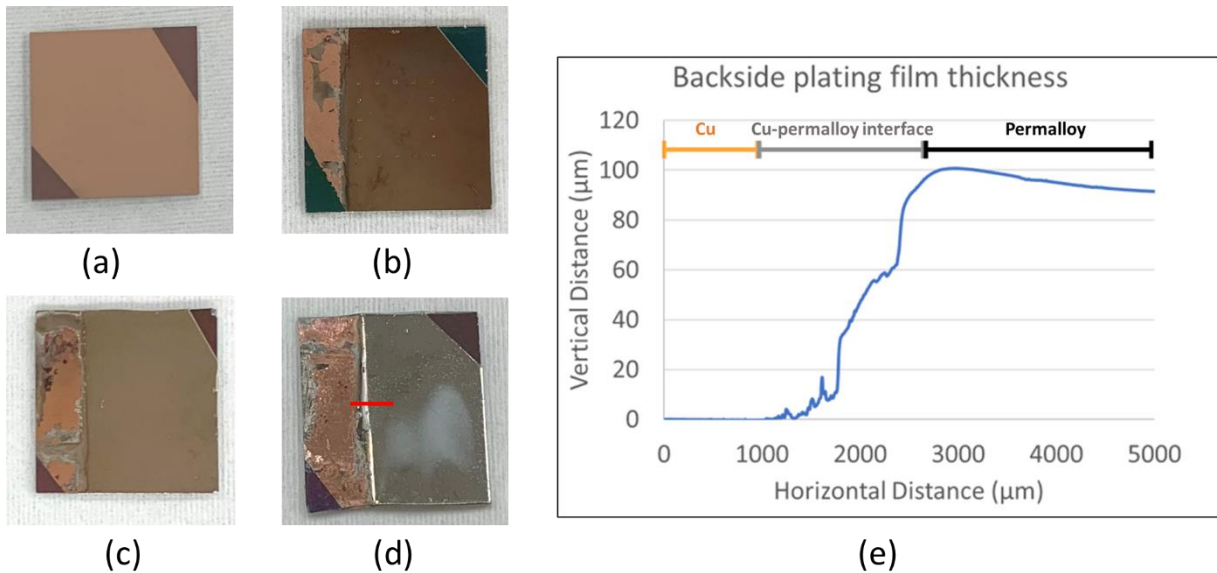
Figure 8.26: *Backside plating samples. (a) The seed layer was sputtered on the backside of the MCM chip. (b) 27.4 μm of permalloy was plated. (c) 51.8 μm of permalloy was plated. (d) 100.8 μm of permalloy was plated. (e) The thickness of the permalloy was measured by Dektak 6M profilometer along the red line labeled on (d).*

Chapter 9. Future Work

The focus of this part of the dissertation is on the design and fabrication of the magnetic shielding for SCE MCM. Further investigations on the shield development process, shield integration, and shielding effectiveness are needed for this work.

As discussed in the previous section, work will be done to improve the development process. First of all, we will continue to improve the NiFe stoichiometry. The ratio of Ni: Fe was measured to be 90:10. By reducing the plating current density, we expect to get the Ni: Fe ratio closer to the desired ratio of 80:20. Power supply with less than 1 mA resolution could be used to apply lower current density during electroplating.

Lower current density can also help with the through-hole plating. Usually, the current density at the hole's top opening is higher than the bottom, and the edges of the holes have more ions accumulated. This mismatch in current density leads to the edges plating faster than within the holes and the formation of voids inside the vias [172]. More uniform electroplating and improved through-hole electroplating can be achieved by using a lower current density.

Secondly, a novel electroplating setup could be incorporated to improve the plating quality. We are now using the DC current source during the electroplating. By switching to pulse reverse techniques, we would be able to have better control of the composition and thickness of the plated structure with enhanced bath stability and efficiency [173]. Additionally, the reverse current protects the edges of through holes and lowers the deposition at the edges [174]. This is beneficial for the TSV plating as it ensures a uniform thickness of permalloy.

The fabricated shields are going to be integrated with the SCE MCM to perform the shielding for an individual superconducting chip. We will closely collaborate with the collaborators from Auburn University to pick and place and bonding of cap shields onto the

MCM. We plan to use a flip chip bonder machine like the FC150 tool to bond shields, the

individual chip, and the MCM. Tooling can be machined from aluminum with various shield

dimensions and MCM designs. Epoxy underfill will be used to adhere shields to substrates.

The shielding effectiveness of the fabricated magnetic shields should be carefully

characterized at both room (RT) and cryogenic temperatures (4 K). The magnetic field inside the

shield will be measured with and without the shield, and the shielding factor could be calculated.

Based on our initial investigation, RT shield testing results are similar to the shielding

performance at cryogenic temperatures, and in fact the shield performed slightly better at 4 K

than at RT. Thus, RT shield test may serve as good prediction for the performance of magnetic

shields at cryogenic temperature. Moreover, future magnetic shield design should consider the

thermal shock at cryogenic temperature. Thermal stresses due to the coefficient of thermal

expansion (CTE) mismatch of the materials can result in fracture of the shield, and future shields

could be designed to reduce the likelihood of failure due to thermal stress at cryogenic

temperatures.

Chapter 10. Conclusion

Overall, this work has proposed a novel way to isolate SCE chips from each other and the external environment. The shield design was optimized through FEA simulation, and the fabrication process of the proposed shield design has been developed. The microfabrication of the high-aspect-ratio magnetic through silicon vias, the sub-millimeter multilayer cap shield, and the thick electroplated backside film demonstrate a promising magnetic shielding method for single chips on MCM. The scalable and flexible magnetic shield design can also be applied to other magnetically sensitive microelectronics where miniature shielding is desirable for each single device.

References

[1]   S. Liu *et al.*, "A Miniature Flexible Coil for High-SNR MRI of the Pituitary Gland," *IEEE Access*, vol. 10, pp. 12619–12628, 2022, doi: 10.1109/ACCESS.2022.3143544 (© 2022 IEEE).

[2]   P. C. Liang, Zhi-Pei; Lauterbur, *Principles of Magnetic Resonance Imaging: A Signal Processing Perspective*. New York: IEEE Press, 2000.

[3]   P. C. Lauterbur, "Image formation by induced local interactions: Examples employing nuclear magnetic resonance," *Nature*, 1973, doi: 10.1038/242190a0.

[4]   D. Zhang and Y. Rahmat-Samii, "Ultraflexible Electrotextile Magnetic Resonance Imaging (MRI) Radio-Frequency Coils," in *Antenna and Sensor Technologies in Modern Medical Applications*, Y. Rahmat-Samii and E. Topsakal, Eds. Wiley-IEEE Press, 2021.

[5]   J. T. Vaughan and J. R. Griffiths, "RF Coils for MRI," in *John Wiley & Sons*, 2012.

[6]   D. Nishimura G, *Principles of Magnetic Resonance Imaging*. Stanford University, 2010.

[7]   K. A. Asher, N. K. Bangerter, R. D. Watkins, and G. E. Gold, "Radiofrequency coils for musculoskeletal magnetic resonance imaging," *Top. Magn. Reson. Imaging*, vol. 21, no. 5, pp. 315–323, 2010, doi: 10.1097/RMR.0b013e31823cd184.

[8]   B. Gruber, M. Froeling, T. Leiner, and D. W. J. Klomp, "RF coils: A practical guide for nonphysicists," *Journal of Magnetic Resonance Imaging*. 2018, doi: 10.1002/jmri.26187.

[9]   O. Ocali and E. Atalar, "Ultimate intrinsic signal-to-noise ratio in MRI," *Magn. Reson. Med.*, vol. 39, no. 3, pp. 462–473, 1998, doi: 10.1002/mrm.1910390317.

[10]   J. P. Stockmann *et al.*, "A 32-channel combined RF and B0 shim array for 3T brain imaging," *Magn. Reson. Med.*, 2016, doi: 10.1002/mrm.25587.

[11]   G. C. Wiggins, C. Triantafyllou, A. Potthast, A. Reykowski, M. Nittka, and L. L. Wald, "32-Channel 3 tesla receive-only phased-array head coil with soccer-ball element geometry," *Magn. Reson. Med.*, 2006, doi: 10.1002/mrm.20925.

[12]   B. Keil *et al.*, "A 64-channel 3T array coil for accelerated brain MRI," *Magn. Reson. Med.*, 2013, doi: 10.1002/mrm.24427.

[13]   S. E. Moyher, D. B. Vigneron, and S. J. Nelson, "Surface coil MR imaging of the human brain with an analytic reception profile correction," *J. Magn. Reson. Imaging*, 1995, doi: 10.1002/jmri.1880050204.

[14]   T. W. Redpath, "Signal-to-noise ratio in MRI," *British Journal of Radiology*. 1998, doi: 10.1259/bjr.71.847.9771379.

[15]   A. Berger, "Magnetic resonance imaging," *BMJ*, vol. 324, p. 35, 2002.

[16] J. Kurhanewicz *et al.*, "Analysis of cancer metabolism by imaging hyperpolarized nuclei: Prospects for translation to clinical research," *Neoplasia*, 2011, doi: 10.1593/neo.101102.

[17] E. A. Tanifum, C. Patel, M. E. Liaw, R. G. Pautler, and A. V. Annapragada, "Hydrophilic fluorinated molecules for spectral 19F MRI," *Sci. Rep.*, 2018, doi: 10.1038/s41598-018-21178-3.

[18] M. W. Lagemaat *et al.*, "31P MR spectroscopic imaging of the human prostate at 7 T: T1 relaxation times, Nuclear Overhauser Effect, and spectral characterization," *Magn. Reson. Med.*, 2015, doi: 10.1002/mrm.25209.

[19] N. R. Bryan, *Introduction to the Science of Medical Imaging*. Cambridge University Press, 2010.

[20] K. Coyne, "MRI: A Guided Tour," 2020. https://nationalmaglab.org/education/magnet-academy/learn-the-basics/stories/mri-a-guided-tour (accessed Oct. 25, 2022).

[21] M. E. Ladd, P. Bachert, M. Meyerspeer, and et al, "Pros and cons of ultra-high-field MRI/MRS for human application," *Prog. Nucl. Magn. Reson. Spectrosc.*, vol. 109, pp. 1–50, 2018.

[22] S. A. Winkler *et al.*, "Gradient and shim technologies for ultra high field MRI," *Neuroimage*, 2018, doi: 10.1016/j.neuroimage.2016.11.033.

[23] M. Lustig and D. Donoho, "Compressed sensing MRI," *Signal Process. …*, 2008.

[24] R. KRIEGL, "A flexible coil array for high resolution magnetic resonance imaging at 7 Tesla," Université Paris Sud - Paris XI; Medizinische Universität Wien, 2014.

[25] A. Kumar, W. A. Edelstein, and P. A. Bottomley, "Noise figure limits for circular loop MR coils," *Magn. Reson. Med.*, 2009, doi: 10.1002/mrm.21948.

[26] J. R. Corea *et al.*, "Screen-printed flexible MRI receive coils," *Nat. Commun.*, 2016, doi: 10.1038/ncomms10839.

[27] M. R. Bendall, "Surface Coil Techniques for in Vivo NMR," *Bull. Magn. Reson.*, vol. 8, no. 1/2, pp. 17–42, 1986.

[28] F. H. Lin, Y. J. Chen, J. W. Belliveau, and L. L. Wald, "Removing signal intensity inhomogeneity from surface coil MRI using discrete wavelet transform and wavelet packet," in *Annual Reports of the Research Reactor Institute, Kyoto University*, 2001, doi: 10.1109/iembs.2001.1017365.

[29] A. Kumar and P. A. Bottomley, "Optimized quadrature surface coil designs," *Magn. Reson. Mater. Physics, Biol. Med.*, vol. 21, no. 1–2, pp. 41–52, Mar. 2008, doi: 10.1007/s10334-007-0090-2.

[30] B. M. Zlatkin, *MRI of the Shoulder*, Second. LWW, 2003.

[31] A. Murphy and F. Gaillard, "MRI sequences (overview)," in *Radiopaedia.org*, 2015.

[32] J. Ballinger, E. Hassanzadeh, A. Murphy, and E. Al., "MRI pulse sequences," *Reference article, Radiopaedia.org.*, 2013. https://radiopaedia.org/articles/21957 (accessed Nov. 15, 2022).

[33] J. Jones and J. Yeung, "Echo time," in *Radiopaedia.org*, 2011.

[34] J. Yeung, A. Murphy, D. Bell, and E. Al., "Repetition time," *Reference article, Radiopaedia.org*, 2011. https://radiopaedia.org/articles/14588 (accessed Nov. 15, 2022).

[35] J. Wang, W. Mao, M. Qiu, M. B. Smith, and R. T. Constable, "Factors influencing flip angle mapping in MRI: RF pulse shape, slice-select gradients, off-resonance excitation, and B0 inhomogeneities," *Magn. Reson. Med.*, vol. 56, no. 2, 2006, doi: 10.1002/mrm.20947.

[36] A. Murphy and J. Yeung, "Spatial resolution (MRI)," in *Radiopaedia.org*, 2011.

[37] J. Graessner, "Bandwidth in MRI?," *MAGNETOM Flash*, 2013. https://www.mriquestions.com/uploads/3/4/5/7/34572113/bandwidth_in_mri_siemens_.pdf (accessed Nov. 15, 2022).

[38] "10 Imaging Basics: Signal-to-Noise Ratio (SNR)," in *The Physics of Clinical MR Taught Through Images*, 2014.

[39] "13 Image Resolution: Pixel and Voxel Size," in *The Physics of Clinical MR Taught Through Images*, 2018.

[40] W. Zafar, "Resolution, SNR, Signal Averaging and Scan Time in MRI for Metastatic Lesion in Spine: A Case Report in a 74 Years Old Patient," *Clin. Radiol. Imaging J.*, vol. 3, no. 1, 2019, doi: 10.23880/crij-16000139.

[41] D. Weishaupt, V. D. Köchli, and B. Marincek, "Factors Affecting the Signal-to-Noise Ratio," in *How does MRI work?*, 2003.

[42] A. Murphy and J. Ballinger, "Acquisition time," in *Radiopaedia.org*, 2013.

[43] L. K. Nieman and I. Ilias, "Evaluation and treatment of Cushing's syndrome," *American Journal of Medicine*. 2005, doi: 10.1016/j.amjmed.2005.01.059.

[44] L. K. Nieman, "Cushing's syndrome: Update on signs, symptoms and biochemical screening," in *European Journal of Endocrinology*, 2015, doi: 10.1530/EJE-15-0464.

[45] J. Newell-Price, X. Bertagna, A. B. Grossman, and L. K. Nieman, "Cushing's syndrome," *Lancet*. 2006, doi: 10.1016/S0140-6736(06)68699-6.

[46] P. Chittiboina *et al.*, "Endosphenoidal coil for intraoperative magnetic resonance imaging of the pituitary gland during transsphenoidal surgery," *J. Neurosurg.*, 2016, doi:

10.3171/2015.11.JNS151465.

[47]   A. A. J. De Rotte *et al.*, "Feasibility of high-resolution pituitary MRI at 7.0 tesla," *Eur. Radiol.*, vol. 24, no. 8, pp. 2005–2011, May 2014, doi: 10.1007/s00330-014-3230-x.

[48]   M. C. Rossi Espagnet *et al.*, "High-resolution DCE-MRI of the pituitary gland using radial k-space acquisition with compressed sensing reconstruction," *Am. J. Neuroradiol.*, vol. 36, no. 8, pp. 1444–1449, Aug. 2015, doi: 10.3174/ajnr.A4324.

[49]   S. L. Tsai, E. Laffan, and S. Lawrence, "A retrospective review of pituitary MRI findings in children on growth hormone therapy," *Pediatric Radiology*, vol. 42, no. 7. Springer, pp. 799–804, Jul. 2012, doi: 10.1007/s00247-012-2349-7.

[50]   J. Cristante *et al.*, "Why We Should Still Treat by Neurosurgery Patients with Cushing Disease and a Normal or Inconclusive Pituitary MRI," *J. Clin. Endocrinol. Metab.*, vol. 104, no. 9, pp. 4101–4113, Sep. 2019, doi: 10.1210/jc.2019-00333.

[51]   Y. Grober, H. Grober, M. Wintermark, J. A. Jane, and E. H. Oldfield, "Comparison of MRI techniques for detecting microadenomas in Cushing's disease," *J. Neurosurg.*, 2018, doi: 10.3171/2017.3.JNS163122.

[52]   J. Jagannathan *et al.*, "Outcome of using the histological pseudocapsule as a surgical capsule in Cushing disease: Clinical article," *J. Neurosurg.*, vol. 111, no. 3, 2009, doi: 10.3171/2008.8.JNS08339.

[53]   O. Hamid, L. El Fiky, O. Hassan, A. Kotb, and S. El Fiky, "Anatomic Variations of the Sphenoid Sinus and Their Impact on Trans-sphenoid Pituitary Surgery," *Skull Base*, vol. 18, no. 1, p. 9, Jan. 2008, doi: 10.1055/S-2007-992764.

[54]   M. Varrassi *et al.*, "High-resolution magnetic resonance imaging at 3T of pituitary gland: Advantages and pitfalls," *Gland Surgery*, vol. 8. 2019, doi: 10.21037/gs.2019.06.08.

[55]   "Acromegaly," *2022 Mayo Foundation for Medical Education and Research (MFMER)*, 2021. https://middlesexhealth.org/learning-center/diseases-and-conditions/acromegaly (accessed Jul. 19, 2022).

[56]   T. H. Le, "High-field, high-performance magnetic resonance: Technical challenges and clinical applications," *Appl. Radiol.*, vol. 33, no. 1 SUPPL., 2004.

[57]   B. Usman and F. Michael, "Gadolinium contrast agents," *Reference article, Radiopaedia.org.*, 2012. https://doi.org/10.53347/rID-18340 (accessed Jul. 19, 2022).

[58]   M. Zaitsev, J. Maclaren, and M. Herbst, "Motion Artifacts in MRI: A Complex Problem With Many Partial Solutions," *J. Magn. Reson. Imaging*, vol. 42, no. 4, pp. 887–901, 2015, doi: 10.1002/jmri.24850.

[59]   C. M. Collins, "Fundamentals of Signal-to-Noise Ratio (SNR)," in *Electromagnetics in Magnetic Resonance Imaging Physical Principles, Related Applications, and Ongoing*

Developments, IOP Publishing, 2016.

[60]   C. M. Collins and M. B. Smith, "Signal-to-noise ratio and absorbed power as functions of main magnetic field strength, and definition of '90°' RF pulse for the head in the birdcage coil," *Magn. Reson. Med.*, vol. 45, no. 4, 2001, doi: 10.1002/mrm.1091.

[61]   A. Yao *et al.*, "Pituitary adenoma consistency: Direct correlation of ultrahigh field 7T MRI with histopathological analysis," *Eur. J. Radiol.*, vol. 126, p. 108931, May 2020, doi: 10.1016/J.EJRAD.2020.108931.

[62]   J. W. Rutland *et al.*, "Analysis of 7-tesla diffusion-weighted imaging in the prediction of pituitary macroadenoma consistency," *J. Neurosurg.*, vol. 134, no. 3, pp. 771–779, Feb. 2020, doi: 10.3171/2019.12.JNS192940.

[63]   C. Y. Wang *et al.*, "Idiopathic growth hormone deficiency in the morphologically normal pituitary gland is associated with perfusion delay," *Radiology*, vol. 258, 2011, doi: 10.1148/radiol.10100504.

[64]   H. Nakazawa *et al.*, "Efficacy of magnetic resonance imaging at 3 T compared with 1.5 T in small pituitary tumors for stereotactic radiosurgery planning," doi: 10.1007/s11604-013-0262-0.

[65]   W. A. Gibby, "MRI Hardware, Signal-to-Noise Ratio, and Safety," in *Neuroimaging*, New York, 2000.

[66]   Y. Mazaheri, H. A. Vargas, G. Nyman, A. Shukla-Dave, O. Akin, and H. Hricak, "Diffusion-weighted MRI of the prostate at 3.0 T: Comparison of endorectal coil (ERC) MRI and phased-array coil (PAC) MRI-THE impact of SNR on ADC measurement," *Eur. J. Radiol.*, vol. 82, no. 10, pp. e515–e520, 2013, doi: 10.1016/j.ejrad.2013.04.041.

[67]   B. Turkbey *et al.*, "Comparison of endorectal coil and nonendorectal coil T2W and diffusion-weighted MRI at 3 Tesla for localizing prostate cancer: Correlation with whole-mount histopathology," *J. Magn. Reson. Imaging*, vol. 39, no. 6, pp. 1443–1448, 2014, doi: 10.1002/jmri.24317.

[68]   A. W. Magill and R. Gruetter, "Nested Surface Coils for Multinucler NMR," in *RF Coils for MRI*, 1 st., J. T. Vaughan and J. R. Griffiths, Eds. Chichester, UK: John Wiley & Sons, 2012, pp. 39–50.

[69]   D. T. P. Nilsson, J. J. Mohr, and V. Zhurbenko, "Practical aspects of 13C surface receive coils with active decoupling and tuning circuit," in *European Microwave Week 2012: "Space for Microwaves", EuMW 2012, Conference Proceedings - 42nd European Microwave Conference, EuMC 2012*, 2012, doi: 10.23919/eumc.2012.6459403.

[70]   G. Giovannetti *et al.*, "Hyperpolarized 13C MRS surface coil: Design and signal-to-noise ratio estimation," *Med. Phys.*, 2010, doi: 10.1118/1.3491437.

[71]   A. O. Solis, S E;Wang, R; Tomasi, D; Rodriguez, "A multi-slot surface coil for MRI of

dual-rat imaging at 4 T," *Phys. Med. Biol.*, vol. 56, no. 12, 2011.

[72]   B. Zhang, D. K. Sodickson, and M. A. Cloos, "A high-impedance detector-array glove for magnetic resonance imaging of the hand," *Nat. Biomed. Eng.*, 2018, doi: 10.1038/s41551-018-0233-y.

[73]   J. R. Hadley, L. Slusser, P. R. Merrill, E. Minalga, and L. D. Parker, "Remote Tuning an Matching of a Non-Resonant Wire Loop," in *ISMRM*, 2018.

[74]   "No Title," *COMSOL Multiphysics® v. 5.2. www.comsol.com. COMSOLAB, Stockholm, Sweden.* .

[75]   "The Finite Element Method (FEM)," 2016. https://www.comsol.com/multiphysics/finite-element-method.

[76]   "RF Module User's Guide, version 5.4." COMSOL, Inc, [Online]. Available: www.comsol.com.

[77]   W. X. Er, W. J. Lim, Y. Dwihapsari, M. N. A. Awang, and A. N. Yusoff, "Signal-to-noise ratio uniformity and stability of agar gel phantom with iron (III) oxide as relaxation modifier," *Beni-Suef Univ. J. Basic Appl. Sci.*, vol. 10, no. 1, 2021, doi: 10.1186/s43088-021-00173-0.

[78]   N. S. M. Yusof, E. Supriyanto, and D. E. O. Dewi, "Investigation of electrochemical characterization of agarose gel for model of human head correlated to lightning currents," in *Proceedings of 2016 International Conference on Robotics, Automation and Sciences, ICORAS 2016*, 2017, doi: 10.1109/ICORAS.2016.7872622.

[79]   G. McIlvain, E. Ganji, C. Cooper, M. L. Killian, B. A. Ogunnaike, and C. L. Johnson, "Reliable preparation of agarose phantoms for use in quantitative magnetic resonance elastography," *J. Mech. Behav. Biomed. Mater.*, vol. 97, 2019, doi: 10.1016/j.jmbbm.2019.05.001.

[80]   L. A. Krause, "Dielectrically-accurate Tissue Simulating Materials for a Heterogeneous Breast MRI Phantom," Purdue University, 2018.

[81]   K. M. Gilbert, T. J. Scholl, and B. A. Chronik, "RF coil loading measurements between 1 and 50 MHz to guide field-cycled MRI system design," *Concepts Magn. Reson. Part B Magn. Reson. Eng.*, 2008, doi: 10.1002/cmr.b.20118.

[82]   S. E. Solis, G. Cuellar, R. L. Wang, D. Tomasi, and A. O. Rodriguez, "Transceiver 4-leg birdcage for high field MRI: Knee imaging," *Rev. Mex. Fis.*, 2008.

[83]   K. Thayalan, *The Physics of Radiology and Imaging*. JP Medical Ltd, 2014.

[84]   S. Solis-Najera, G. Cuellar, R. Wang, D. Tomasi, and A. Rodríguez, "Transceiver 4-leg birdcage for high field MRI: Knee imaging," *Rev. Mex. Física, ISSN 0035-001X, Vol. 54, Nº. 3, 2008, pags. 215-221*, vol. 54, 2009.

[85]   G. Giovannetti *et al.*, "Conductor geometry and capacitor quality for performance optimization of low-frequency birdcage coils," *Concepts Magn. Reson. Part B Magn. Reson. Eng.*, 2004, doi: 10.1002/cmr.b.20005.

[86]   D. Zhang and Y. Rahmat-Samii, "A novel flexible electrotextile 3T MRI RF coil array for carotid artery imaging: Design, characterization, and prototyping," *IEEE Trans. Antennas Propag.*, vol. 67, no. 8, 2019, doi: 10.1109/TAP.2019.2891700.

[87]   D. I. Hoult and R. E. Richards, "The signal-to-noise ratio of the nuclear magnetic resonance experiment," *J. Magn. Reson.*, 1976, doi: 10.1016/0022-2364(76)90233-X.

[88]   K. Ocegueda and A. O. Rodríguez, "A simple method to calculate the signal-to-noise ratio of a circular-shaped coil for MRI," *Concepts Magn. Reson. Part A Bridg. Educ. Res.*, 2006, doi: 10.1002/cmr.a.20066.

[89]   C. Stumpf, M. Malzacher, and L.-P. Schmidt, "Radio Frequency Modeling of Receive Coil Arrays for Magnetic Resonance Imaging," *J. Imaging*, vol. 4, no. 67, 2018.

[90]   M. V. Vaidya, C. M. Collins, D. K. Sodickson, R. Brown, G. C. Wiggins, and R. Lattanzi, "Dependence of B1- and B1+ field patterns of surface coils on the electrical properties of the sample and the MR operating frequency," *Concepts Magn. Reson. Part B Magn. Reson. Eng.*, 2016, doi: 10.1002/cmr.b.21319.

[91]   J. Yu, H. Agarwal, M. Stuber, and M. Schär, "Practical signal-to-noise ratio quantification for sensitivity encoding: Application to coronary MR angiography," *J. Magn. Reson. Imaging*, 2011, doi: 10.1002/jmri.22571.

[92]   D. I. Hoult and P. C. Lauterbur, "The sensitivity of the zeugmatographic experiment involving human samples," *J. Magn. Reson.*, vol. 34, no. 2, 1979, doi: 10.1016/0022-2364(79)90019-2.

[93]   M. D. Harpen, "Sample noise with circular surface coils," *Med. Phys.*, vol. 14, no. 4, 1987, doi: 10.1118/1.596027.

[94]   R. B. Buxton, *Introduction to functional magnetic resonance imaging: Principles and techniques*. 2009.

[95]   J. P. Marques, F. F. J. Simonis, and A. G. Webb, "Low-field MRI: An MR physics perspective," *Journal of Magnetic Resonance Imaging*. 2019, doi: 10.1002/jmri.26637.

[96]   G. Giovannetti *et al.*, "Simulation, design, and test of an elliptical surface coil for magnetic resonance imaging and spectroscopy," *Concepts Magn. Reson. Part B Magn. Reson. Eng.*, 2017, doi: 10.1002/cmr.b.21361.

[97]   P. Ibinaiye, S. Olarinoye-Akorede, O. Kajogbola, and A. Bakari, "Magnetic Resonance Imaging Determination of Normal Pituitary Gland Dimensions in Zaria, Northwest Nigerian Population," *J. Clin. Imaging Sci.*, vol. 5, no. 1, 2015, doi: 10.4103/2156-7514.157853.

[98] C. Keanninsiri, P. Cheiwvit, S. Tritrakarn, K. Thepamongkhol, and J. Santiprabhop, "Size and Shape of the Pituitary Gland with MR Imaging from Newborn to 30 Years: A Study at Siriraj Hospital," in *6th Annual Scientific Meeting, Phitsanulok, Thailand*, 2012.

[99] A. P. Amar and M. H. Weiss, "Pituitary anatomy and physiology," *Neurosurgery Clinics of North America*, vol. 14, no. 1. pp. 11–23, 2003, doi: 10.1016/S1042-3680(02)00017-7.

[100] K. Yoshimura *et al.*, "Development of a tissue-equivalent MRI phantom using carrageenan gel," *Magn. Reson. Med.*, vol. 50, no. 5, pp. 1011–1017, Nov. 2003, doi: 10.1002/mrm.10619.

[101] D. R. Messroghli, A. Radjenovic, S. Kozerke, D. M. Higgins, M. U. Sivananthan, and J. P. Ridgway, "Modified look-locker inversion recovery (MOLLI) for high-resolution T 1 mapping of the heart," *Magn. Reson. Med.*, vol. 52, no. 1, pp. 141–146, 2004, doi: 10.1002/mrm.20110.

[102] C. D. Constantinides, E. Atalar, and E. R. McVeigh, "Signal-to-noise measurements in magnitude images from NMR phased arrays," *Magn. Reson. Med.*, vol. 38, no. 5, pp. 852–857, 1997, doi: 10.1002/mrm.1910380524.

[103] P. Kellman and E. R. McVeigh, "Image reconstruction in SNR units: a general method for SNR measurement," *Magn. Reson. Med.*, vol. 54, no. 6, pp. 1439–1447, 2005, doi: 10.1002/mrm.20713.

[104] M. Alfonsetti *et al.*, "Versatile coil design and positioning of transverse-field RF surface coils for clinical 1.5-T MRI applications," *Magn. Reson. Mater. Physics, Biol. Med.*, 2005, doi: 10.1007/s10334-004-0090-4.

[105] K. Forbes, J. Karis, and W. L. White, "Imaging of the Pituitary Gland," *Barrow Neurological Institute*, 2002. https://www.barrowneuro.org/for-physicians-researchers/education/grand-rounds-publications-media/barrow-quarterly/volume-18-no-3-2002/imaging-pituitary-gland-2/#:~:text=The size of the pituitary,and more upwardly convex (Fig. (accessed Sep. 30, 2022).

[106] "IEC 60601-2-33 Edition 3 Amendment 2," *Particular Requirements for The Basic Safety and Essential Performance of Magnetic Resonance Equipment for Medical Diagnosis, Geneva, Switzerland*, 2015. https://webstore.iec.ch/publication/22705 (accessed Sep. 21, 2022).

[107] P. A. Bottomley, "Turning Up the Heat on MRI," *J. Am. Coll. Radiol.*, vol. 5, no. 7, 2008, doi: 10.1016/j.jacr.2008.04.003.

[108] J. S. van den Brink, "Thermal Effects Associated with RF Exposures in Diagnostic MRI: Overview of Existing and Emerging Concepts of Protection," *Concepts Magn. Reson. Part B*, vol. 2019, 2019, doi: 10.1155/2019/9618680.

[109] A. Macovski, "Noise in MRI," *Magn. Reson. Med.*, vol. 36, no. 3, pp. 494–497, Sep. 1996,

doi: 10.1002/mrm.1910360327.

[110] M. Law *et al.*, "Value of pituitary gland MRI at 7 T in Cushing's disease and relationship to inferior petrosal sinus sampling: Case report," *J. Neurosurg.*, vol. 130, no. 2, pp. 347–351, Feb. 2019, doi: 10.3171/2017.9.JNS171969.

[111] D. I. Hoult, C. -N Chen, and V. J. Sank, "Quadrature detection in the laboratory frame," *Magn. Reson. Med.*, vol. 1, no. 3, 1984, doi: 10.1002/mrm.1910010305.

[112] T. W. Redpath, "Quadrature rf coil pairs," *Magnetic Resonance in Medicine*, vol. 3, no. 1. 1986, doi: 10.1002/mrm.1910030115.

[113] M. S. Kim, "Investigation of factors affecting body temperature changes during routine clinical head magnetic resonance imaging," *Iran. J. Radiol.*, vol. 13, no. 4, 2016, doi: 10.5812/iranjradiol.34016.

[114] R. Deichmann, C. D. Good, O. Josephs, J. Ashburner, and R. Turner, "Optimization of 3-D MP-RAGE sequences for structural brain imaging," *Neuroimage*, vol. 12, no. 1, 2000, doi: 10.1006/nimg.2000.0601.

[115] G. Nair, M. Absinta, and D. S. Reich, "Optimized T1-MPRAGE sequence for better visualization of spinal cord multiple sclerosis lesions at 3T," *Am. J. Neuroradiol.*, vol. 34, no. 11, 2013, doi: 10.3174/ajnr.A3637.

[116] C. Y. Lin *et al.*, "Bio-compatibility and bio-insulation of implantable electrode prosthesis ameliorated by A-174 silane primed parylene-C deposited embedment," *Micromachines*, vol. 11, no. 12, 2020, doi: 10.3390/mi11121064.

[117] Y. H. Jung *et al.*, "A Compact Parylene-Coated WLAN Flexible Antenna for Implantable Electronics," *IEEE Antennas Wirel. Propag. Lett.*, vol. 15, pp. 1382–1385, 2016, doi: 10.1109/LAWP.2015.2510372.

[118] N. Beshchasna *et al.*, "Influence of artificial body fluids and medical sterilization procedures on chemical stability of parylene C," in *Proceedings - Electronic Components and Technology Conference*, 2010, doi: 10.1109/ECTC.2010.5490711.

[119] C. W. Scarantino, D. M. Ruslander, C. J. Rini, G. G. Mann, H. T. Nagle, and R. D. Black, "An implantable radiation dosimeter for use in external beam radiation therapy," *Med. Phys.*, vol. 31, no. 9, 2004, doi: 10.1118/1.1778809.

[120] D. C. Rodger *et al.*, "Flexible parylene-based multielectrode array technology for high-density neural stimulation and recording," *Sensors Actuators, B Chem.*, vol. 132, no. 2, 2008, doi: 10.1016/j.snb.2007.10.069.

[121] B. J. Kim *et al.*, "Parylene MEMS patency sensor for assessment of hydrocephalus shunt obstruction," *Biomed. Microdevices*, vol. 18, no. 5, p. 87, 2016, doi: 10.1007/s10544-016-0112-9.

[122] R. Zetik, J. Sachs, and R. Thoma, "UWB short-range radar sensing - The architecture of a baseband, pseudo-noise UWB radar sensor," *IEEE Instrum. Meas. Mag.*, vol. 10, no. 2, 2007, doi: 10.1109/mim.2007.364960.

[123] R. Chakraborty, N. Kumari, M. Mousam, and A. Mukherjee, "The Future of 5G and Millimeter Waves," in *Proceedings of the 2nd International Conference on Electronics, Communication and Aerospace Technology, ICECA 2018*, 2018, doi: 10.1109/ICECA.2018.8474584.

[124] L. M. Frazier, "Surveillance through walls and other opaque materials," *IEEE Aerosp. Electron. Syst. Mag.*, vol. 11, no. 10, 1996, doi: 10.1109/62.538794.

[125] P. Bandara and D. O. Carpenter, "Planetary electromagnetic pollution: it is time to assess its impact," *The Lancet Planetary Health*, vol. 2, no. 12. 2018, doi: 10.1016/S2542-5196(18)30221-3.

[126] K. B. Cheng, M. L. Lee, S. Ramakrishna, and T. H. Ueng, "Electromagnetic Shielding Effectiveness of Stainless Steel/Polyester Woven Fabrics," *Text. Res. J.*, vol. 71, no. 1, 2001, doi: 10.1177/004051750107100107.

[127] S. J. Genuis, "Fielding a current idea: exploring the public health impact of electromagnetic radiation," *Public Health*, vol. 122, no. 2, 2008, doi: 10.1016/j.puhe.2007.04.008.

[128] J. C. Wu, L. Li, J. C. Harrison, and R. N. Candler, "Micro-to millimeter scale magnetic shielding," in *TRANSDUCERS 2017 - 19th International Conference on Solid-State Sensors, Actuators and Microsystems*, 2017, doi: 10.1109/TRANSDUCERS.2017.7994179.

[129] S. Geetha, K. K. S. Kumar, C. R. K. Rao, M. Vijayan, and D. C. Trivedi, "EMI shielding: Methods and materials - A review," *J. Appl. Polym. Sci.*, vol. 112, no. 4, 2009, doi: 10.1002/app.29812.

[130] H. Wang, S. Li, M. Liu, J. Li, and X. Zhou, "Review on Shielding Mechanism and Structural Design of Electromagnetic Interference Shielding Composites," *Macromolecular Materials and Engineering*, vol. 306, no. 6. 2021, doi: 10.1002/mame.202100032.

[131] X. C. Tong, *Advanced Materials and Design for Electromagnetic Interference Shielding*. 2016.

[132] O. L. Krivanek *et al.*, "An electron microscope for the aberration-corrected era," *Ultramicroscopy*, vol. 108, no. 3, 2008, doi: 10.1016/j.ultramic.2007.07.010.

[133] X. T. Xu, Z. Y. Wang, R. H. Jiao, C. R. Yi, W. Sun, and S. Chen, "Ultra-low noise magnetic field for quantum gases," *Rev. Sci. Instrum.*, vol. 90, no. 5, 2019, doi: 10.1063/1.5087957.

[134] T. Van Zoest *et al.*, "Bose-einstein condensation in microgravity," *Science (80-.).*, vol. 328, no. 5985, 2010, doi: 10.1126/science.1189164.

[135] A. Farolfi, D. Trypogeorgos, G. Colzi, E. Fava, G. Lamporesi, and G. Ferrari, "Design and characterization of a compact magnetic shield for ultracold atomic gas experiments," *Rev. Sci. Instrum.*, vol. 90, no. 11, 2019, doi: 10.1063/1.5119915.

[136] J. Li *et al.*, "SERF Atomic Magnetometer-Recent Advances and Applications: A Review," *IEEE Sens. J.*, vol. 18, no. 20, 2018, doi: 10.1109/JSEN.2018.2863707.

[137] M. Nisenoff, "Progress bringing superconductor digital technology to the market place," *IEICE Trans. Electron.*, vol. E91-C, no. 3, 2008, doi: 10.1093/ietele/e91-c.3.252.

[138] O. A. Mukhanov, "Superconductive single-flux quantum technology," in *Digest of Technical Papers - IEEE International Solid-State Circuits Conference*, 1994, doi: 10.1109/isscc.1994.344703.

[139] K. K. Likharev, O. A. Mukhanov, and V. K. Semenov, "RESISTIVE SINGLE FLUX QUANTUM LOGIC FOR THE JOSEPHSON-JUNCTION DIGITAL TECHNOLOGY," in *SQUID '85 Superconducting Quantum Interference Devices and their Applications*, 2012.

[140] F. Furuta, K. Saitou, A. Yosiiida, and H. Suzuki, "Superconductor/semiconductor hybrid analog-to-digital converter," *IEICE Trans. Electron.*, vol. E91-C, no. 3, 2008, doi: 10.1093/ietele/e91-c.3.356.

[141] T. Ortlepp and F. H. Uhlmann, "Recent Progress in Superconductive Digital Electronics Part II - Japanese Contributions," *IEEE/CSC & ESAS EUROPEAN SUPERCONDUCTIVITY NEWS FORUM*, no. 5, 2008.

[142] Y. Kameda, Y. Hashimoto, and S. Yorozu, "Design and demonstration of a prototype system and 1O-Gbps 4 × 4 SFQ network switch bit-error-rate measurement," *IEICE Trans. Electron.*, vol. E91-C, no. 3, 2008, doi: 10.1093/ietele/e91-c.3.333.

[143] A. I. Braginski, "Superconductor Electronics: Status and Outlook," *J. Supercond. Nov. Magn.*, vol. 32, no. 1, 2019, doi: 10.1007/s10948-018-4884-4.

[144] S. A. Stuiber, "Creation of ultra-low remanent fields and homogeneous NMR fields for precision experiments," Techn. Univ. München, 2018.

[145] J. M. Kreikebaum, A. Dove, W. Livingston, E. Kim, and I. Siddiqi, "Optimization of infrared and magnetic shielding of superconducting TiN and Al coplanar microwave resonators," *Supercond. Sci. Technol.*, vol. 29, no. 10, 2016, doi: 10.1088/0953-2048/29/10/104002.

[146] Y. Yamanashi and N. Yoshikawa, "Design and evaluation of magnetic field tolerant single flux quantum circuits for superconductive sensing systems," *IEICE Trans. Electron.*, vol. E97-C, no. 3, 2014, doi: 10.1587/transele.E97.C.178.

[147] Y. Mizugaki *et al.*, "Magnetic isolation on a superconducting ground plane," *Japanese J. Appl. Physics, Part 1 Regul. Pap. Short Notes Rev. Pap.*, vol. 38, no. 10, 1999, doi: 10.1143/jjap.38.5869.

[148] R. Collot, P. Febvre, J. Kunert, H. G. Meyer, R. Stolz, and J. L. Issler, "Characterization of an On-Chip Magnetic Shielding Technique for Improving SFQ Circuit Performance," *IEEE Trans. Appl. Supercond.*, vol. 26, no. 3, 2016, doi: 10.1109/TASC.2016.2542117.

[149] Y. A. Polyakov, V. K. Semenov, and S. K. Tolpygo, "3D active demagnetization of cold magnetic shields," in *IEEE Transactions on Applied Superconductivity*, 2011, vol. 21, no. 3 PART 1, doi: 10.1109/TASC.2010.2091384.

[150] L. Wei, G. Wang, J. Li, S. Zhang, and G. Hong, "Multilayer magnetic shielding for testing a superconducting single-flux-quantum circuit chip in liquid helium dewar," *J. Instrum.*, vol. 16, no. 4, 2021, doi: 10.1088/1748-0221/16/04/P04007.

[151] S. Levy, "Electromagnetic Shielding Effect of an Infinite Plane Conducting Sheet Placed Between Circular Coaxial Coils," *Proc. Inst. Radio Eng.*, vol. 24, no. 6, 1936, doi: 10.1109/JRPROC.1936.228237.

[152] J. G. Negi, "RADIATION RESISTANCE OF A VERTICAL MAGNETIC DIPOLE OVER AN INHOMOGENEOUS EARTH," *GEOPHYSICS*, vol. 26, no. 5, 1961, doi: 10.1190/1.1438927.

[153] A. Touazi, I. Dergham, Y. Alayli, L. Chassagne, and J. Linares, "COMSOL simulation of an attenuated magnetic field through a metallic plate," in *Journal of Physics: Conference Series*, 2018, vol. 1141, no. 1, doi: 10.1088/1742-6596/1141/1/012156.

[154] J. R. MOSER, "Low-Frequency Shielding of a Circular Loop Electromagnetic Field Source," *IEEE Trans. Electromagn. Compat.*, vol. EMC-9, no. 1, 1967, doi: 10.1109/TEMC.1967.4307447.

[155] S. A. Schelkunoff, *Electromagnetic Waves*, 1st Ed. New York: D. Van Nostrand Company, Inc, 1943.

[156] W. Frei, "Computational Electromagnetics Modeling: Which Module to Use?," 2020. https://www.comsol.com/blogs/computational-electromagnetics-modeling-which-module-to-use/ (accessed Jul. 29, 2022).

[157] M. Glickman, T. Niblock, J. Harrison, I. B. Goldberg, P. Tseng, and J. W. Judy, "High permeability permalloy for MEMS," in *Technical Digest - Solid-State Sensors, Actuators, and Microsystems Workshop*, 2010, doi: 10.31438/trf.hh2010.88.

[158] D. A. Chavan and T. A. Jadhav, "Analysis of Laser Sintering Process in 3D Metal Printer," *Int. J. Sci. Adv. Res. Technol.*, vol. 4, no. 10, pp. 27–37, 2018.

[159] J. Hyun, "Design of a Pressure-fed Gas System Operating at Supercritical Temperatures and Pressures," Purdue University Graduate School, 2019.

[160] G. T. Furukawa, W. G. Saba, and M. L. Reilly, "Critical Analysis of the Heat-Capacity Data of the Literature and Evaluation of Thermodynamic Properties of Copper , Silver , and Gold from 0 to 300 K," *National Standard Reference Data Series- National Bureau of Standards 18*, vol. 18, no. April. 1968.

[161] O. R. Christianson *et al.*, "Design and Projected Performance of the Westinghouse μSMES Unit," 1996.

[162] J. C. Thompson and B. A. Younglove, "Thermal conductivity of silicon at low temperatures," *J. Phys. Chem. Solids*, vol. 20, no. 1–2, 1961, doi: 10.1016/0022-3697(61)90146-9.

[163] P. Flubacher, A. J. Leadbetter, and J. A. Morrison, "The heat capacity of pure silicon and germanium and properties of their vibrational frequency spectra," *Philos. Mag.*, vol. 4, no. 39, 1959, doi: 10.1080/14786435908233340.

[164] R. L. Powell and W. A. Blanpied, "NBS Circular 556," p. 31, 1954.

[165] G. K. White and S. B. Woods, "Electrical and thermal resistivity of the transition elements at low temperatures," *Philos. Trans. R. Soc. London. Ser. A, Math. Phys. Sci.*, vol. 251, no. 995, 1959, doi: 10.1098/rsta.1959.0004.

[166] R. H. Busey and W. F. Giauque, "The Heat Capacity of Nickel from 15 to 300°K. Entropy and Free Energy Functions," *J. Am. Chem. Soc.*, vol. 74, no. 12, 1952, doi: 10.1021/ja01132a058.

[167] M. I. Beyaz, M. McCarthy, and R. Ghodssi, "FABRICATION OF HIGH-ASPECT-RATIO METAL STRUCTURES WITH PLANAR SURFACES FOR POWER MEMS DEVICES," in *PowerMEMS*, 2009.

[168] G. Sun, J. I. Hur, X. Zhao, and C. J. Kim, "Fabrication of very-high-aspect-ratio micro metal posts and gratings by photoelectrochemical etching and electroplating," *J. Microelectromechanical Syst.*, vol. 20, no. 4, 2011, doi: 10.1109/JMEMS.2011.2148163.

[169] J. Bergström, "Experimental Characterization Techniques," in *Mechanics of Solid Polymers*, 2015.

[170] C. R. Yang, P. Y. Chen, Y. C. Chiou, and R. T. Lee, "Effects of mechanical agitation and surfactant additive on silicon anisotropic etching in alkaline KOH solution," *Sensors Actuators, A Phys.*, vol. 119, no. 1, 2005, doi: 10.1016/j.sna.2004.07.015.

[171] R. Rhee, K. Moon, and B. Yoo, "Synthesis of Permalloy (Ni-Fe) Nanosheets through Sonoelectrochemical Methods and its Magnetic Properties," *J. Korean Inst. Surf. Eng.*, vol. 51, no. 4, pp. 202–206, 2018, doi: https://doi.org/10.5695/JKISE.2018.51.4.202.

[172] P. Dixit and J. Miao, "Aspect-Ratio-Dependent Copper Electrodeposition Technique for Very High Aspect-Ratio Through-Hole Plating," *J. Electrochem. Soc.*, vol. 153, no. 6, 2006, doi: 10.1149/1.2189238.

[173] M. S. Chandrasekar and M. Pushpavanam, "Pulse and pulse reverse plating-Conceptual, advantages and applications," *Electrochimica Acta*, vol. 53, no. 8. 2008, doi: 10.1016/j.electacta.2007.11.054.

[174] "DC vs. Pulse Plating for Beginners," 2019. https://www.royalcircuits.com/2019/01/15/dc-vs-pulse-plating-for-beginners/ (accessed Sep. 06, 2022).